Soviet Physics

CRYSTALLOGRAPHY

Vol. 1, No. 5, pp. 389-484

September-October, 1956

SOVIET PHYSICS – CRYSTALLOGRAPHY VOL. 1, NO. 5 SEPT.-OCT., 1956

A RATIONAL METHOD OF DERIVING THE VARIOUS CLOSE-PACKED ARRAYS OF SPHERES

V. V. Bakakin and N. V. Belov

M. V. Lomonosov State University, Moscow

Translated from Kristallografiya, Vol. 1, No. 5,
pp. 491-494, September-October, 1956
Original article submitted July 13, 1956

Simplified methods are presented for calculating the number of arrays of close-packed spheres having a repeat distance of n layers; the distributions over the 8 symmetry groups are also given. Detailed calculations are presented for n = 13 and 14.

Belov [1] has given a complete list of close packings with repeat over n layers for values of n up to n = 12; there are 43 such packings for n = 12; for 13 layers and above, the problem appeared too difficult and consideration of it was deferred. The methods previously used have now been simplified somewhat and made more systematic; the solutions for n = 13 and 14 are obtained almost mechanically.

The essential minimum symmetry of any close-packed array is C_{3v}^1 = P3m (I); the packings for this purpose may be denoted by *h* and *c*, of which *h* divides the formula of *h* and *c* into two symmetrical halves and denotes the passage of a symmetry plane through the corresponding layer of spheres perpendicular to the packing axis. The centers of symmetry lie either in the *c* layers, in which case the formula is divided into two symmetrical halves, or between two *cc* or *hh* layers, if the corresponding pair divides the packing formula into two symmetrical halves.

The minimum repeat distance in a packing formula consisting of *h* and *c* corresponds either to a complete repeat distance in the array of spheres or to a half or third of the latter. That minimum repeat may contain an odd number of *h*, in which case it is always half the full repeat distance, and the array is characterized by a 6_3 axis (not a triad one), and so belongs to group C_{6v}^4 = $P6_3mc$ (II) if there are no additional symmetry elements. Alternatively, it may contain an even number of *h*, in which case the full repeat is determined by the number of *c* in the minimum repeat, which is found as follows: we count the *c* between each pair of *h*, the corresponding numbers being formed into a sum with alternating plus and minus signs (not excluding zeros, which correspond to runs of *h*). The algebraic sum may be a multiple of 3, in which case the repeat distance of the packing coincides with the minimum repeat distance of the formula, the space group being C_{3v}^1 = P3m in the absence of additional symmetry elements. Alternatively, the sum may not be a multiple of 3, in which case the full repeat is three times the minimum, and the space group is C_{3v}^1 = R3m (III) in the absence of additional symmetry elements.

Additional centers of symmetry are possible in all three cases: C_{3v}^1 = P3m becomes D_{3v}^3 = $P\bar{6}m$ = $P\bar{3}m$ (IV), and C_{3v}^1 = R3m becomes D_{3d}^5 = $R\bar{6}m$ = $R\bar{3}m$ (V), but those in group C_{6v}^4 = $P6_3mc$ also generate horizontal symmetry planes, so the space group becomes D_{6h}^4 = $P6_3/mmc$ (VI).

Horizontal symmetry planes may be added independently only to C_{3v}^1 = P3m, which gives D_{3h}^1 = P3/mm2 = P6m2 (VII).

The packing formula may not contain *h* at all, in which case we get cubic close packing ... *ccc* ... with symmetry $O_h^5 = Fm3m$ (VIII).

These features give us the following systematic way of deducing all packings of repeat distance n. We seek all groups with an even number p of *h* and with sums of the *c* that are multiples of 3. We first draw up all combinations of even numbers of *h* possible for the given n. For instance, for n = 13:

2, 11,
4, 31, 22, 211, 1111,
6, 51, 42, 411, 33, 321, 3111, 222,
2211, 2121, 21111, 111111,

8, 71, 62, 611, 53, 521, 5111, 44,
431, 422, 4211, 4121, 41111, 332,
3311, 3131, 3221, 3212, 32111,
31211, 2222, 22211, 21212,
10, 91; 82, 811, 73, 721, 64, 631,
622, 55, 541, 532, 442

Some c must come between the h, and here there cannot be less than 3, so $p = 10$ is the limit.

For each combination of the h we list the different numbers of c, and check that the algebraic sum is divisible by 3. For instance, for $n = 13$, we have for the 321 combination that

$+1+1-5=-3$ $+2+1-4=-1$ $+3+1-3=+1$
$+1+2-4=-1$ $+2+2-3=+1$ $+3-2+2=+3$
$+1+3-3=+1$ $+2+3-2=+3$ $+3+3-1=+5$
$+1+4-2=+3$ $+2+4-1=+5$ $+4+1-2=+3$
$+1+5-1=+5$ $+3+1-1=+5$ $+4+2-1=+5$

Five formulas for the 321 combination have multiples of 3, which in letter form are

1) . . . | hhhchhhcccccc | . . ., 2) . . . | hhhchhccccchcc | . . .,
3) . . . | hhhcchhcccchcc | . . ., 4) . . . | hhhccchhcchcc | . . .,
5) . . . | hhhcccchhchcc | . . .

The combinations of the h written as numbers may have symmetry planes, in which case insertion of the c gives us two formulas that are, respectively, mirror images, and such arrays are to be taken as identical. For instance, this occurs for the following in combination 141:

. . . | hchhhhccccchcc | . . . and . . . | cchcccchhhhch | . . .

All the combinations of the h are examined in this way to give us the total number of n-layer arrays, but some of these are only multiples of arrays of shorter repeat distance. These are struck out by specifying the minimum repeat distances, which may [1] only be $n/2$ or $n/3$, subject to certain conditions. Of course, no minimal periods are possible at all for $n = 13$, while for $n = 14$ they each have 7 members and correspond to independent 7-layer arrays provided that the number of h is even in each half. Finally, the arrays are assigned to their space groups by identification of centers of symmetry and mirror planes, in accordance with the above rules.

This gives the number of 13-layer arrays as 63, of which 21 have symmetry $D^3_{3d} = P\bar{6}m = P\bar{3}m$:[1]

1) | ccccchchcccc |, 2) | cchccccccchcc |, 3) | hhccccccccchh |,
4) | ccccchhchcccc |, 5) | chhccccccchhc |, 6) | ccchhccchhccc |,
7) | cchhccccchhcc |, 8) | hccchccchccch |, 9) | chccchchccchc |,
10) | hhchccccchchh |, 11) | chhhccccchhhc |, 12) | hchchccchchch |,
13) | hcchchchchcch |, 14) | chcchhchhcchc |, 15) | chchhccchhchc |,
16) | hhhcchchcchhh |, 17) | hcchhhchhhcch |, 18) | hchhhchchchhch |,
19) | hhhhhccchhhhh |, 20) | hhhchhchchhh |, 21) | hchhhhchhhhch |,

and 42 have symmetry $C^1_{3v} = P3m$:

22) | hhhccchcccccc |, 23) | hhchccchccccc |, 24) | hhchccccchcc |,
25) | hhcchccccchcc |, 26) | hchchchcccccc |, 27) | hchchchcccc |,
28) | hhhhhchcccccc |, 29) | hhhhchchcccc |, 30) | hhhhchchhccc |,
31) | hhhchhhcccccc |, 32) | hhhchhcccchcc |, 33) | hhhccchhchcc |,
34) | hhhcchhcchcc |, 35) | hhhccchhcchcc |, 36) | hhhchchchccc |,
37) | hhhchhcccchc |, 38) | hhhchchchcccc |, 39) | hhhchcccchcc |,
40) | hhchchchchcc |, 41) | hhchchcchchcc |, 42) | hhchchhchcccc |,
43) | hhchccchhcchc |, 44) | hhchhchcchcc |, 45) | hhcchhchcchcc |,
46) | hhhhhhhchcccc |, 47) | hhhhhhchchcc |, 48) | hhhhhchhhcccc |,
49) | hhhhhchhcccchc |, 50) | hhhhhcchhchc |, 51) | hhhhchhhchcchc |,
52) | hhhhchhhchccc |, 53) | hhhhccchhhchc |, 54) | hhhhcchhhchcc |,
55) | hhhhchhchchcc |, 56) | hhhhchhcchchc |, 57) | hhhhcchhchchc |,
58) | hhhchhhhchhccc |, 59) | hhhchhhchhcchc |, 60) | hhhchhcchhchc |,
61) | hhhcchhchhchc |, 62) | hhhhhhhhchhcc |, 63) | hhhhhhchhhhcc |.

The 14-layer arrays number 126, of which 7 have symmetry $D^4_{6h} = P6_3/mmc$:[2]

1) | cchcccccchccc |, 2) | cchhhcccchhhcc |,
3) | chhhhhccchhhhhc |, 4) | chchchcchchchc |, 5) | hcchcchhccchcch |,
6) | hhchchhhhchchh |, 7) | hchhhchchhhhch |.

One has symmetry $C^4_{6v} = P6_3/mc$:

8) | hchhcccchhccc |.

Twenty-four have symmetry $D^4_{3h} = P\bar{6}m2$:[3]

9) hhcccccchcccchh, 10) hchcccchcccchch, 11) hcchcccchccchcch,
12) hhhcccchcccchhh, 13) hhchcccchccchhh, 14) hhcchcchcchcchh,
15) hhcccchhchcccchh, 16) hchhcccchcccchch, 17) hchhcchcchcchch,
18) hhhhcccchcchhhh, 19) hhhcchhhcchhhh, 20) hhhcchchcchchh,
21) hchhhchcchhhch, 22) hhcchhchchhcch, 23) hhchchchchchch,
24) hchhchchchchch, 25) hhhhhcchcchhhh, 26) hhhhcchhhcchhh,
27) hchchhhhhhhchh, 28) hhhchchhhchhh, 29) hhchhhchchhchh,
30) hhhhhhchchhhhh, 31) hhhhhchhhchhhh, 32) hhhhchhhhhchhh.

Twenty-four have symmetry $D^3_{3d} = P\bar{3}m$:[4]

33) | ccccchhccccc |, 34) chcccccccccchc, 35) | cccchhchcccc |,
36) | chccchhccchc |, 37) chchcccccchch, 38) | chchcccchchc |,
39) chchcccccchchc, 40) | hhcchcccchchh |, 41) ccchhhhhhcccc,
42) hhhcchchcchhc, 43) | chhchcccchchc |, 44) chhcchchchchc,
45) cchhhchchhccc, 46) | hchchchchchch |, 47) | hhhhcccccchhh |,
48) | hhhcchhcchhh |, 49) cchhhhhchhhcc, 50) | cchhhhchhhcc |,
51) | cchhchhhhchcc |, 52) | chhchhhhchc |, 53) chhchhccchhchc,
54) | hchhcchhcchch |, 55) | hhhchchhchhh |, 56) | chhchhhhchhc |;

[1] The dots before and after the formulas are omitted. The centers of symmetry are found each time from the middle letter and the end strokes [1].

[2] The rules show that group D^4_{6h} has a center of symmetry at each end stroke and between the two central letters, while symmetry planes pass through letters 4 and 11 (see [1]).

[3] The first letter (accented) and the translationally identical 15th, and also the 8th, have symmetry planes [1].

[4] A center of symmetry lies at the start (and end) of the period, and another in the middle.

and 70 have symmetry C_{3v}^1 = P3m:[5]

57) | hhhsshsssssss |, 58) | hhchechecccccc |, 59) | hhchcccechcccc |
60) | hhechechcccccc |, 61) | hhechecccchccc |, 62) | hhcccchchcccc |
63) | hchechcccchccc |, 64) | hhhhhchcccccc |, 65) | hhhhchchcccccc |
66) | hhhhchcccchccc |, 67) | hhhhchchcccccc |, 68) | hhhhcchchcccc |
69) | hhhcchchcchccc |, 70) | hhhchhccchcccc |, 71) | hhhchhcccccchc |
72) | hhhchhchcchccc |, 73) | hhhchhcccchhc |, 74) | hhhcchhchcccc |
75) | hhhcchhcccchc |, 76) | hhhcccchhcchc |, 77) | hhhchchcchchcc |
78) | hhhcccchhchhc |, 79) | hhhchchcchchc |, 80) | hhhcccchhchc |
81) | hhchhchchcccc |, 82) | hhchhchcchcc |, 83) | hhchhchchcccc |
84) | hhcchhchchcccc |, 85) | hhcchhchchcc |, 86) | hhccchhchchcc |
87) | hhccchhchchc |, 88) | hhchchhchchcc |, 89) | hhchchchchcchcc |
90) | hhchchchcchc |, 91) | hhchchchchcc |, 92) | hhchcchchchcc |
93) | hhhhhhchhcccc |, 94) | hhhhhhchhccc |, 95) | hhhhhhchcchcc |
96) | hhhhhchhcchcc |, 97) | hhhhhcchhchcc |, 98) | hhhhhchchcchcc |
99) | hhhhhchcchchc |, 100) | hhhhchhchhccc |, 101) | hhhhchchchhcc |
102) | hhhhchhcchhc |, 103) | hhhhchhhcchcc |, 104) | hhhhchchhcchc |
105) | hhhhchhchcchc |, 106) | hhhhchchhcchcc |, 107) | hhhhchchhchcc |
108) | hhhhchchchchc |, 109) | hhhcchhhchhcc |, 110) | hhhchhhchcchcc |
111) | hhhcchhhchchc |, 112) | hhhchcchhhcchc |, 113) | hhhchhchhchcc |
114) | hhhchhchchhcc |, 115) | hhhchhchchchc |, 116) | hhhchhchcchchc |
117) | hhhchchhchcchc |, 118) | hhhcchchhchchc |, 119) | hhchchhcchchhc |
120) | hhhhhhhhchchc |, 121) | hhhhhhhchchcc |, 122) | hhhhhchhhchchc |
123) | hhhhhchhhhchcc |, 124) | hhhhhcchhhchhc |, 125) | hhhhhchhhhchchc |
126) | hhhhchhhchchc |.

LITERATURE CITED

1. N. V. Belov, Structures of Ionic Crystals and Metallic Phases [in Russian] (1947).

[5] There are no additional symmetry elements; in each group $\Sigma \equiv 0 \pmod 3$.

ACCURACY OF FOURIER SERIES FOR THE POTENTIAL IN ELECTRON DIFFRACTION

B. K. Vainshtein

Institute of Crystallography, Academy of Sciences of the USSR
Translated from Kristallografiya, Vol. 1, No. 5,
pp. 495-501, September-October, 1956
Original article submitted May 19, 1956

A method previously described is applied to give working formulas for the variance in the potential as deduced via Fourier series from electron-diffraction data, together with the errors in the peak heights arising from termination and the variances of the atomic coordinates.

Fourier series derived from experimental amplitudes do not give the true distribution of the lattice potential on account of experimental error, and also of series cutoff. The accuracy of the potential and of the atomic coordinates may be deduced by a method similar to that given previously for the electron density [1], which is as follows. The atomic f_e curves [2] are used to compute the integral characteristics G of the potential φ within the atoms for several B (thermal-vibration parameter): the mean-square potential, the potential at the center of the atom, and the mean square of the first derivative of the potential. These can be represented via a universal relation to the atomic number:

$$G = kZ^{\alpha} \cdot q, \tag{1}$$

in which k and α are governed by the Debye factor B characteristic of the crystal, q being determined by the cutoff; q = 1 when there is no cutoff, decreasing as the cutoff increases. The factor q reflects the loss of Fourier terms by cutoff. Sometimes it is necessary to take account of the contribution to a characteristic from terms in the cutoff region, in which case the q of (1) is replaced by (1 - q).

The accuracy of a Fourier series for the potential may readily be evaluated via the characteristics of the atoms in the unit cell, which are easily found from (1); here we need to know the extent of the experimental error, for which purpose we may use the factor

$$b = \frac{\Sigma |\Phi_0| - |\Phi_t|}{\Sigma |\Phi_0|}. \tag{2}$$

Only an approximate value for B is needed in order to evaluate the accuracy of the series; B ≈ 1 for most silicates and other materials with strong bonds and high melting points, ≈1-2 for ionic crystals and metals, and around 4 for organic crystals. Heavy atoms may reduce B to 0.5-1.

Error in the Potential

The Fourier series here is constructed from $\Phi_{hkl} + \Delta\Phi_{hkl}$, with $\Delta\Phi_{hkl} = b\Phi_{hkl}$ as the errors in deducing the amplitudes and b the mean relative error given by (2). The standard deviation in the potential is [1] dependent on b and is given by

$$\sqrt{\overline{\Delta\varphi_e^2}} = b\sqrt{\Sigma_i G_{i_i}/\Omega}, \tag{3}$$

in which G_i is the appropriate characteristic for the atom in question, the sum being taken over all the atoms in the cell, whose volume is Ω. The cutoff error is

$$\sqrt{\overline{\Delta\varphi_c^2}} = \sqrt{(1-q)\Sigma_i G_{i_i}/\Omega}. \tag{4}$$

The over-all standard deviation for a three-dimensional series on the basis of the G_i of (1) is then

$$\sqrt{\overline{\Delta\varphi^2}} = \sqrt{\overline{\Delta\varphi_e^2} + \overline{\Delta\varphi_c^2}} = \sqrt{(b^2q + 1 - q)k\Sigma Z_i^{\alpha}/\Omega}. \tag{5}$$

The Ω of (5) is replaced by S (cell area) for the two-dimensional series used in projections. Table 1 gives k, α, and q as functions of B for the two cases.

TABLE 1. Values of k, α, and q for (5)

Series dimensions	n	k	α	q for $(\sin\theta/\lambda)_c \cdot 10^{-8}$ = 0.5	0.6	0.7	0.8
Three	1	0.0557	1.39	0.780	0.861	0.913	0.948
	2	0.0490	1.35	0.920	0.960	0.982	0.995
	3	0.0443	1.32	0.950	0.980	0.995	1
	4	0.0399	1.30	0.965	0.987	0.997	1
Two	1	0.0800	1.27	0.917	0.951	0.978	0.989
	2	0.0840	1.24	0.960	0.983	0.994	1
	3	0.0815	1.22	0.980	0.993	0.998	1
	4	0.0790	1.20	0.987	0.997	1	1

TABLE 2. Values of k, α, and q for Use in (1) for $\varphi(0)$ and $\varphi'(0)$

	n	k	α	q for $(\sin\theta/\lambda)_c \cdot 10^{-8}$ = 0.5	0.6	0.7	0.8
$\varphi(0)$	1	0.753	0.81	0.33	0.45	0.55	0.64
	2	0.495	0.79	0.50	0.63	0.74	0.81
	3	0.376	0.77	0.60	0.73	0.83	0.89
	4	0.317	0.75	0.69	0.81	0.90	0.94
$\varphi'(0)$	1	0.480	0.75	0.59	0.69	0.77	0.83
	2	0.405	0.72	0.72	0.81	0.88	0.92
	3	0.362	0.70	0.80	0.88	0.93	0.96
	4	0.335	0.68	0.86	0.92	0.96	0.98

The G are calculated from the f_e given in [2], expressed in p-units,[1] so the error given by (5) will be in p/Å^3 (three dimensions) or p/Å^2 (two); conversion to volts (or volt-Å for projections) simply involves multiplication by 114.5 [3]. The peak heights are of the order of a few hundred volts, while $\sqrt{\overline{\Delta\varphi^2}}$ is around ten volts or so in ordinary structural studies, with b ≈ 0.2–0.3 and $(\sin\theta/\lambda)_c \approx 0.7$. The G given by (1) and Table 1 may be used to normalize Fourier series for the potential, i.e., to reduce them to the absolute scale [1,4,5].

The $\sqrt{\overline{\Delta\varphi^2}}$ of (5) gives an estimate of the error in φ as an average over the whole volume (or area) of the cell; but sometimes we need to know how the cutoff affects the peak heights $\varphi(0)$, as its effect is greatest for these. This $\varphi(0) = G_2$ is the second integral characteristic that can be put in the form of (1), as can the analogous quantity $\varphi'(0)$ for projections. The q in (1) indicates the loss in peak height; Table 2 gives the parameters of 1 for the cases of $\varphi(0)$ and $\varphi'(0)$.

This and (1) together enable us to find the expectation value for the potential at the center for any B. The peak heights in electron diffraction are proportional to Z^α, with $\alpha < 1$, which explains why light atoms are more readily detected in the presence of heavy ones ($\alpha > 1$ for x rays).

The peaks for the light atoms are readily seen, together with those from the heavy atoms, via Fourier series for the potential, on account of the weak dependence on atomic number [6]. The q of Table 2 show that cutoff reduces the heights substantially; as for the $\sqrt{\overline{\Delta\varphi^2}}$ of (5), the k of Table 2 calculated from (1) give the $\varphi(0)$ in p/Å^3, and the $\varphi'(0)$ in p/Å^2, while multiplication by 114.5 converts these respectively to volts and volt-Å.

Error in the Atomic Coordinates

The general formula for the error Δx_j in a coordinate of atom j is

$$\Delta x_j = \frac{\partial\Delta\varphi}{\partial x} \Big/ \left(\frac{\partial^2\varphi}{\partial x^2}\right)_j. \qquad (6)$$

Δx_j is directly proportional to the perturbation produced by the error and cutoff waves (i.e., to the first derivative of these) and is inversely proportional to the curvature of the peak for atom j (second derivative at the peak). The $\Delta\varphi$ have a random distribution, so the $\partial\Delta\varphi/\partial x$ do also; the numerator is therefore to be evaluated as its mean square, as in

[1] A p-unit is the electron scattering for a proton for $(\sin\theta/\lambda) = 0.1 \cdot 10^8$ cm^{-1} [2, 3].

the evaluation of $\Delta\varphi$ from (3)-(5). As in (3), the error introduced via $\partial\Delta\varphi/\partial x$ from errors in the amplitudes may [1] be found from

$$\overline{\left(\frac{\partial\Delta\varphi_e}{\partial x}\right)^2} = b^2 \sum_i G_{3i}/\Omega . \qquad (7)$$

while that introduced via the cutoff wave is, by analogy with (4), given by

$$\overline{\left(\frac{\partial\Delta\varphi_c}{\partial x}\right)^2} = (1-q) \sum_i G_{3i}/\Omega. \qquad (8)$$

The over-all standard deviation $\sqrt{\overline{(\partial\Delta\varphi/\partial x)^2}}$ may be calculated from the sums of (7) and (8) by analogy with (5); but here we need a certain refinement, because the cutoff wave has a regular structure, not a random one. The atom in question must lie outside spheres of radius about 2 Å drawn around all the other atoms; but the cutoff wave and the first derivative of this are maximal within such spheres, so the quantity we need to find, Δx_j, is only a fraction of that given by (8). It is found that the significant part of the mean square of the first derivative outside the sphere (as regards Δx_j) may be found by multiplying the result from (8) by $1/8$, so it accounts for $\sqrt{1/8} \approx 1/3$ of the total. Then,

$$\sqrt{\overline{\left(\frac{\partial\Delta\varphi}{\partial x}\right)^2}} = \sqrt{\left(b^2 q + \frac{1-q}{8}\right) k \Sigma Z_i^2/\Omega}. \qquad (9)$$

The second derivative may also be put as in (1):

$$\frac{\partial^2\varphi}{\partial x^2} = k' Z^{\alpha'} q' \qquad (10)$$

By substituting (9) and (10) into (6), we find, when B = 1-4, Eqs. (11a)-(11d) for particular values of the parameters $\sqrt{k}/k'$, α and α' with the introduction of an effective error b_{eff} given by Eq. (12); because of cutoff, the magnitude of this error is always larger than the error b given by Eq. (2).

For three-dimensional series

for $B = 1$ $\quad \Delta x_j = 0.025\,(b_{eff}/\sqrt{\Omega}) \sqrt{\Sigma Z_i^{1.62}}/Z_j^{0.88}$, (11a)

for $B = 2$ $\quad \Delta x_j = 0.045\,(b_{eff}/\sqrt{\Omega}) \sqrt{\Sigma Z_i^{1.56}}/Z_j^{0.85}$, (11b)

for $B = 3$ $\quad \Delta x_j = 0.065\,(b_{eff}/\sqrt{\Omega}) \sqrt{\Sigma Z_i^{1.52}}/Z_j^{0.82}$, (11c)

for $B = 4$ $\quad \Delta x_j = 0.093\,(b_{eff}/\sqrt{\Omega}) \sqrt{\Sigma Z_i^{1.48}}/Z_j^{0.80}$, (11d)

where $$b_{eff} = \frac{\sqrt{b^2 q + (1-q)/8}}{q'} . \qquad (12)$$

The q and q' are given by Table 3 and Fig. 1. The sum under the root in (11a)-(11d) is taken over all atoms in the unit cell; the atomic numbers Z_i^α in the denominator being for the atom appropriate to Δx_j; Ω is the cell volume.

The low q' show that cutoff markedly reduces the second derivative, especially for small B, which increases Δx_j.

The analogous formulas for two-dimensional series are

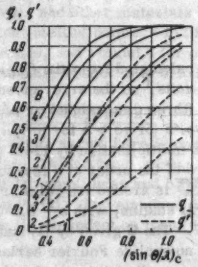

Fig. 1. Relation of q (solid lines) and q' (broken lines) to $(\sin\theta/\lambda)_c$ and to B for three-dimensional series.

TABLE 3. Values of q and q' for (12) for Three-Dimensional Series

	B	$\sin\theta/\lambda_c \cdot 10^{-8}$						
		0.4	0.5	0.6	0.7	0.8	0.9	1.0
q, %	1	22	36	49	62	72	80	87
	2	39	57	72	84	91	95	98
	3	52	72	85	93	97	99	100
	4	62	81	92	97	99	100	100
q', %	1	3	6	10	16	24	33	42
	2	6	13	24	35	47	57	67
	3	13	24	37	52	66	77	86
	4	19	35	51	66	79	89	94

TABLE 4. Values of q and q' for (12) for Two-Dimensional Series

	B	$\sin\theta/\lambda_c \cdot 10^{-8}$						
		0.4	0.5	0.6	0.7	0.8	0.9	1.0
q, %	1	42	57	69	78	86	92	96
	2	59	75	86	93	97	99	100
	3	68	84	93	97	99	100	100
	4	77	90	96	99	100	100	100
q', %	1	8	14	22	30	39	48	57
	2	17	28	41	54	65	76	83
	3	25	40	55	68	79	86	92
	4	33	51	67	79	88	94	97

for $B = 1$ $\Delta x_j = 0.057\,(b_{\text{eff}}/\sqrt{S})\,\sqrt{\sum_i Z_j^{1.55}/Z_i^{0.87}}$, (13a)

for $B = 2$ $\Delta x_j = 0.095\,(b_{\text{eff}}/\sqrt{S})\,\sqrt{\sum_i Z_j^{1.46}/Z_i^{0.83}}$, (13b)

for $B = 3$ $\Delta x_j = 0.130\,(b_{\text{eff}}/\sqrt{S})\,\sqrt{\sum_i Z_j^{1.42}/Z_i^{0.81}}$, (13c)

for $B = 4$ $\Delta x_j = 0.165\,(b_{\text{eff}}/\sqrt{S})\,\sqrt{\sum_i Z_j^{1.39}/Z_i^{0.79}}$ (13d)

Here, b_{eff} is still given by (12), but q and q' are different (Table 4 and Fig. 2); S is the cell area. It is to be appreciated that (13a)-(13d) are not applicable unless atom j is represented by a separate peak.

Equations (11) and (13) apply to Δx, Δy, and Δz; $\Delta x = \Delta y = \Delta z$ if the cutoff is the same in all directions, but q and q' will vary with direction if it is not, as will the b_{eff} of (12), so the errors will be different (largest in the direction of greatest cutoff).

Equations (11) and (13) give the inherent errors of the series for the potential. The errors in the atomic coordinates in addition include contributions from errors in the cell constants and in the interpolations involved in locating the maxima. These additional sources of error are usually relatively trivial and increase the Δx_j of (11) and (13) only slightly; reasonable intensity estimates ($b \approx 0.2$) and optimal cutoff at $(\sin\theta/\lambda) \cdot 10^{-8} = 0.6$-$0.7$ have been found by experience and by calculation by these methods or others [7, 8] to give errors not in excess of 0.01 Å (from three-dimensional series) for the coordinates of the heaviest atoms in a structure, or 0.02-0.03 Å for projections. The structure may contain heavy, medium, and light atoms, in which case the errors for the medium atoms are much as for x-ray methods, those for the heavy ones are rather larger, and those for the light ones are reduced by factors of two or three. This again shows that light atoms are readily detected in the presence of heavy ones by electron diffraction.

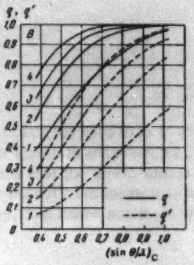

Fig. 2. Relation of q (solid lines) and q' (broken lines) to $(\sin\theta/\lambda)_c$ and to B for two-dimensional series.

Conclusions

A universal relation $kZ^{\alpha}q$ (in which Z is the atomic number) may be used to compute the accuracy for two- and three-dimensional Fourier series in electron diffraction via integral characteristics for the distribution of potential in the atom (mean squares of the potential and of the first derivative, potential and second derivative of the potential at the center of the atom). Here, k, α, and q are parameters, the last relating to cutoff; values are given for these for each of the characteristics listed above for several values of B, the temperature factor.

These characteristics are used in working formulas for the accuracy of series for the potential and atomic coordinates, the reliability factor being used as an estimate of the experimental error. The parameters are presented as tables and graphs.

LITERATURE CITED

1. B. K. Vainshtein, "Quantitative relations in Fourier series for the electron density in a

crystal," ZhÉTF, 27, 44-61 (1954).
2. B.K. Vainshtein, "Atomic scattering factors for electrons," ZhÉTF, 25, 157-168 (1953).
3. B.K. Vainshtein, "Examination of the lattice potential by electron diffraction," Tr. Inst. Kristallogr., 9, 259-276 (1954).
4. B.K. Vainshtein, "Normalization of Fourier series for the electron density," Dokl. Akad. Nauk SSSR, 93, 821-824 (1953).
5. G. Kartha, "A new method of calculating the scale factor in structure analysis," Acta Cryst., 6, 817-823 (1953).
6. B.K. Vainshtein, "Heights of peaks in electron-density and potential syntheses," Tr. Inst. Kristallogr., 11, 78-84 (1954).
7. D.W.I. Cruickshank, "The accuracy of electron density maps," Acta Cryst., 2, 65-87 (1949).
8. B.K. Vainshtein, "An electron-diffraction study of diketopiperazine," Zh. Fiz. Khim., 29, 328-344 (1956).

STRUCTURE TYPES WITH CLOSEST ATOMIC PACKING: POSSIBLE STRUCTURE TYPES FOR THE AB_4 COMPOSITION

N. L. Smirnova

M.V. Lomonosov State University, Moscow
Translated from Kristallografiya, Vol. 1, No. 5, pp. 502-505, September-October, 1956
Original article submitted February 18, 1956

We have already [1] deduced the possible structure types with the closest packing of A and B atoms for the case in which each A atom lies in a cube-octahedron of B atoms, while each B atom has four A atoms in its coordination sphere.

The same principle is used here: the closest packing allows only structure types in which each A atom is surrounded only by B atoms, while each B atom has at least one A atom in its coordination sphere. Detailed consideration is given to the case in which each B atom has three A atoms adjacent to it; then each B has $\frac{1}{3}$ of an A atom, while each A atom has $\frac{1}{3} \cdot 12 = 4$ B atoms. The composition is AB_4.

Consider a close-packed layer; if a B atom is surrounded only by B atoms in such a layer, it can have not more than two A atoms adjacent to it in its coordination sphere in the three-dimensional array.

It may be shown that, if a B atom in a layer has three A atoms adjacent to it, there are B atoms each having four A atoms in the coordination sphere in space. Figure 1a shows that atoms of types 1 and 2 must be A in cubic close packing, because any deviation from this would mean that atoms of types 3 and 4 would have no A atom adjacent in the layer. But then the B atoms of type 5 each have four A atoms in the coordination sphere in space. The same occurs for hexagonal close packing (Fig. 1b). Atoms of type 1 in the layers above and below must be A, but then the B atoms of type 5 have four A neighbors each.

Thus, a B atom has either one or two adjacent A atoms within a layer; in the latter case, the hexagons of B atoms around the A atoms are joined at vertices or along sides.

Joints at vertices give rise to B atoms each having four A atoms in the coordination sphere. Figure 2 shows that the type 1 atoms cannot be B, because they cannot have more than one adjacent A within a layer, and hence not more than two in

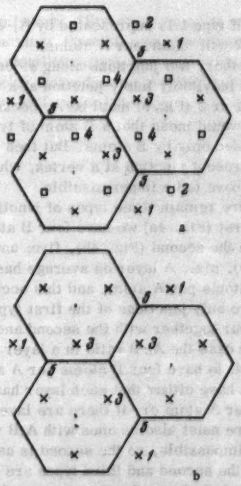

Fig. 1. (a) Cubic close packing; (b) hexagonal close packing. The centers of the hexagons in the middle layer are A atoms, while the vertices are B atoms.

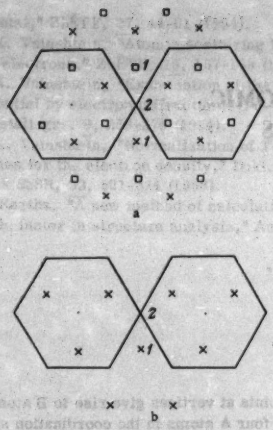

Fig. 2. (a) Cubic close packing; (b) hexagonal close packing. The centers of the hexagons are A atoms, the vertices being B.

space. If type 1 is represented by A, each B atom of type 2 will touch four A atoms.

Further, two junctions along sides that are not parallel inevitably imply junction at a vertex; atoms of type 1 or 2 (Fig. 3) must be A, because any other results would mean that a B atom of type 3 would be surrounded only by B atoms. But then point 4 or 5 will represent junction at a vertex, which we have shown above to be impermissible.

There remain three types of junctions (Fig. 4); in the first (Fig. 4a) we have four B atoms per A atom; in the second (Fig. 4b), five; and in the third (Fig. 4c), six. A layer on average has at least four B atoms per A atom, and this occurs when there are only junctions of the first type. These may occur together with the second and third types, in which case the A : B ratio in a layer would be less than 1 : 4; to have four B atoms per A atom in space, we must have either that each layer has four B atoms per A atom or, if there are layers with A:B > 1:4, there must also be ones with A:B < 1:4. The first is impossible, so the second is as well; junctions of the second and third types are therefore eliminated, to leave the first type as the only one possible within a layer (Fig. 5). The next layer of this type is superimposed in such a way as to give each B atom three A neighbors. Only one mode of

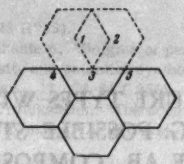

Fig. 3. The centers of the hexagons are A atoms, the vertices being B; the broken lines indicate hexagons of B atoms that occur if atoms 1 and 2 are of type A.

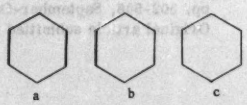

Fig. 4. Possible types of junction in a close-packed layer: junction along sides.

superposition is possible in cubic close packing and in hexagonal (Figs. 6 and 7); both figures show the unit cells and the hexagons in the lowest layer, the numbers 0,1,2, etc., representing A atoms in layers 0,1,2, etc. The repeat distance perpendicular to a layer is 15 layers for the cubic case and 10 for hexagonal. The structure type in the first case is described as follows: $a = a_C\sqrt{8}/3$; $c = a_C$; space group I4/m; n = 2; A at 2(*a*); B at 8(h): x = 0.4, y = 0.2. This is known under the name Ni_4 [2] and has several representatives. The unit cell is monoclinic in the second case (Fig. 8): $a = \sqrt{4c_h^2 + a_h^2}$; $b = a_h\sqrt{3}$, $c = \sqrt{4a_h^2 + c_h^2}$; $\beta = 67°49'$; space group

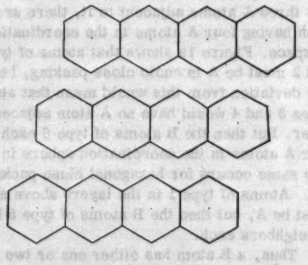

Fig. 5. Array of A and B atoms in a layer for junctions of the type of Fig. 4a; the centers of the hexagons are A atoms, the vertices being B atoms.

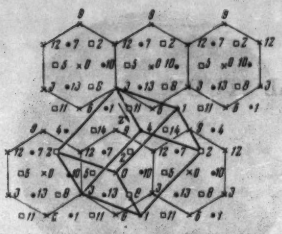

Fig. 6. Possible structure type for AB_4 with cubic close packing: x – layers 0,3,6,9,15; ● – layers 1,4,7,10,13; □ – layers 2,5,8,11,14.

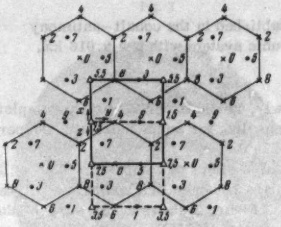

Fig. 7. Possible structure type for AB_4 with hexagonal close packing: x – layers 0,2,4,6,8,10; ● – layers 1,3,5,7,9; △ – inversion centers at which the vertices of the cell lie, the adjacent numbers being the heights with the distance between adjacent layers taken as unit.

Fig. 8. Unit cell of the possible structure type for AB_4 with hexagonal close packing, the numbers being the heights as fractions of the cell parameter; ○ – A; x – B_I; □ – B_{II}.

C2/c; n = 4; A at 4(e): 0 y ¼, y = ⅚, B_I at 8(f): xyz, x = 0.1, y = ⅓, z = 0.1; B_{II} at 8(f): x = 0.3, y = ⅔, z = 0.3. The literature appears to carry no evidence for representatives of this type.

There are thus two structure types possible for AB_4 subject to the above conditions.

We are indebted to Academician N. V. Belov and Professor G.B. Bokii for valuable advice and comments.

LITERATURE CITED

1. N.L. Smirnova, "Structure types in atomic close packing. Possible structure types for AB_3," Kristallografiya, 1, 2, 165-170 (1956).
2. G.B. Bokii, Introduction to Chemical Crystallography [in Russian] (1954).

MICROSCOPE AND X-RAY STRUCTURAL STUDY OF COBALT-ANTIMONY ALLOYS

N. N. Zhuravlev

M. V. Lomonosov State University, Moscow

Translated from Kristallografiya, Vol. 1, No. 5, pp. 506-508, September-October, 1956
Original article submitted May 19, 1956

Three compounds, CoSb, $CoSb_2$, and $CoSb_3$ are established in the cobalt-antimony system. The compound $CoSb_3$ crystallizes in the cubic system with $a = 9.016$ kX.

According to data of Podkopaev [1], Lewkonja [2], and Losev [3], two compounds, CoSb and $CoSb_2$, can crystallize in the Co-Sb system. In the range 70 to 95 wt.% Sb, between the peritectic and eutectic horizontals (894 and 618°C, respectively, Fig. 1), Losev [3] noticed a thermal effect at varying temperatures (~770°C); he ascribed this to a polymorphic transformation of the compound $CoSb_2$. Since two other workers [1, 2] had failed to observe this phenomenon, it was inserted into the phase diagram as "possible" only [4].

Our own microscopic and x-ray structural studies of several cobalt-antimony alloys offered no confirmation of the polymorphism of compound $CoSb_2$. In our view, the thermal effect at ~770°C should be attributed not to a polymorphic transformation of the compound $CoSb_2$, but to a peritectic reaction involving formation of crystals of a third compound corresponding to composition $CoSb_3$.

Preparation of the Alloys

Cobalt and antimony were fused together in various ratios from small concentrations of Co to 50 at.% in quartz ampoules with an argon atmosphere. Both slowly and quickly cooled alloys were studied.

Structural Investigation

Alloys containing less than 13.89 wt.% Co consist of $CoSb_3$ crystals and the eutectic $CoSb_3$-Sb. With increasing Co content, the quantity of precipitating $CoSb_3$ crystals rises. The peritectic reaction for the formation of $CoSb_3$ crystals proceeds very slowly, and in order to pass to completion requires annealing for some hours at a temperature close to 770°C.

Annealed alloys of composition $CoSb_3$ (13.89 wt.% Co) are homogeneous and have a polyhedral structure. Figure 2 shows a micrograph taken at magnification 140 with light polyhedral crystals of $CoSb_3$; the dark regions are pores.

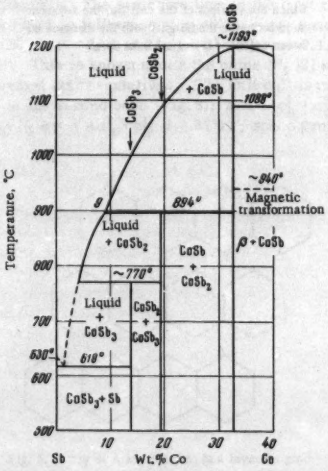

Fig. 1

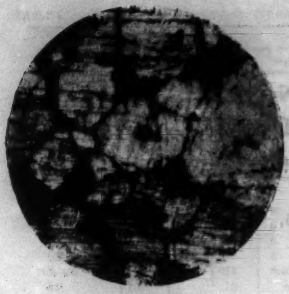

Fig. 2

Fig. 3

An x-ray photograph with more than 40 clear lines was obtained from an annealed sample of $CoSb_3$ by the powder method in a 114.4-mm diameter camera, using CuK_α radiation. On calculating and indexing the diffraction picture, it proved that the crystals belonged to the cubic system. The unit cell was body-centered with spacing $a = 9.016 \pm 0.003$ kX and contained eight $CoSb_3$ units, i.e., 32 atoms of Co and Sb. Indexing the powder photographs and noting the extinctions showed that the structure belonged to one of the two x-ray groups mI – (N102) or m3mF... (N112) [5]. Rapidly cooled alloys of composition $CoSb_3$ were heterogeneous. Figure 3 shows a micrograph of such an alloy taken at magnification 300; in the etched field of the eutectic, gray crystals of $CoSb_2$ can be seen, surrounded by a thin layer of $CoSb_3$ crystals. Annealed alloys of composition $CoSb_2$ (19.49 wt.% Co) are homogeneous and constitute the compound $CoSb_2$. In Bokii's handbook [6], there is an indication that the compound $CoSb_2$ crystallizes in the rhombic system and has the structural type of marcasite, but no values are given for the unit-cell parameters. On rapidly cooling an alloy of composition $CoSb_2$, heterogeneous structure occurred including crystals of all three compounds ($CoSb$, $CoSb_2$, and $CoSb_3$). Annealed alloys of composition $CoSb$ (32.62 wt.% Co) are homogeneous and represent the compound $CoSb$, which has the structural type of nickel arsenide [6].

TABLE 1

Compound	σ_{hyd}, g/cm³	σ_x, g/cm³	Mean microhardness, kg/mm²	Spread of microhardness, kg/mm²
$CoSb_3$	7.2	7.68	455	420–490
$CoSb_2$	7.7	–	565	520–610
$CoSb$	8.6	8.93	580	520–660

Density and Microhardness of the Compounds

The density of the compound σ_{hyd} was determined for bars weighing 0.5 to 2 g by hydrostatic suspension [7] in carbon tetrachloride. The table shows the densities σ_{hyd} and the densities σ_x calculated from the x-ray diffraction data at room temperature. The x-ray density of $CoSb$ was calculated from data given in [6].

The microhardness of the alloys was measured on the PMT-3 with a constant indentor load of 20 g. The table shows the mean microhardness together with its scatter. We see from the table that with increasing cobalt content the density and microhardness of the compounds increase.

LITERATURE CITED

1. N.S. Podkopaev, Zhur. Russkogo Fiz.-khim. obshchestva, 38, 463 (1906).
2. K. Lewkonja, Z. Anorg. Allgem. Chem., Bd. 59 (1908).
3. K. Losev, Zhur. Russkogo Fiz.-khim. obshchestva, 43 375-388 (1911).
4. M. Hansen, Constitution of Binary Alloys [Russian translation] (1941), Vol. 1, p. 487.
5. G.S. Zhdanov and V.A. Pospelov, Zh. Éksperim. i Teor. Fiz., 15, 709 (1945).
6. G.B. Bokii, Introduction to Crystal Chemistry [in Russian] (1954), pp. 353, 394.
7. É.M. Bronshtedt-Kupletskaya, Determination of the Specific Gravity of Minerals [in Russian] (1951), pp. 43-55.

X-RAY DIFFRACTION DETERMINATION OF THE STRUCTURE OF $CoSb_3$, $RhSb_3$, AND $IrSb_3$

N. N. Zhuravlev and G. S. Zhdanov

M. V. Lomonosov State University, Moscow

Translated from Kristallografiya, Vol. 1, No. 5, pp. 509-513, September-October, 1956
Original article submitted July 4, 1956

It is shown that the compounds $CoSb_3$, $RhSb_3$, and $IrSb_3$ crystallize in the cubic system and are isostructural with $CoAs_3$.

It was shown in [1] that, in addition to the compounds CoSb and $CoSb_2$, the cobalt–antimony system contained a compound $CoSb_3$ with $a = 9.016$ kX. The chemical analogs of cobalt, rhodium, and iridium should also form compounds of composition $MeSb_3$ with antimony.

In order to prove this, we fused rhodium and iridium together with antimony in the ratio $MeSb_3$ in quartz ampoules in an argon atmosphere. The alloys of composition $RhSb_3$ and $IrSb_3$ were annealed in an argon atmosphere at 700-800°C for 5-8 h and cooled in the furnace. These annealed alloys appeared practically homogeneous in the microscope; only in individual small regions did the peritectic reaction fail to pass to completion. Powder x-ray diffraction photographs were taken of these alloys in a 57.3-mm diameter camera in CuK_α radiation; calculation and indexing of these showed that the three cubic compounds $CoSb_3$, $RhSb_3$, and $IrSb_3$ were isostructural.

For further x-ray study of the crystal structure of $CoSb_3$, $RhSb_3$, and $IrSb_3$, it was essential to have fairly pure powders of each phase. In order to obtain these we prepared alloys richer in antimony than $MeSb_3$. From microscopical data, these alloys consisted of $MeSb_3$ and antimony crystals. The $MeSb_3$ crystals were separated from the alloy by dissolving the antimony in aqua regia.

Using the pure crystalline phases of $CoSb_3$, $RhSb_3$, and $IrSb_3$ obtained in this way, x-ray powder photographs were obtained in a 114.4-mm diameter camera in CuK_α radiation; these contained more than 40 sharp lines. The x-ray lines were indexed on a bcc cell. The accurate lattice spacings are shown in Table 1.

The interplanar spacings calculated from these data agreed closely with the measured values (Table 2).

The density of the $CoSb_3$, $RhSb_3$, and $IrSb_3$ crystals was determined by hydrostatic weighing in carbon tetrachloride, and the results are given in Table 1. The unit cells of $CoSb_3$, $RhSb_3$, and $IrSb_3$ contain eight formula units. Inspection of known structures of composition AB_3 and comparison of their unit cells with those of $CoSb_3$, $RhSb_3$, and $IrSb_3$ showed that these latter compounds are isostructural with $CoAs_3$ [2, 3].

The positions of the atoms in the space group $Im3(T_h^5)$ for the $CoAs_3$ type of structure are as follows [3] (Fig. 1):

Co 8 : (c) $\frac{1}{4}$, $\frac{1}{4}$, $\frac{1}{4}$, etc. (without parameters)

As 24 : (g) Oyz, etc.

The structure amplitude depends on parameters y and z, determining the positions of the Sb atoms.

The line intensities were calculated from the formula

$$I \sim L_p \cdot p \cdot F^2,$$

where L_p is the Lorentz factor and p the recurrence factor for parameter values $y = 0.35$ and $z = 0.15$.

Comparison between the calculated and measured intensities (Table 2) shows satisfactory general agreement. Occasional discrepancies are

TABLE 1

Compound	a in kX	σ_{hyd}, g/cm³	σ_x, g/cm³
$CoSb_3$	9.016±0.002	7.2	7.69
$RhSb_3$	9.211±0.002	7.5	7.96
$IrSb_3$	9.230±0.002	8.9	9.41

TABLE 2

hkl	$CoSb_3$				$RhSb_3$				$IrSb_3$			
	d_{calc}	d_{exp}	I_{calc}	I_{exp}	d_{calc}	d_{exp}	I_{calc}	I_{exp}	d_{calc}	d_{exp}	I_{calc}	I_{exp}
110	6.37	–	418	–	6.51	6.48	418	v.w.	6.53	–	418	–
200	4.51	–	14.5	–	4.60	4.59	212	v.w.	4.61	4.57	1158	w.
211	3.68	3.67	233	v.w.	3.76	3.73	241	v.w.	3.77	3.76	241	v.w.
220	3.19	–	0.4	–	3.25	3.25	87	v.w.	3.26	3.25	774	v.w.
310	2.85	2.84	2682	v.s.	2.91	2.90	2822	v.s.	2.92	2.91	2822	s.
222	2.60	–	10.6	–	2.66	2.65	92	v.w.	2.66	2.65	438	v.w.
321	2.41	2.40	647	med.w.	2.46	2.46	704	s.	2.46	2.46	704	s.
400	2.25	–	2.3	–	2.30	–	8.8	–	2.31	2.30	127	w.
411; 330	2.12	2.12	241	w.	2.17	2.16	253	w.	2.17	2.17	253	w.
420	2.02	2.01	706	s.	2.06	2.06	1207	med.s.	2.06	2.06	2414	s.
332	1.92	2.92	264	s.	1.96	1.96	277	w.	1.97	1.96	277	w.
422	1.84	1.84	309	s.	1.88	1.87	643	med.s.	1.88	1.89	1450	w.
510; 431	1.77	1.76	952	med.w.	1.80	1.80	1.053	med.s.	1.81	1.81	1053	med.w.
521	1.65	–	12	–	1.68	–	14	–	1.68	–	14	–
440	1.59	–	21	–	1.63	–	1	–	1.63	–	39	–
530; 433	1.54	1.54	256	med.w.	1.58	1.58	287	med.s.	1.58	1.58	287	med.w.
600; 442	1.50	1.50	217	s.	1.53	1.53	126	w.	1.54	1.54	70	w.
611; 532	1.46	1.46	20	v.w.	1.49	1.49	21	v.w.	1.50	1.45	21	v.w.
620	1.42	1.42	60	v.w.	1.45	1.45	150	w.	1.46	1.49	431	med.s.
541	1.39	–	48	–	1.42	–	53	–	1.42	–	53	–
622	1.36	1.36	74	w.	1.39	1.39	170	s.	1.39	1.39	442	med.s.
631	1.33	1.33	332	med.s.	1.36	1.36	369	med.s.	1.36	1.36	369	med.s.
444	1.30	1.30	165	v.w.	1.33	1.33	237	w.	1.33	1.33	382	s.
710; 550; 543	1.27	1.27	124	w.	1.30	1.30	135	w.	1.30	1.30	135	w.
640	1.25	1.25	91	v.w.	1.28	1.28	182	w.	1.28	1.28	414	med.s.
721; 633; 552	1.227	1.225	103	w.	1.25	1.25	107	w.	1.25	1.25	107	w.
642	1.205	–	5	–	1.23	–	6	–	1.23	1.23	135	w.
730	1.184	1.183	271	s.	1.21	1.21	295	s.	1.21	1.21	295	med.s.
732; 651	1.145	1.145	160	s.	1.17	1.17	171	s.	1.17	1.17	171	s.
800	1.127	–	59	–	1.15	1.15	90	w.	1.15	1.15	153	s.
554; 741; 811	1.110	–	47	–	1.134	1.132	51	v.w.	1.136	1.136	51	v.w.
820; 644	1.093	1.093	79	w.	1.117	1.116	167	s.	1.119	1.119	425	c.
653	1.078	1.077	59	w.	1.100	1.100	60	w.	1.103	1.103	60	w.
822; 660	1.062	1.062	191	med.s.	1.085	1.085	277	med.s.	1.088	1.088	503	c.
831; 750; 743	1.048	1.048	407	med.s.	1.070	1.069	416	med.s.	1.073	1.072	416	med.s.
662	1.034	–	4	–	1.056	–	24	–	1.058	1.058	104	v.w.
752	1.021	–	8	–	1.043	–	8	–	1.045	–	8	–
840	1.008	–	4	–	1.030	–	1	–	1.032	1.031	37	v.w.
833; 910	0.995	0.995	108	s.	1.017	1.018	109	s.	1.019	1.019	109	s.
842	0.984	–	28	–	1.004	1.003	85	v.w.	7.007	1.006	272	s.
921; 761; 655	0.972	0.972	59	v.w.	0.993	0.993	60	v.w.	0.995	0.995	60	v.w.
664	0.961	–	2	–	0.982	–	2	–	0.984	0.984	43	v.w.
930; 851; 754	0.950	0.950	76	v.w.	0.971	0.971	75	v.w.	0.973	0.973	75	v.w.
932; 763	0.930	0.930	310	med.s.	0.950	0.949	317	med.s.	0.952	0.952	317	med.s.
844	0.920	0.920	17	v.w.	0.940	0.939	46	w.	0.942	0.942	143	s.
941; 853; 770	0.911	0.911	115	s.	0.931	0.931	114	s.	0.932	0.932	114	s.
00 10; 068	0.902	–	61	–	0.921	0.920	49	v.w.	0.923	0.922	80	w.
11 10; 277	0.893	–	43	–	0.912	0.912	40	v.w.	0.914	–	40	–
02 10; 268	0.884	–	25	–	0.903	0.903	53	v.w.	0.905	0.905	237	s.
059; 349	0.876	0.876	53	w.	0.894	0.894	52	w.	0.896	0.896	52	w.
22 10; 668	0.867	0.867	61	w.	0.886	–	34	–	0.888	0.888	39	v.w.
13 10; 259; 567	0.859	0.859	342	med.s.	0.878	0.878	301	med.s.	0.880	0.880	301	med.s.
178; 558; 477	0.844	0.845	81	v.w.	0.862	0.862	64	v.w.	0.865	0.865	64	w.
04 10; 468	0.837	0.837	264	s.	0.855	0.855	425	med.s.	0.857	0.857	924	w.
169; 33 10	0.830	0.830	177	med.s.	0.848	0.848	153	s.	0.849	0.849	153	s.
24 10	0.823	0.833	425	med.s.	0.840	0.840	549	med.s.	0.842	0.842	1005	c.
01 11; 378; 459	0.816	0.816	351	med.s.	0.834	0.834	252	s.	0.835	0.835	252	s.
12 11; 15 10; 369	0.8032	0.8032	160	s.	0.820	0.820	127	w.	0.822	0.822	127	c.
088	0.7989	–	66	–	0.814	0.814	84	v.w.	0.816	0.816	190	c.
079; 03 11	0.7907	0.7907	364	c.	0.808	0.808	228	med.s.	0.809	0.809	288	med.s.
288; 44 10	0.7847	0.7847	528	s.	0.8017	0.8015	230	s.	0.803	0.803	274	s.
279; 23 11; 35 10; 677	0.7789	0.7789	735	v.s.	0.7957	0.7954	404	med.s.	0.7973	0.7972	404	med.s.
06 10; 668	0.7731	0.7331	671	s.	0.7898	0.7897	428	med.s.	0.7915	0.7916	882	c.
14 11; 578	–	–	–	–	0.7841	0.7840	307	w.	0.7857	0.7857	307	w.
26 10	–	–	–	–	0.7784	0.7784	804	v.s.	0.7801	0.7803	1793	v.s.
569	–	–	–	–	0.7730	0.7730	538	c.	0.7746	0.7746	538	med.s.

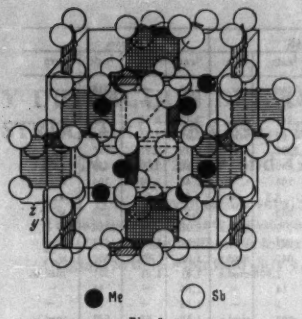

Fig. 1

probably connected with slight deviations of the antimony parameters from the values taken above. The hemihedral space group of skutterudite and its analogs is responsible for the appearance of lines with the same absolute indices but different signs (and hence different structure factors) on the Debye photographs. Hence, the parameters can only be refined by using the intensities of reflections from single crystals.

This investigation shows that a whole series of isomorphic compounds crystallize in the skutterudite structure with square arrangements of the type $[As_4]^{3-}$. It is extremely probable that compounds $RhAs_3$ and $IrAs_3$ with analogous structures also exist.

We are grateful to Engineer R. N. Kuz'min for help in carrying out the experiments.

LITERATURE CITED

1. N. N. Zhuravlev, "Microscope and x-ray structural study of cobalt–antimony alloys," Kristallografiya, 1, 5, 506-509 (1956).
2. I. Oftedal, "Die Kristallstructur von Skutterudit und Speiskobalt–Chloanthit," Z. Krist. 166, 5/6, 517 (1927/28).
3. G. B. Bokii, Introduction to Crystal Chemistry [in Russian] (1954), p. 396.

X-RAY STRUCTURAL STUDY OF LEAD DIETHYLDITHIOCARBAMATE

G. S. Zhdanov, Z. V. Zvonkova, and N. V. Rannev

L. Ya. Karpov Physicochemical Institute

Translated from Kristallografiya, Vol. 1, No. 5, pp. 514-519, September-October, 1956
Original article submitted July 13, 1956

The unit cell and space group of lead diethyldithiocarbamate were determined. A general solution is given for the structure. The Pb–S bonds have a pyramidal disposition.

Lead diethyldithiocarbamate

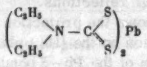

belongs to the class of salts of dithiocarbamic acid

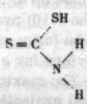

in which the hydrogen atoms of an amino group are replaced by organic radicals, C_2H_5 groups. Free and thiosubstituted carbamic acids are unstable compounds and cannot be separated in the free state; their salts, however, are stable compounds. These dissolve easily in organic solvents (some of them simply in water), melt easily, and enjoy wide practical use in accelerating the vulcanization of rubber, as insectofungicides, medicinal substances, etc. This group of compounds has been little studied as regards physical and chemical properties and atomic structure.

Cambi and Malatesta [1] studied a number of dithiocarbamate compounds. With the help of x-ray analysis they established isomorphism between the salts of tervalent iron and cobalt. A study of magnetic moments led to certain conclusions regarding the nature of the chemical bond in the molecules.

$(R_2NCS_2)_3Co$, $\mu = 0$
$(R_2NCS_2)_3Fe$, $\mu = 5.5$ (Bohr magnetons)

In the compound with tervalent cobalt, the covalent type of bond predominates, $\mu_{Co}^{hyd} = 0$. In the second compound the bond was assigned an ionic nature, since this agrees with the magnetic moment of the Fe^{+++} ion in aqueous solution, $\mu = 5.9$ [2].

Later investigations, however, associated the magnetic moment in iron complexes with the existence of covalent bonds [3]. The isomorphism was explained by the fact that the octahedral bonds of the metal atoms had similar directions.

The lead atom is characterized by the following occupation of valence orbits:

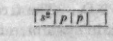

this allows a different configuration of the bonds in the molecules and crystalline compounds, namely, a triangular configuration with p^2 electron orbits, as observed in the structure of $PbCl_2$. As a result

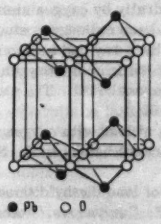

● Pb ○ O

Fig. 1. Structure of PbO.

TABLE 1

Formula	Crystal system	Spacings, A			Angle β	Space group	No. of molecules Z	Density	
		a	b	c				σ_x	σ
$[(C_6H_5)_2NCS_2]_2Pb$	Monoclinic	9.55	11.75	14.72	96°	C_{2h}^5 — $P2_1/c$	4	2.02	2.04

of the unpairing of the s^2 electrons, tetrahedrally directed sp^3 bonds are formed, as established by Zhdanov and Ismailzade [4] in the structure of tetraphenyl lead $Pb(C_6H_5)_4$ and also in $Pb(CH_3)_4$ [5] and $Pb_2(CH_3)_6$ [6].

Pyramidally directed bonds were also established for Pb, for example in the oxide PbO. Moore and Pauling [7] showed that in the PbO structure the lead atoms lay at the vertex of a square pyramid, the base of which comprised four oxygen atoms, the angles O–Me–O being 118 and 75° (Fig. 1).

The metal atom forms four electron orbits directed toward the base of the pyramid, the vertex of which is occupied by an unshared pair of electrons. The oxide SnO has the same structure.

In another form of lead oxide, the lead atom is connected with three oxygen atoms in the rhombic system.

Cox [8] considered the dimensions of the unit cell of the complex lead oxalate $K[Pb(C_2O_4)_2]_4$ and concluded that the four Pb–O bonds had plane configuration; the atomic structure of this compound was not solved, however, and this bond configuration could not be proved.

Byström and Evers [9] studied the structures of Ag_2PbO_2 and $Ag_5Pb_2O_6$. The first compound belongs to the monoclinic system, and the position of the oxygen atoms relative to the lead is the same as in tetragonal PbO. The oxygen atoms form severely distorted tetrahedra; the lead atoms, however, lie outside these. The structure of $Ag_5Pb_2O_6$ is tetragonal, and the lead atoms in this are surrounded octahedrally by oxygen atoms.

Shirane [10] and colleagues studied the structure of $PbTiO_3$ by x-ray and neutron diffraction. The configuration of the lead and oxygen atoms was the same as in tetragonal PbO. The shortest Pb–O distance was 2.53 Å.

Compounds of lead with oxygen analogs (sulfur, selenium, tellurium) belong to the NaCl-type structure [11, 12].

Specimens of lead diethyldithiocarbamate obtained from E. N. Gur'yanova (Molecular-Structure Laboratory) were recrystallized in benzene. The crystals had the form of hexahedral prisms of dimensions 0.6 × 0.8 × 1 mm. Table 1 gives the x-ray data.

In addition to this, crystals with unit-cell dimensions $a = 9.55$, $b = 11.75$, $c = 44.1$ Å, containing 12 molecules, were found.

In x-ray rotation photographs taken along the [100], the odd layer lines were very severely weakened, owing to the disposition of the lead atoms in positions $x = 1/4$ and $3/4$. The Laue photographs reveal pseudo-symmetry planes due to the same heavy lead atoms.

The structure was solved by means of F^2 series. The initial data included the measured intensities of 82 0kl and 86 h0l reflections.

Figure 2 shows the projection of the interatomic-vector function on the (100) plane, from which the configuration of the Pb–S bonds was determined The Pb Atom lay at the vertex of a four-sided pyramid having a base made up of four S atoms.

The maxima in the (010) projection were poorly resolved owing to the large superposition number of interatomic vectors for a small number of terms in the series. The maxima corresponding to the S atoms in the (100) projection were unresolved as a result of the superposition of two pairs of atoms. S_I, S_{II}, and S_{III}, S_{IV}.

Tetrahedral disposition of the S atoms around the lead atom was excluded owing to the positioning

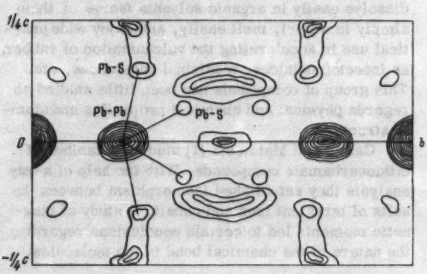

Fig. 2. Projection of F^2 series on the (100) plane.

TABLE 2

Atoms	Projection (100)		Projection (010)	
	y	z	x	z
Pb	0.112	0	0.250	0
S_I	0.16	0.13	0.47	0.13
S_{II}	0.29	0.94	0.07	0.94
S_{III}	0.16	0.13	0.03	0.13
S_{IV}	0.29	0.94	0.42	0.94

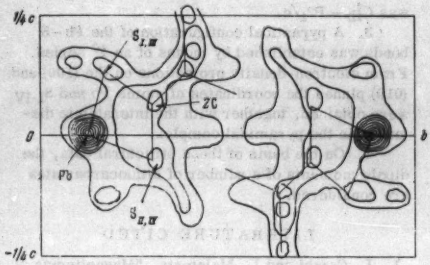

Fig. 3. Electron-density projection on the (100) plane.

of the Pb atoms indicated above. Plane configuration of the Pb–S bonds was not supported by the projection on the (010) plane.

The electron-density projection on the (100) plane, constructed with structure-amplitude signs determined from the coordinates of the heavy atom (lead), excluded triangular configuration of the Pb–S bonds and supported pyramidal configuration. A refined electron-density series was then constructed, the signs of the structure amplitudes being corrected in accordance with the S coordinates obtained

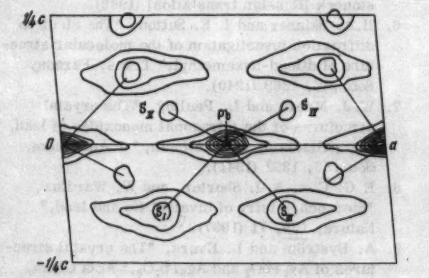

Fig. 4. Electron-density projection on the (010) plane.

TABLE 3

Atoms	Å
Pb — Pb	4.25
Pb — $S_{I, III}$	2.7
Pb — $S_{II, IV}$	2.8
S_I — S_{II}	3.5
S_I — S_{III}	3.3
S_{II} — S_{IV}	3.3

from the pyramidal model. A (010) electron-density projection was also constructed.

From these projections (Figs. 3 and 4) the coordinates of the Pb, S_I, S_{II}, S_{III}, and S_{IV} atoms were obtained (see Table 2).

The interatomic distances obtained are given in Table 3.

The (100) electron-density projection contained maxima corresponding to some of the light atoms and also superfluous maxima due to truncation waves.

The dependence of these superfluous maxima on the truncation wave is made clear by constructing the theoretical electron-density series, using the coordinates of the heavy lead atom.

The resolving power of the series is reduced owing to the absence of reflections 0k*l* and h0*l* with $k + l = 2n + 1$ and $h = 2n + 1$ (required for space group $C_{2h}^5 - P2_1/c$) as a result of the large difference between the scattering power of the Pb atoms and the other atoms in the structure.

The maxima on the (010) projection were more poorly resolved on account of the superposition of atoms of neighboring molecules.

Geometrical analysis of the structure confirmed the model obtained from the electron-density projection. Figure 5 shows the disposition of the molecules in the unit cell.

In this way we found that the structure of lead dithiocarbamate contains a pyramidal configuration of the lead–sulfur bonds analogous to that earlier established for lead oxide.

A review of crystal chemistry [13] indicated the desirability of studying whether this configuration could occur in finite complexes, since it had formerly only been established for layered structures of metal oxides with infinite lattices of oxygen atoms. This we have done in the present paper, which is the first to indicate tetrahedral–pyramid configuration in a lead complex.

The interatomic distance Pb – Pb = 4.95 Å indicates the absence of any chemical bond between the lead atoms, such as occurs in the compound

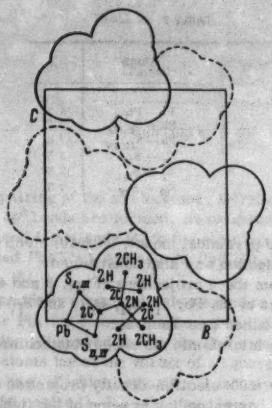

Fig. 5. Disposition of the molecules in the unit cell [(100) plane].

$Pb_2(CH_3)_6$, where we have 2.88 Å [6]. Here this distance exceeds the atomic diameter of lead still more on account of the way in which the molecules are packed in the cell.

The Pb–S bond has a predominantly covalent character, as confirmed by the directional properties of the valences and the interatomic distances. For the ionic type of bond with coordination number 6, the Pb–S distance equals 3.08 Å [11].

Analysis of the interatomic distances in lead dithiocarbamate shows that the Pb–S bonds are realized with a deficit in the number of electrons; hence, on hybridization of the bonds, an unshared pair of electrons may be retained in the Pb, since on formation of the tetrahedral bonds all the valence electrons of the Pb atom take part in these bonds.

Table 4 [14] gives the values of the dipole moments for a series of compounds of dithiocarbamate salts.

The Pb–S bond has an intermediate character between covalent and ionic; hence, the $Pb^{+\delta_1}-S^{-\delta_1}$ bond is polar. Thus, the increase in dipole moment on passing from zinc to lead is explained by the different directional properties of the valences in the molecules. As the structural studies show, the pyramidally directed Pb–S bonds explain the increase in the dipole moment.

TABLE 4

$(C_5H_{10}NS_2)_2Zn$	$\mu \cdot 10^{-18}$ 1.89
$(C_5H_{10}NS_2)_2Ni$	1.94
$(C_5H_{10}NS_2)_2Pb$	2.88
$(C_5H_{10}NS_2)_3Bi$	4.05

Conclusions

1. Single crystals of lead diethyldithiocarbamate were obtained in the form of colorless hexahedral prisms.

2. X-ray diffraction revealed a monoclinic unit cell: $a = 9.55$, $b = 11.75$, $c = 14.72$ Å; $\beta = 96°$ with $Z = 4$ molecules per cell. The space group was $C_{2h}^5 - P2_1/c$.

3. A pyramidal configuration of the Pb–S bonds was established by means of an F^2 series. From electron-density projections on the (100) and (010) planes the coordinates of atoms Pb and S_{I-IV} were obtained, together with the interatomic distances in the pyramidal complex.

4. On the basis of these structural data, the dipole moments of a number of dithiocarbamates are considered.

LITERATURE CITED

1. L. Cambi and L. Malatesta, "Magnetismus und Polymorphie der inneren Komplexsalze. Eisensalze der Ditiocarbamidsäuren," Ber., 70, 2067 (1937).
2. L. Pauling, Nature of the Chemical Bond [Russian translation] (1947).
3. R.S. Newholm, Magnetism and Inorganic Chemistry [Russian translation] (Advances in Chemistry, 25, 4, 517-544, 1956).
4. G.S. Zhdanov and I.G. Ismailzade, "Crystal structure of metalloorganic compounds. I. X-ray study of crystals of tetraaryl compounds of silicon, tin, and lead," Zh. Fiz. Khim., 24, 12, 1495-1501 (1950).
5. A.F. Wells, Constitution of Inorganic Substances [Russian translation] (1949).
6. H.A. Skinner and L.E. Sutton, "The electron diffraction investigation of the molecular structure of dilead-hexamethyl," Trans. Faraday Soc., 36, 1209 (1940).
7. W.J. Moore and L. Pauling, "The crystal structures of the tetragonal monoxides of lead, tin, palladium, and platinum," J. Am. Chem. Soc., 63, 1392 (1941).
8. E.G. Cox, A.J. Shorter, and W. Wardlaw, "Stereochemistry of bivalent tin and lead," Nature, 139, 71 (1937).
9. A. Byström and L. Evers, "The crystal structures of Ag_2PbO_2 and $Ag_8Pb_2O_6$," Acta Chem. Scand., 4, 4, 613 (1950).

10. G. Shirane, R. Pepinski, and B.C. Franzer, "X-ray and neutron diffraction study of ferroelectric $PbTiO_3$," Acta Cryst., 9, 131 (1956).
11. G.B. Bokii, Introduction to Crystal Chemistry [in Russian] (1954).
12. B.F. Ormont, Constitution of Inorganic Substances [Russian translation] (1950).
13. G.M. Powell, "Inorganic structures," Collection: New Studies in Crystallography and Crystal Chemistry [Russian translation](1951), Vol. 3, p. 20.
14. L.S. Kuzina, Dissertation: Isotopic Exchange of Sulfur and Certain Derivatives of Dithiocarbamic Acids and Their Structure [in Russian] (L. Ya. Karpov Physicochemical Institute).

SOVIET PHYSICS – CRYSTALLOGRAPHY VOL. 1, NO. 5 SEPT.-OCT., 1956

ISOMORPHISM OF THE FERRATES AND TITANATES OF STRONTIUM, BARIUM, AND LEAD

E. G. Fesenko and O. I. Prokopalo

Scientific-Research Physicomathematical Institute at the
V.M. Molotov State University, Rostov
Translated from Kristallografiya, Vol. 1, No. 5,
pp. 520-523, September-October, 1956
Original article submitted July 14, 1956

Lead ferrate was obtained and its electrical properties studied, together with those of barium and strontium ferrates.

The remarkable dielectric properties of compounds with the perovskite-type structure stimulate a search for new compounds with this type of structure. A recent communication [1] described the synthesis of barium ferrate in two forms, tetragonal and hexagonal, and also the production of strontium ferrate [2]. The x-ray structural work described in these papers showed that the parameters of the compounds in question were extremely close to those of the corresponding titanates.

The present investigation was undertaken in order to synthesize lead ferrate (this has not hitherto been done, so far as we know) and study its electrical properties together with those of barium and strontium ferrates.

As original components for the synthesis we took carbonates of Sr, Ba, and Pb, and also Fe_2O_3 (all of analytical grade). The latter was subjected to chemical analysis for iron content and the data of the analysis were taken into account in calculating the components. Roasting took place in an oxygen atmosphere. A sample of stoichiometric composition $SrFeO_3$ was obtained on roasting for 1 h at 1200°C; $BaFeO_3$ was roasted for 4 h at 950°C, and $PbFeO_3$ for 1 h at 1000°C.

The x-ray photographs were taken by the powder method in an 86-mm diameter x-ray camera using Cu and Fe K_α radiation. The photographs of all three substances contained very weak lines of Fe_2O_3 and the oxides of Sr, Ba, and Pb, respectively. This indicated that the conditions specified had taken the reaction to a fair conclusion, although the samples obtained were not analyzed chemically.

In all our attempts at preparing barium ferrate the cubic form was always obtained. We were unable to produce the hexagonal and tetragonal modifications, in spite of observing the conditions specified in [1]. We did establish a variation of the lattice spacing of cubic barium ferrate with roasting temperature. The spacing a varied linearly from 4.007 Å (950°C) to 4.010 Å (1150°C). The cubic form of $BaTiO_3$ showed a variation of the opposite kind. As we know [3], the cubic form of barium titanate can be obtained from $Ba(OH)_2 \cdot 8H_2O$ and TiO_2 at 400°C. We found that a sample obtained at this temperature had $a = 4.014$ Å and one obtained at 800°C had $a = 4.010$ Å. The different effects of the roasting temperature may be explained by the fact that, in barium ferrate, there is a partial transformation of the quadrivalent iron into tervalent on heating above the formation temperature, corresponding to a weakening of the interatomic forces. In the case of $BaTiO_3$, heating above 400°C leads to ordering of the structure.

The parameters obtained for our substances are given in Table 1, which, for comparison, also contains data for the forms of barium ferrate and titanate given in [1] and [4].

The data in the table illustrate the complete isomorphism of the ferrates and titanates and show that the cell volumes of the ferrates are smaller than those of the corresponding titanates. At the same time we notice the extremely small change in spontaneous deformations on replacement of the octahedral ion.

This similarity is based on the common nature of the chemical bond in titanates and ferrates; in the BO_3 groups, where B = Fe or Ti, the bond in both cases is effected by 4s and 3d electrons. The difference observed is due to the fact that the state of

TABLE 1

Modification	Spacings (Å)	Stoichiometric composition					
		$SrTiO_3$	$SrFeO_3$	$BaTiO_3$	$BaFeO_3$	$PbTiO_3$	$PbFeO_3$
Cubic	a	3.905	3.869	4.010	4.007	—	—
Tetragonal	a	—	—	3.994	3.98	3.900	3.887
	c	—	—	4.034	4.01	4.151	4.123
	c/a	—	—	1.010	1.01	1.064	1.060
Hexagonal	a	—	—	5.74	5.68	—	—
	c	—	—	14.05	13.86	—	—

the Ti ion is energetically more favorable in establishing the bond.

Comparison of the lattice parameters of the titanates and ferrates enables us to estimate the radius of the Fe^{4+} ion, regarding which data obtained by interpolation with respect to the radii of Mn and V ions exist in [2]. The radius of the Fe^{4+} ion may also be estimated from the volume of the octahedral cavity which it occupies. By comparing the lattice spacings of $BaFeO_3$ and $BaTiO_3$ [1], it was earlier suggested that the radius of Fe^{4+} was smaller than that of Ti^{4+}. This selection of material, however, was unfortunate, since, for barium titanate Gol'dshmidt's geometrical criterion t exceeds unity, and hence the dimensions of the central ion can only indirectly influence the cell size. It is better to estimate the radius of Fe^{4+} from strontium titanate and ferrate, for which $t < 4$.

The lattice spacings of the cubic forms found experimentally and calculated from the ionic radii are, respectively, 4.010 and 4.10 Å for $BaTiO_3$ and 3.905 and 4.00 Å for $SrTiO_3$ [5]. The theoretical overestimates indicate the necessity of correcting the tabulated ionic radii used. This should be done primarily for oxygen and titanium ions. In fact, since the nature of the bond in the BO_3 groups is partly covalent [6], the oxygen–ion radius should be taken rather smaller and the titanium–ion radius rather larger than those indicated above. The same conclusion may easily be drawn from the following. It is known that the octahedral cavity in $BaTiO_3$ and the cubo-octahedral cavity in $SrTiO_3$ are somewhat free, respectively, for Ti and Sr ions. In the first of these the parameter is determined by a framework of Ba and O ions and in the second by Ti and O. Since the experimental parameters in both $BaTiO_3$ and $SrTiO_3$ are smaller, the radius of the oxygen ion must be taken rather smaller than that indicated.

From the experimental value of a for cubic $BaTiO_3$, regarding the bond between the Ba and other ions as covalent, we can estimate the average radius of oxygen as approximately 1.28 Å. The octahedral cavity occupied by titanium in $SrTiO_3$ can contain an inscribed sphere of radius 0.67 Å.

The isomorphism of $SrTiO_3$ and $SrFeO_3$ enables us (by taking the oxygen radius found) to determine the radius of the sphere corresponding to the octahedral cavity in $SrFeO_3$. This proves to be 0.65 Å. If we consider the radius of the Fe^{4+} ion to be as much below the radius of the sphere in the octahedral cavity of $SrFeO_3$ as the radius of the Ti^{4+} ion is in $SrTiO_3$, we may estimate the radius of the Fe^{4+} ion as about 0.62 Å. The Fe^{4+} radius may possibly be rather smaller, since we took the averaged parameter value for $SrFeO_3$, the lattice of which is probably defective.

In view of the isomorphism of the titanates and ferrates, we may expect that tetragonal $BaFeO_3$ and $PbFeO_3$ have phase transformations at temperatures higher than the corresponding titanates. In fact, bearing in mind the instability of quadrivalent iron, we may assume the existence of defects in the $BaFeO_3$ lattice. A result of this will be the weakening of the internal field. With increasing concentration of defects the spontaneous deformation will fall to zero. The cubic modification corresponds to this limiting case. Considering the similarity of the spontaneous deformations in the titanates and ferrates, and also the existence of defects in the latter, we come to the conclusion that the ferrates have a high temperature of the phase transformation.

The ferrate samples obtained had a high electrical conductivity. Figures 1-3 show $\ln\sigma = f(1/T)$

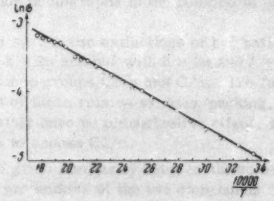

Fig. 1

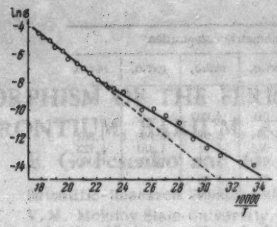

Fig. 2

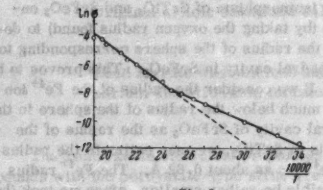

Fig. 3

curves for our ferrates of strontium, lead, and barium, respectively. The activation energies or (allowing for the large electrical conductivity) energy gaps between the normal band or local levels and the conduction band are calculated from the formula $w = [(\ln \sigma_2 - \ln \sigma_1)/(1/T_1 - 1/T_2)]k$. For strontium ferrate, w = 0.10 eV. In the temperature range 20 to 290°C, there are no changes in the mechanism of electrical conduction. The $\ln \sigma = f(1/T)$ curves for lead and barium ferrate have a break at T_0 equal to 180 and 130°C, respectively. The value of w at the break point changes from 0.50 to 0.63 eV for $PbFeO_3$ and from 0.34 to 0.60 eV for $BaFeO_3$. The existence of the break may be explained by a changeover from the normal band to the conduction band, while the electrical conduction at temperatures below T_0 is mainly determined by the distance from the conduction band to the local levels arising as a result of impurities. It is possible, however, that the break in the $\ln \sigma = f(1/T)$ curves is connected with structural changes.

At the present time, the conditions for synthesizing ferrates are being optimized with a view to studying their properties further, with the closest possible approach to the composition ABO_3.

LITERATURE CITED

1. W.W. Malinofsky and H. Kedesdy, "Barium iron oxide isomorphs of hexagonal and tetragonal $BaTiO_3$," J. Am. Chem. Soc., 76, 3090-3091 (1954).
2. L. Harry and I. Vakel, "On the structures of some compounds of the perovskite type," Acta Cryst., 8, 394-398 (1955).
3. M.C. Harewood and H.A. Klasens, Nature, 165, 73 (1950).
4. R.D. Burbank and H.T. Evans, "The crystal structure of hexagonal barium titanate," Acta Cryst., 1, 330-336 (1948).
5. N.V. Belov and G.B. Bokii, "Modern state of crystal chemistry and its immediate problems," Collection: First Congress on Crystal Chemistry [in Russian] (1954), p. 7.
6. M.A. Blokhin, "Study of the x-ray K absorption spectrum of titanium in barium and lead titanates," Dokl. Akad. Nauk SSSR, 95, 965-968 (1954).

SOVIET PHYSICS – CRYSTALLOGRAPHY VOL. 1, NO. 5 SEPT.-OCT., 1956

STRUCTURE OF DIPHENYLIODONIUM CHLORIDE AND IODIDE

T. L. Khotsyanova

Institute of Heteroorganic Compounds, Academy of Sciences of the USSR

Translated from Kristallografiya, Vol. 1, No. 5,
pp. 524-530, September-October, 1956
Original article submitted March 24, 1956

Diphenyliodonium chloride and iodide are isomorphic crystals: $(C_6H_5)_2ICl$, $a = 20.81$, $b = 5.82$, $c = 20.26$ Å, $\beta = 102.5°$, $n = 8$. $(C_6H_5)_2I-I$, $a = 22.08$, $b = 6.27$, $c = 20.42$ Å, $\beta = 101°$, $n = 8$. The space group is C2/c. These were studied by x-ray diffraction using Mo Kα radiation. In view of the isostructural connection between the two substances, only $(C_6H_5)_2ICl$ was studied completely. The coordinates of the atoms were determined by calculating a three-dimensional electron-density series containing more than 2000 independent F_{hkl} terms. The accuracy in determining the positions of the light atoms (C) was ±0.03 to 0.04 Å; that of determining the heavy atoms (I, Cl) was ±0.015 Å.

Introduction

The chemical nature of iodonium compounds manifested in exchange and decomposition reactions is of considerable interest. Thus, for diphenyliodonium chloride and iodide, as well as for some of their derivatives substituted in the benzene rings, there are some typical reactions [1,2] involving a stage in which free radicals are formed (I) and others involving heterolytic decomposition of the molecule (II):

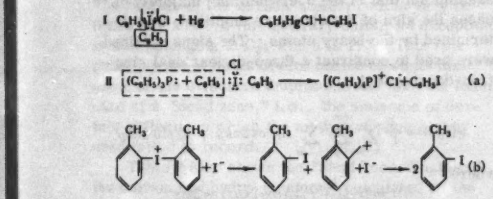

Certain physical properties and physicochemical data [3] indicate an ionic character for the halide–halide bond in diphenyliodonium halides. Apart from studying the character of this bond, it is also interesting to determine the configuration of the molecule (valence configuration of tervalent iodine, valence angles C–I–C and C–I–X).

The problem of the present x-ray diffraction study lay in establishing the configuration of the molecule in the crystal and elucidating the connection between its structure and chemical properties.

Experimental Part

Crystals of diphenyliodonium chloride and iodide, $(C_6H_5)_2I-Cl$ and $(C_6H_5)_2I-I$, were obtained by slow evaporation of the saturated solutions in ethyl alcohol. The crystals had the form of platelets [colorless for $(C_6H_5)_2I-Cl$ and yellowish for $(C_6H_5)_2I-I$] strongly drawn out in the direction of the b axis and reaching several mm in length (transverse dimensions of the order of 0.2 × 0.4 mm). The simple forms were $a\{100\}$ and $c\{001\}$. The unit-cell parameters were determined from oscillation diffraction photographs in the reciprocal-lattice camera.

The systematic extinctions of hkl reflections with $h + k \neq 2n$ and $h0l$ with $h \neq 2n$ and $l \neq 2n$ lead to two space groups, C2/c and C/c. The fact that the first of these relates to close packing, and that the crystals have no piezoelectric effect, however, leads us to choose C2/c.

The great similarity between the ac electron-density projections of the two compounds and the similarity between their unit-cell parameters indi-

	$(C_6H_5)_2I-Cl$	$(C_6H_5)_2I-I$
a	20.81±0.06 Å	22.08±0.10 Å
b	5.82±0.02 Å	6.27±0.03 Å
c	20.26±0.06 Å	20.42±0.08 Å
β	102°34'±0°30'	101°±1°
ρ_{meas}	1.67 g/cm³	—
ρ_x	1.76 g/cm³	1.95 g/cm³
n	8	8

cates that they are entirely isomorphic. Hence, only the diphenyliodonium chloride was subjected to a full structural study. The structure of the iodide was analyzed on the principle of complete isomorphism with the chloride. This is justified in view of the fact that the x and z coordinates of the heavy atoms practically coincide in the two crystals.

The crystals were photographed in Mo Kα radiation, using the reciprocal-lattice camera. The whole experimentally attainable set of reflections was recorded; by rotation around the b axis, the $h0l$, $h1l$, $h2l$, $h3l$, $h4l$, $h5l$ developments were obtained. The total number of reflections recorded was around 2000. In order to reduce the measured intensities for various layer lines to a single relative scale, a series of oscillation photographs around the b axis was used.

For converting intensities I_{hkl} into structure factors F^2_{hkl}, the Lorentz and polarization factors were taken into account.

Solutions of the Structure

The x and z coordinates of the heavy atoms (I and Cl) in the two substances were found from two-dimensional series of interatomic vectors P(x0z) and used in determining the signs of F_{h0l} for subsequent construction of electron-density series ρ (x0z). The electron-density projection on the *ac* face for diphenyliodonium chloride is shown in Fig. 1.

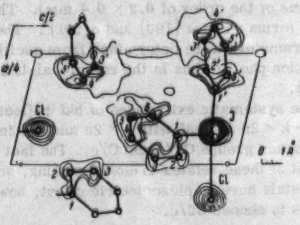

Fig. 1. Diphenyliodonium chloride. Electron-density projection ρ(x0z) for the independent part of the unit cell.

This gives a clear picture of the benzene-ring maxima as well as those corresponding to I and Cl.

The y coordinates of the iodine and chlorine atoms (in diphenyliodonium chloride only) were determined by means of a three-dimensional series of interatomic vectors (F_{hkl} series). Attempts to determine the y coordinates by means of two-dimensional series of interatomic vectors P (0yz) and P (xy0) and to calculate the one-dimensional section A ($02y\frac{1}{2}$) of the three-dimensional series by the Harker method gave no positive results.

The three-dimensional series of interatomic vectors was calculated by the formula

$$P(xyz) = \frac{4}{V}\sum_{h=0}\sum_{k=0}\sum_{l=-\infty}^{+\infty}\{(F^2_{hkl}+F^2_{h\bar{k}l})\cos 2\pi hx\cos 2\pi lz$$

$$-(F^2_{hkl}-F^2_{h\bar{k}l})\sin 2\pi hx\sin 2\pi lz\}\cos 2\pi ky.$$

The symmetry of the series was C2/m and the independent part a/4, b/2, c.

In solving the structure we were only interested in maxima corresponding to vectors between heavy atoms, a list of which is given in Table 1.

For the C^3_{2h} = C2/c group, the F^2_{hkl} series does not enable us to find the positions of the glide planes c and n directly. The correctness of the positions chosen (y = 0 for c and y = ¼ for n) was confirmed by calculating the I–I, I–Cl, and Cl–Cl distances and at a later stage the C – C distances in the "broken" benzene ring (Fig. 1).

Starting from the x and z coordinates of the I and Cl atoms determined from the electron-density projection ρ (x0z) (these values were close to those found from the F^2_{hkl} series) and the y coordinates taken from the F^2_{hkl} series, we calculated the signs of all the structure amplitudes, making the justified assumption that in the overwhelming majority of cases the sign of the structure amplitude was determined by the heavy atoms. The signs obtained were used to construct a three-dimensional electron-density series:

$$\rho(xyz) = \frac{4}{V}\sum_{h=0}\sum_{k=0}^{+\infty}\sum_{l=-\infty} A_k\cos 2\pi ky + B_k\sin 2\pi ky,$$

where

$$A_k = (F_{hkl}+F_{h\bar{k}l})\cos 2\pi hx\cos 2\pi lz$$

$$-(F_{hkl}-F_{h\bar{k}l})\sin 2\pi hx\sin 2\pi lz = 0 \text{ for } l \neq 2n,$$

$$B_k = (F_{hkl}+F_{h\bar{k}l})\sin 2\pi hx\cos 2\pi lz$$

$$+(F_{hkl}-F_{h\bar{k}l})\cos 2\pi hx\sin 2\pi lz = 0 \text{ for } l = 2n.$$

TABLE 1. Maxima of Three-Dimensional Interatomic-Vector Series

Interatomic vector	Coordinates of maximum in relative units x	y	z	Height of max., arbitrary units	Theor. "weight" of maximum	Theoretical coordinates of maxima
I—I	0	0.094	0.500	745	$4z_I^2$	$0, 2y_I, \frac{1}{2}$
I···I	0.146	0.500	0.625	674	$4z_I^2$	$-2x_I+\frac{1}{2}, \frac{1}{2}, -2z_I+\frac{1}{2}$
I—I	0.146	0.406	0.125	316	$2z_I^2$	$-2x_I+\frac{1}{2}, -2y_I+\frac{1}{2}, -2z_I$
I—Cl	0.148	0	0.023	256	$4z_I z_{Cl}$	$-(x_I-x_{Cl})-(y_I-y_{Cl})-(z_I-z_{Cl})$
I—Cl	0	0.500	0.392	246	$4z_I z_{Cl}$	$x_I+x_{Cl}-\frac{1}{2}, y_I-y_{Cl}+\frac{1}{2}, z_I+z_{Cl}-\frac{1}{2}$
I···Cl	0.148	0	0.544	161	$4z_I z_{Cl}$	$x_{Cl}-x_I, y_I+y_{Cl}, z_{Cl}-z_I+\frac{1}{2}$

The independent part of the series is $a/4$, $c/2$, b.

Since the a and c spacings of the cell are large, the corresponding axes were divided into 120 parts for calculating ρ (xyz), while the b edge was divided into 48 parts. The electron-density values were not calculated for the whole independent region, but only in sections ("prickings") parallel to the b axis passing through the regions of electron-density maxima which appeared on the ac projection. These sections contained all 14 maxima corresponding to the carbon, iodine, and chlorine atoms. The exact coordinates of the maxima were determined by interpolation, using the method described earlier [4]. The coordinates of the maxima (in relative units and Å) for the atoms of one molecule are given in Table 2, together with the heights of the maxima. The heights of the carbon-atom maxima vary between 2.1 and 3.4 (in arbitrary units); an exception is that belonging to C_4', which is 1.3. This is a consequence of an incorrect choice of signs for some of the structure amplitudes and also the existence of a "dead zone," i.e., the omission of certain reflections which the method of photography used failed to record.

Table 2 also shows the "ideal" coordinates of the carbon and hydrogen atoms[1] calculated on the assumption that the benzene rings were regular plane hexagons with side 1.40 Å and C—H bonds directed along the diagonal of the benzene ring 1.08 Å in length. The positions of the hydrogen atoms (calculated on the assumptions indicated) are required in order to study steric problems in the molecule and analyze the stacking. All the distances between atoms not connected by valences were calculated on the basis of the "ideal" positions of the carbon and hydrogen atoms.

The benzene rings observed experimentally are practically plane hexagons with the following bond lengths:

The accuracy of the heavy atom coordinates found is 0.01 Å. The accuracy for the carbon atoms (determined by the deviation of the benzene rings from the coplanar state) was 0.04 Å; hence, the differences in the C—C distances are not subject to analysis.

Calculation of the "Ideal" Carbon Atoms

The scatter in the C—C bond lengths of the benzene rings was due to experimental error (mainly incorrect choice of the signs of certain structure amplitudes) since the symmetry of the benzene rings with respect to the lines C_1—C_4 and C_1'—C_4' was slightly disturbed. In order to determine the signs of the structure amplitudes for constructing the next approximation to the electron-density series, slight corrections should be introduced into the experimental values of the carbon-atom coordinates so as to transform the benzene rings into regular plane hexagons with sides of 1.40 Å. This

[1] See below for the method of calculating "ideal" C and H coordinates.

TABLE 2. Coordinates of the Atoms of One Molecule in the Structure of Diphenyliodonium Chloride

Atom	Actual molecule						Height of maxima in arbitrary units	Ideal molecule					
	Relative units			Å				Relative units			Å		
	x	y	z	x	y	z		x	y	z	x	y	z
C_1	0.183	−0.187	0.356	3.80	−1.09	7.21	3.4	0.183	−0.187	0.356	3.80	−1.90	7.21
C_2	0.231	−0.357	0.370	4.80	−2.08	7.50	3.3	0.230	−0.359	0.369	4.80	−2.09	7.49
C_3	0.222	−0.521	0.318	4.83	−3.03	6.44	2.7	0.233	−0.521	0.319	4.86	−3.03	6.47
C_4	0.187	−0.517	0.257	3.89	−3.01	5.20	2.5	0.187	−0.516	0.258	3.89	−3.00	5.22
C_5	0.144	−0.330	0.243	2.99	−1.92	4.93	2.5	0.144	−0.328	0.243	2.99	−1.91	4.93
C_6	0.139	−0.176	0.294	2.89	−1.02	5.95	2.8	0.138	−0.168	0.294	2.88	−0.98	5.95
Center of gravity of I ring											3.87	−3.80	6.21
H_2								0.265	−0.368	0.419	5.52	−2.14	8.48
H_3								0.270	−0.655	0.329	5.62	−3.81	6.67
H_4								0.188	−0.646	0.220	3.91	−3.76	4.46
H_5								0.111	−0.314	0.195	2.31	−1.83	3.94
H_6								0.102	−0.031	0.284	2.12	−0.18	5.75
C'_1	0.077	0.058	0.420	1.61	0.34	8.50	2.1	0.079	0.067	0.421	1.64	0.39	8.54
C'_2	0.039	0.238	0.386	0.82	1.39	7.81	1.3	0.037	0.242	0.389	0.78	1.41	7.88
C'_3	−0.029	0.214	0.370	−0.61	1.25	7.49	2.1	−0.030	0.207	0.369	−0.64	1.20	7.48
C'_4	−0.058	−0.003	0.388	−1.20	−0.02	7.87	2.3	−0.058	−0.003	0.387	−1.20	−0.02	7.84
C'_5	−0.018	−0.174	0.420	−0.37	−1.01	8.50	2.1	−0.016	−0.178	0.419	−0.34	−1.04	8.49
C'_6	0.050	−0.151	0.437	1.04	−0.88	8.86	2.8	0.052	−0.143	0.436	1.08	−0.83	8.84
Center of gravity of I' ring											0.22	0.19	8.18
H'_2								0.058	0.407	0.378	1.21	2.37	7.65
H'_3								−0.063	0.342	0.343	−1.31	1.99	6.94
H'_4								−0.111	−0.031	0.374	−2.30	−0.18	7.58
H'_5								−0.037	−0.340	0.431	−0.77	−1.98	8.74
H'_6								0.084	−0.278	0.462	1.75	−1.62	9.35
I	0.1802	0.0430	0.4344	3.75	0.25	8.80	55						
Cl	0.3316	0.0636	0.4585	6.90	0.37	9.29	13.3						

is achieved by analyzing the experimental coordinates as described below.

1. First of all, the method of least squares was used to find the equations of the "best" planes for the two benzene rings

$$\sum_{i=1}^{6} (Ax + By + Cz + D)^2 \to \min,$$

whence

$$A\sum_{i=1}^{6} x_i^2 + B\sum_{i=1}^{6} x_i y_i + C\sum_{i=1}^{6} x_i z_i + D\sum_{i=1}^{6} x_i = 0,$$

$$A\sum_{i=1}^{6} x_i y_i + B\sum_{i=1}^{6} y_i^2 + C\sum_{i=1}^{6} y_i z_i + D\sum_{i=1}^{6} y_i = 0,$$

$$A\sum_{i=1}^{6} x_i z_i + B\sum_{i=1}^{6} y_i z_i + C\sum_{i=1}^{6} z_i^2 + D\sum_{i=1}^{6} z_i = 0,$$

$$A\sum_{i=1}^{6} x_i + B\sum_{i=1}^{6} y_i + C\sum_{i=1}^{6} z_i + \sum_{i=1}^{6} D = 0,$$

where $x_i y_i z_i$ are the experimental coordinates of the carbon atoms.

Setting D equal to an arbitrary constant, say D=1, we obtain four equations with three unknowns A, B, and C. On determining these we find the equations for the "best" planes for the I and I' rings. In the orthogonal coordinate system a^*bc:

$$1.0.645x + 0.584y - 0.493z - 1.994 = 0,$$
$$1'.0.087x - 0.359y - 0.929z - 7.614 = 0.$$

The deviations of the carbon atoms from the corresponding planes do not exceed 0.04 Å; this quantity characterizes the accuracy of determining the carbon-atom coordinates.

2. The benzene rings were subjected to an affine transformation into the coordinate plane x'0z'. The transformation requires transfer of the origin of the coordinate system to the center of one of the atoms (in our case, C_1 and C'_1), after which the formulas for transforming from the "old" system of coordinates to the "new," and conversely, take the form

$$\left.\begin{aligned} 1)\ x' &= a_{11}x + a_{21}y + a_{31}z \\ 2)\ y' &= a_{12}x + a_{22}y + a_{32}z \\ 3)\ z' &= a_{13}x + a_{23}y + a_{33}z \end{aligned}\right\} \text{(a)}$$

$$\left.\begin{aligned} x &= a_{11}x' + a_{12}y' + a_{13}z' \\ y &= a_{21}x' + a_{22}y' + a_{23}z' \\ z &= a_{31}x' + a_{32}y' + a_{33}z' \end{aligned}\right\} \text{(b)}$$

Here, x', y', z' are the coordinates in the new system and x, y, z those in the old.

Let us denote $h_i - h_1 = y'$, where h_1 and h_i are the distances of the first and i-th atoms from the "best" plane, and let us write equations (a) for atoms C_3, C_4, and C_5 (the most distant from C_1):

$$y'_3 = a_{12}x_3 + a_{22}y_3 + a_{32}z_3,$$
$$y'_4 = a_{12}x_4 + a_{22}y_4 + a_{32}z_4,$$
$$y'_5 = a_{12}x_5 + a_{22}y_5 + a_{32}z_5.$$

Hence, we find a_{12}, a_{22}, and a_{32}.

Equations (b) 1, 2, 3 for atom C_4 ($x'_4 = 0$, $y'_4, z'_4 = z_0$, where $z_0 = \sqrt{[d_{14} - (h_4 - h_1)^2]}$, and d_{14} is the distance between atoms C_1 and C_4) will be

$$x_4 = a_{13}y'_4 + a_{13}z_0,$$
$$y_4 = a_{23}y'_4 + a_{23}z_0,$$
$$z_4 = a_{33}y'_4 + a_{33}z_0.$$

These give coefficients a_{13}, a_{23}, and a_{33}.

The coefficient a_{11} is determined from expression $a_{11} = \pm\sqrt{(1 - a_{12}^2 - a_{13}^2)}$, the sign being selected arbitrarily. Coefficients a_{21} and a_{31} are found from the relations

$$a_{11}a_{21} + a_{12}a_{22} + a_{13}a_{23} = 0,$$
$$a_{11}a_{31} + a_{12}a_{32} + a_{13}a_{33} = 0.$$

3. The next stage was to find the coordinates of the carbon atoms in the ideal benzene ring, this being so arranged in the plane as to minimize the mean-square deviation of its atoms from the experimental positions. For this purpose the center of a regular hexagon of side 1.40 Å was made to coincide with the center of gravity of the experimental benzene ring, after which the origin of coordinates was moved to the center of gravity of the latter in such a way that the 0Z" axis should coincide with the diagonal $C_1 - C_4$.

In the new system of coordinates, x"y"z", the regular hexagon was rotated around the 0Y" axis so as to make the deviations of its carbon atoms from the experimental positions in this system a minimum. This kind of rotation, as we know, corresponds to the formula

$$x'_{exp} = x_{id}\cos\varphi + z_{id}\sin\varphi,$$
$$z'_{exp} = -x_{id}\sin\varphi + z_{id}\cos\varphi,$$

where x''_{exp}, z''_{exp} are the experimental coordinates and x_{id}, z_{id} the ideal coordinates of the vertices of the regular hexagon.

The required rotation may be found by minimizing the square error in the form

$$\left.\begin{matrix}\sum(x'_{exp} - x_{id}\cos\varphi - z_{id}\sin\varphi)^2 \\ \sum(z'_{exp} - x_{id}\sin\varphi - z_{id}\cos\varphi)^2\end{matrix}\right\} \to \min$$

Having found the position of the regular hexagon corresponding as closely as possible to experiment, we must now retransform to the original coordinate system. This will give the coordinates of the vertices of a regular hexagon, i.e., the ideal positions of the carbon atoms in the original system.

The fully solved structures will be compared with the structures of other compounds of tervalent iodine in a following article.

The present paper is the first of a series on the structure of onium compounds originating in the X-Ray Analysis Laboratory of the Institute of Heteroorganic Compounds, Academy of Sciences of the USSR. In addition to diphenyliodonium borofluoride, $[(C_6H_5)_2I]^+[BF_4]^-$ (which has an ionic structure), the structures of certain bromonium and chloronium compounds were studied.

We consider it our duty to thank Yu. T. Struchkov for direct participation in the work and to acknowledge the constant interest and attention of A.I. Kitaigorodskii, the Director of the Laboratory.

LITERATURE CITED

1. L.G. Makarova and A.N. Nesmeyanov, "Decomposition and formation of onium compounds and synthesis of heteroorganic compounds by way of onium compounds," Izv. Akad. Nauk SSSR, OKhN, No. 6, 617 (1945).
2. H.J. Lucas, E.R. Kennedy, and C.A. Wilmot, "The decomposition of diorthotholyliodonium iodide," J. Am. Chem. Soc., 58, 157 (1936).
3. W.V. Medlin, "The I–I bond in diphenyliodonium iodide," J. Am. Chem. Soc., 57, 1026 (1935).
4. A.I. Kitaigorodskii, T.L. Khotsyanova, and Yu.T. Struchkov, "Some questions on the methods of x-ray structural analysis used in a study of the crystal structure of tetraiodethylene," Zh. Fiz. Khim., 27, 10, 1490 (1953).

SOVIET PHYSICS - CRYSTALLOGRAPHY VOL. 1, NO. 5 SEPT.-OCT., 1956

X-RAY DIFFRACTION STUDY OF THE CRYSTAL-LATTICE CONSTANTS AND THERMAL-EXPANSION COEFFICIENTS OF LEUCOSAPPHIRE AND RUBY

N. A. Shal'nikova and I. A. Yakovlev

M. V. Lomonosov State University, Moscow

Translated from Kristallografiya, Vol. 1, No. 5, pp. 531-533, September-October, 1956
Original article submitted July 4, 1956

The lattice parameters of leucosapphire were determined by x-ray diffraction in the temperature range of 20-1000°C; the lattice parameters of ruby were determined as a function of Cr_2O_3 content.

The important technical applications of pure α-Al_2O_3 crystals, and especially ruby (i.e., corundum with chromium impurities) give rise to continued interest in their physical properties.

Despite various approaches made toward the study of corundum crystals, no precise values of their lattice parameters as a function of temperature and impurity content have yet been obtained [1-4]. A recent paper by Tillo [5], moreover, contains the doubtful assertion that the introduction of chromium into α-Al_2O_3 only begins to affect the lattice parameters of corundum after the chromium content reaches a critical value of 8 at.%.

We undertook the work of determining the most important lattice constants of pure α-Al_2O_3 as exactly as possible, studying their variation with chromium content, and finding the thermal-expansion coefficients of pure corundum and ruby. The single-crystal ruby samples used (kindly provided for our measurements by S. V. Grum-Grzhimailo) were described in [6] together with data on their chemical analysis. Polycrystalline samples are described in [1, 2] and their chemical analysis is given in [7].

The lattice constants of corundum were calculated from photographs obtained in the RKU-114 camera. Because of some uncertainty in indexing the diffraction lines, some control measurements were made, using oscillation photographs of a single crystal in the RKV-86 camera with an attachment for taking epigrams. This made it easy to index the RKU-114 photographs. The constant a was calculated from the 330 doublet and c from the 21.14 doublet. The results in kX are given in Table 1 together with those of other authors. The constants (a and c) for ruby were obtained in a similar way and appear in Table 2. The data of Tillo, which have a special part to play, are compared with our data in Fig. 1.

The monotonic form of our graph suggests that Tillo's results [5] for small chromium content are wrong. The curious shape of Tillo's curve is probably due to the low sensitivity of his apparatus.

The thermal-expansion coefficients of pure corundum and rubies were measured in a "Unicam" camera over the temperature range 20-1000°C. The stability of the temperature over the sample was 0.4 deg/mm for a sample length of 15 mm. This enabled the lattice constants to be measured with an accuracy of 0.001 kX. The results of the measurements are given in Table 3.

The linear-expansion coefficients $\beta_\perp$ and $\beta_\parallel$ were calculated from the data of Table 3 by using empirical formulas for the experimental relationships a (t) and c(t).

The formulas have the form

$$a(t) = 4.7474 + 2.8 \cdot 10^{-5}\, t + 9.7 \cdot 10^{-9}\, t^2, \quad (1)$$

$$c(t) = 12.9554 + 8.0 \cdot 10^{-5}\, t + 2.3 \cdot 10^{-8}\, t^2. \quad (2)$$

TABLE 1*

No.	Year	Authors	a, kX	c, kX	
1	1920	Davey and Hofman	4.86	13.23	
2	1922	Bragg	4.75	12.974	
3	1927	Harrington	4.761	12.941	
4	1928	Zachariasen	4.76	13.00	
5	1930	Passerini	4.741	12.958	
6	1953	Swanson and Fuyat	4.749	12.965	at 26° C
7	1956	Present work	4.748	12.957	at 20° C

*Data 1-6 in this table are taken from [4].

TABLE 2

% Cr_2O_3	a, kX	c, kX
0	4.7477±4	12.957±1
1.5 [*]	4.7490±4	12.962±1
2.9 »	4.7521±5	12.967±1
9.6 [1,2]	4.7643±5	12.994±2
23.2 »	4.7914±6	13.071±2
48.7 »	4.8365±6	13.198±2

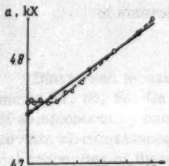

Fig. 1. Lattice spacing a as a function of Cr_2O_3, wt.%; points ○ represent Tillo's data [5]; ● represent our own.

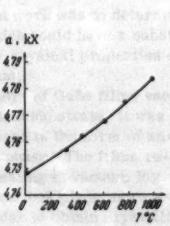

Fig. 2. Lattice spacing a as a function of temperature. The curve follows formula (1); the points give our experimental data.

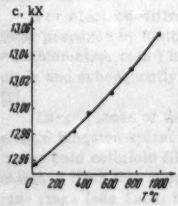

Fig. 3. Lattice spacing c as a function of temperature. The curve follows formula (2); the points give our experimental data.

TABLE 3

T°C	a, kX	c, kX
	α-Al_2O_3	
20	4.748±1	12.957±3
320	4.757±1	12.982±3
440	4.762±1	12.995±3
610	4.763±1	13.011±4
770	4.775±1	13.038±4
980	4.784±1	13.056±4
	α-Al_2O_3 + 9.6% Cr_2O_3 [1,2]	
20	4.765±1	12.994±3
570	4.784±1	13.062±4

TABLE 4

Coefficients	α-Al_2O_3	α-Al_2O_3 + 9.6% Cr_2O_3
$\beta_\perp$ (500° C)	$7.1 \cdot 10^{-6}$	$7.2 \cdot 10^{-6}$
$\beta_\parallel$ (500° C)	$7.0 \cdot 10^{-6}$	$8.2 \cdot 10^{-6}$

The agreement between the formulas and the experimental results is indicated in Figs. 2 and 3. By using the formulas we obtain the following linear-expansion coefficients:

$$\beta_\perp = 5.85 \cdot 10^{-6} + 2.05 \cdot 10^{-9}\, t,$$

$$\beta_\parallel = 6\,23 \cdot 10^{-6} + 1.8 \cdot 10^{-9}\, t.$$

Measurements of a (t) and c(t) for ruby containing 9.6% chromium showed that the linear-expansion coefficients were larger than those of pure corundum. Table 4 compares the average values of $\beta_\perp$ and $\beta_\parallel$ for the temperature range 20 to 600°C for corundum and ruby.

Comparison of the linear-expansion coefficients found for pure corundum with the results of other authors [8-11] shows that our values agree closely with dilatometric measurements [8-10] but disagree violently with Sharma [11].

We should remember that the linear-expansion coefficient $\beta_\parallel$ depends much more strongly on the presence of chromium in α-Al_2O_3 than does $\beta_\perp$. Hence, we may conclude that the isomorphic introduction of Cr in place of Al in the corundum lattice primarily tends to weaken the ionic bonds in the crystal in the c direction.

The authors are extremely grateful to S. V. Grum-Grzhimailo for drawing their attention to the problems considered in this paper and for useful comments in discussing the results.

LITERATURE CITED

1. S. V. Grum-Grzhimailo, "Properties of isomorphic mixtures of Al_2O_3–Cr_2O_3," Tr. Inst. Kristallogr., 8, 27-34 (1953).
2. S. V. Grum-Grzhimailo and A. N. Lyamina, "Optical control of ceramic dyes," Zh. Prikl. Khim., 21, 12, 1228-1240 (1948).
3. E. S. Rudnitskaya, "Basic information on the crystallography and structure of corundum crystals," Tr. Inst. Kristallogr., 8, 13-20 (1953).
4. H. E. Swanson and R. K. Fuyat, "Standard x-ray diffraction powder patterns," Natl. Bur. Stds. Circular, 539, II, 20-23 (1953).
5. E. Tillo, Über die Farbe des Rubins. Miscellanea academica berolinensia. Gesammelte Abhandlungen zur Feier des 250 jährigen Bestehens der Deutschen Akademie der Wissenschaften zu Berlin, 1, 89-94 (1950).
6. S. V. Grum-Grzhimailo and E. I. Utkina, "Possibility of determining the quantity of chromium in ruby by an optical method," Tr. Inst. Kristallogr., 8, 99-100 (1953).
7. E. I. Pashkovskaya, "Chromium content in rubies," Tr. Inst. Kristallogr., 8, 43-46 (1953).
8. R. A. Heindl, "The thermal expansion of refractories to 1800°C," Bur. Stds. J. Res., 10, 715-735 (1953).
9. W. Büssen, M. Bluth, and C. Grochtmann, Röntgenographische ausdehnungsmessungen kristalliner Massen I. Berichte der Deutschen Keramischen Gesellschaft, 16, 381-387 (1935).
10. H. Ebert and C. Tingwaldt, Ausdehnungsmessungen bei Temperaturen bis 2000°C. Phys. Z., 37, 13, 471-475 (1936).
11. S. S. Sharma, "Thermal expansion of crystals," Proc. Ind. Acad. Sci., 33, 245-248 (1951).

SOVIET PHYSICS - CRYSTALLOGRAPHY VOL. 1, NO. 5 SEPT.-OCT., 1956

ELECTRON-DIFFRACTION STUDY OF AMORPHOUS GaSe

L. I. Tatarinova

Institute of Crystallography, Academy of Sciences of the USSR

Translated from Kristallografiya, Vol. 1, No. 5,
pp. 534-536, September-October, 1956
Original article submitted June 26, 1956

Amorphous films of GaSe prepared by vacuum deposition on celluloid substrates were studied. An experimental curve of intensities normalized by the atomic-factor curve was obtained. In view of the similarity between the atomic numbers, it was assumed that the substance consisted of atoms of one type. The radial distribution curve was calculated. Interatomic distances $r_1 = 2.40$ and $r_2 = 3.75$ Å were found; the numbers of nearest atoms were 6 and 12. These data show that in the first coordination groups of amorphous GaSe there is no correspondence with the lattice of the crystal phase.

Binary and ternary systems containing the elements Tl, Sb, Se, Ga, As, Bi, etc., form a series of semiconducting compounds, some of which, under certain circumstances, are amorphous. The physical properties of these (conductivity, activation energy, thermal emf, etc.) are characteristic of crystalline substances [1].

The aim of the present work was to determine the short-range order, which could have a substantial bearing on some of the physical properties of GaSe in the amorphous state.

By studying the structure of GaSe films vacuum-deposited onto a celluloid substrate, it was found that the GaSe condensed in the form of an extremely stable amorphous phase. The films remained amorphous after heating in vacuum for many hours. Crystallization took place more easily in the thicker films. In order to obtain crystalline samples it was essential to preheat the celluloid film to 120-130°C.

For electron-diffraction examination we used GaSe prepared by fusing the elements (taken in stoichiometric ratio) in an evacuated quartz ampoule and subsequently cooling to room temperature [1].

Large pieces of this alloy were placed in a cone-shaped tungsten spiral and vacuum-evaporated onto hot or cold celluloid films. The diffraction picture obtained from this specimen consisted of four diffuse rings (see Table 1).

In order to obtain an experimental intensity curve the multiple-exposure method was used for the diffraction pictures [2].

Six electron-diffraction photographs were obtained with multiple exposures and microphotometric curves were obtained on the MF-4 photometer. After constructing blackening curves and determining intensities for various values of $(\sin\vartheta)/\lambda$ from these, we obtained an experimental intensity curve for amorphous GaSe in arbitrary units.

The application of the integral-analysis method in electron diffraction to complex substances including atoms of various kinds demands special theoretical treatment. The case of GaSe may, however, be simplified. Remembering the proximity of the respective atomic numbers (Ga, 31; Se, 34) and scattering powers, we may regard this compound as consisting of atoms of one sort.

The experimental intensity curve must be normalized by a curve representing the sum of coherent and incoherent scattering

TABLE 1

Ring No.	$(\sin\vartheta)/\lambda$	Intensity
1	0.110	Weak
2	0.166	Very very strong
3	0.276	Weak
4	0.430	Very strong

$$\frac{f^2_{Ga}+f^2_{Se}}{2}+\frac{(ZS/s^4)_{Ga}+(ZS/s^4)_{Se}}{2}, \qquad (1)$$

where $f_{Ga,Se}$ is the atomic scattering factor of electrons for Ga and Se; Z is the atomic number; ZS is is the incoherent-scattering function; $s = (4\sin\vartheta)/\lambda$; 2ϑ is the scattering angle; λ is the electron wavelength.

In expression (1), the first term represents coherent scattering and the second (calculated from data of Bewilogua [3]) incoherent scattering. The curves were joined at $(\sin\vartheta)/\lambda \simeq 0.8$. After normalization and subtraction of the incoherent scattering from the intensity curve (Fig. 1), the quantities under the integral sign in the expression

$$4\pi r^2\rho(r) = 4\pi r^2\rho_0 + \frac{2r}{\pi}\int_0^\infty si(s)\sin srds$$

could be determined.

Here, r is the distance in Å, $\rho(r)$ is the atomic-density function, and ρ_0 is the mean atomic density of the given substance

$$\rho_0 = \frac{5.03\ \text{g/cm}^3}{148.68\cdot 1.65\cdot 10^{-24}} = 0.0205\ \text{at./Å}^3.$$

For calculating the integral we used the simplified method proposed by Harris, Wood, and Ritter [4]. The integration reduces to the summation of a large number of terms. The whole of the region s used is divided into small intervals, e.g., $\Delta s = 0.02$. The integrand comprises the product of two factors si(s) and sin sr; the si(s) is a curve in a range varying, for example, from 0 to 10.05, which determines the practical limits of integration. If we choose r so that for any small value of s the product $rs = 2\pi$, then sin sr, sin 2sr, sin 3sr, ... will be zero and at intermediate points the sines will have recurring positive and negative values. For example, if $r = 5.0671$, then for $s = 0$, 1.24, 2.48, ..., 9.92, the product rs is a multiple of 2π. The whole range of s considered will have 8 cycles. However, we have only to calculate 15 sine values in a $\frac{1}{4}$ period. The multiplication by si(s) reduces to addition of coefficients for the same values of the sines.

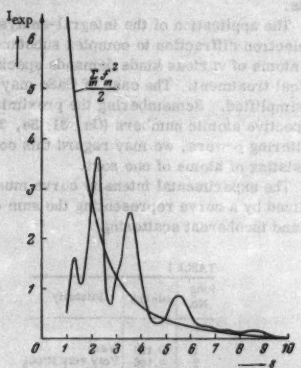

Fig. 1

It is still simpler to prepare strips representing the product of sines by si(s) where si(s) varies, for example, from 1 to 100 in certain small intervals.

Having calculated the integral in this way, we obtained a radial distribution curve (Fig. 2). The first two maxima lie at $r_1 = 2.40$ and $r_2 = 3.75$ Å. The area under these corresponds to approximately 6 and 12 atoms. In order to interpret these results we turn naturally to the lattice of crystalline GaSe, the structure of which we studied earlier together with that of the amorphous type [5]. The GaSe lattice has distances Se–Se = 2.33 and Ga–Se = 2.48 Å, averaging 2.405 Å. We may suppose that both these distances are reflected in the first maximum. In the GaSe lattice, however, each Ga or Se atom has three Se or Ga atoms around it at distances of 2.48 Å. The interatomic distance 3.75 Å is the lattice spacing a. In the plane of the film there are six atoms of the same type at this distance from any one atom. Furthermore, there are three Ga atoms around each Ga at a distance of 3.84 Å. We may suppose that the second maximum reflects both these distances. Thus, according to our data, there is no correspondence between the first coordination groups of the amorphous phase and the crystalline-phase lattice. Perhaps we should not have expected such correspondence, since it may well be that a

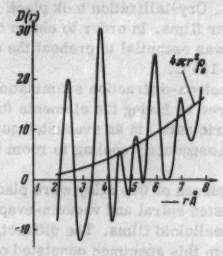

Fig. 2

change of coordination takes place on passing from the amorphous to the crystalline state without any change in the composition.

LITERATURE CITED

1. B. T. Kolomiets and N. A. Goryunova, "Properties and structure of ternary semiconductor systems. 1. Electrical properties and structure of certain substances in the Tl–Sb–Se system," Zh. Tekhn. Fiz., 25, 984-994 (1955).
2. L. I. Tatarinova, "Electron-diffraction study of amorphous antimony," Tr. Inst. Kristallogr., 11, 104-114 (1955).
3. L. Bewilogua, "Über inkoherente Streckung der Röntgenstrahlen," Phys. Zschr., 32, 740-744 (1931).
4. R. L. Harris, R. E. Wood, and H. L. Ritter, "The structure of liquid aluminum chloride," J. Am. Chem. Soc., 73, 3151-3155 (1951).
5. L. I. Tatarinova, Yu. K. Auleitner, and Z. G. Pinsker, "Electron-diffraction study of the structure of GaSe," Kristallografiya, 1, 5, 537-542 (1956).

ELECTRON-DIFFRACTION STUDY OF GaSe

L. I. Tatarinova, Yu. K. Auleitner,* and Z. G. Pinsker

Institute of Crystallography, Academy of Sciences of the USSR

Translated from Kristallografiya, Vol. 1, No. 5, pp. 537-541, September-October, 1956
Original article submitted June 7, 1956

GaSe films obtained by vacuum evaporation onto celluloid substrates and subsequently annealed were subjected to structural study. The hexagonal unit cell had $a = 3.74$, $c = 15.89$ kX. The space group was $D_{3h}^4 - C6mmc$; the atoms lay in position 4(f), $z_{Ga} = -0.10$; $z_{Se} = 0.177$. The structure was layerlike. The layers were composed of pyramids turned with the (Se) vertices toward one another, the bases being Ga atoms. The absence of many reflections from the electron-diffraction patterns and the diffuseness of others indicated defects in the lattice structure caused by the displacement of layers perpendicularly to the c axis by a vector distance $\frac{1}{3}x + \frac{2}{3}y$.

The crystal structure of phases belonging to the Ga–Se system has been studied several times by x rays [1]. Apparently there are one or two phases corresponding to the ideal composition GaSe in the concentration range 48 to 52 at.% Se. According to x-ray data [1], a rhombohedral structure predominates for Se > 50 at.% and a hexagonal structure for Se < 50 at.%. Samples were prepared by fusing the elements in vacuum; the processes of ordering and crystallizing take place very slowly (even at high temperatures) and some of the maxima on the x-ray diffraction pictures are diffuse. The two structures are very similar, and in powder photographs the occurrence of the rhombohedral phase is indicated by splitting of the $(01\bar{1}3)$ line of the hexagonal lattice.

The hexagonal-lattice spacings are $a = 3.73_5$ and $c = 15.88_7$ kX. There are four GaSe molecules in the unit cell. In describing the structure, the authors of [1] presented the concept of lattice defects consisting of sections with rhombohedral stacking forming part of the hexagonal phase. The space group $C_{3h}^1 - C\bar{6}$ was selected; this enabled the coordinates of two molecules to be described by setting them in positions 2(g) and 2(i), the other two molecules requiring translations $\frac{2}{3}, \frac{1}{3}, \frac{1}{2}$. From the data presented we find that a considerable number of reflections which would have been expected to occur are in fact absent from the x-ray diffraction photographs.

We notice the similarity between the unit-cell dimensions given for the hexagonal phase and those of GaS [2]: $a = 3.57_8$ and $c = 15.4_7$ kX. The GaS structure is described by the group D_{3h}^1; the atoms of Ga and S occupy position 4(f) with parameters $z_{Ga} = 0.17$ and $z_S = 0.60$. From the data on GaSe we see [2] that the x-ray diffraction photographs of the hexagonal phase show no reflections contradicting the extinction conditions for D_{3h}^1. Hence, we may expect the structures of GaS and GaSe to be very similar.

In the present investigation we used samples of GaSe[1] prepared by fusion in a quartz ampoule under vacuum, taking the elements in stoichiometric ratio [3]. The specimens for electron-diffraction study were obtained by evaporating the GaSe onto a celluloid substrate. The first experiments led to the formation of an amorphous deposit. In order to obtain a crystalline film, the celluloid substrate was preheated to about 120°C. Crystallization took place more rapidly (3–4 h, subsequent to heating for thicker films. Thin films remained amorphous even after 10 h. Specimens for study in transmission

*Institute of Physics, Polish Academy of Sciences, Warsaw.

[1]The compound was obtained from B.T. Kolomiets and N. A. Goryunova, Leningrad Physicotechnical Institute.

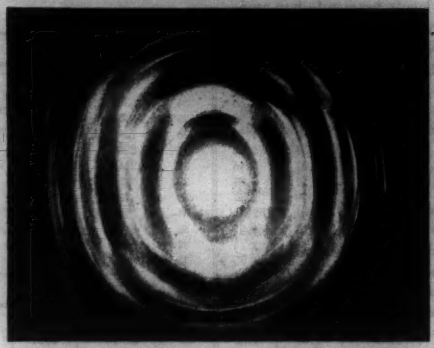

Fig. 1. Electron-diffraction photograph of GaSe.

were also prepared from a suspension in water. The orientation in these was worse; hence, for obtaining oblique-texture diffraction patterns, films prepared by sublimation were used. From these diffraction patterns (Fig. 1) we see that the processes of ordering and crystallization failed to pass to completion, since two types of reflection occur: sharp and diffuse. The complete set of reflections corresponds to spacings of $a = 3.74$ and $c = 15.889$ kX of the hexagonal unit cell, in agreement with the x-ray data. Diffuse reflections only occur on ellipses with $h - k \neq 3n$, the reflections of hki0 type on these having normal sharpness.

In the first stages we made an attempt to calculate the structure from the sharp reflections only, these corresponding to spacings $a = 3.74$ and $c = 7.945$ kX. The results obtained from the complete set of reflections show that, by analyzing the data with the sharp reflections only, we obtain the structure of a single "packet" of the type making up the GaSe lattice (see below).

The electron-diffraction pictures show the following extinctions: hki$l$ exist in all orders, 000l only for $l = 2n$, hh2$\bar{h}l$ only for $l = 2n$; of the hki$l$ with $h - k = 3n$, only those for which $l = 2n$ exist. The number of extinctions exceeds that which might be expected for any of the hexagonal space groups. Some of these extinctions may be connected with special positions of the atoms and perhaps other features of lattice structure; they are not contradictory to a number of groups, including space group D_{6h}^4. By analogy with GaS, we may site the Ga and Se atoms in the 4(f) position:

$$1/3,\ 2/3\ z,\ 2/3\ 1/3\ z,\ 2/3,\ 1/3\ 1/3+z,\ 1/3\ 2/3\ 1/3-z.$$

We were able to locate 54 independent reflections on the photographs (including 7 0001).

The intensities of the sharp reflections were estimated visually and those of the diffuse reflections on an objective nonrecording MF-2 microphotometer. The intensities of the diffuse and sharp reflections were compared by measuring the half-widths of the maxima and equating these to the half-widths of the sharp reflections by introducing an appropriate factor.

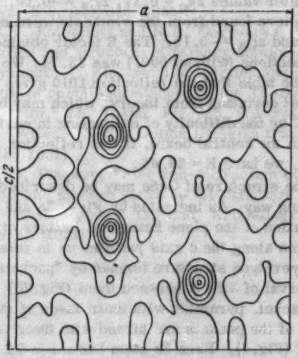

Fig. 2. Cross section of Φ series (potential) of the GaSe structure along the x0z plane.

TABLE 1

Serial No.	hkil	Φ exp	Φ theor	Serial No.	hkil	Φ exp	Φ theor
1	$10\bar{1}0$	2.32	4.83	24	$30\bar{3}.12$	0.86	0.83
2	$10\bar{1}3$	4.86	3.95	25	$30\bar{3}.14$	1.16	1.40
3	$10\bar{1}5$	1.36	1.75	26	$22\bar{4}0$	2.68	2.02
4	$10\bar{1}7$	4.01	4.33	27	$22\bar{4}4$	1.83	0.99
5	$11\bar{2}0$	5.07	5.16	28	$22\bar{4}8$	1.20	0.53
6	$11\bar{2}2$	0.57	0.84	29	$22\bar{4}.10$	0.87	0.92
7	$11\bar{2}4$	3.56	2.37	30	$22\bar{4}.12$	0.97	0.73
8	$11\bar{2}8$	0.51	1.11	31	$22\bar{4}.14$	0.99	1.23
9	$11\bar{2}.10$	1.66	1.71	32	$31\bar{4}0$	1.36	0.95
10	$11\bar{2}.12$	1.76	1.24	33	$31\bar{4}3$	0.84	0.91
11	$11\bar{2}.14$	1.86	1.95	34	$31\bar{4}5$	0.46	0.50
12	2020	1.95	2.21	35	$31\bar{4}7$	1.37	1.45
13	$20\bar{2}3$	2.13	2.04	36	$40\bar{4}0$	1.13	0.80
14	$20\bar{2}5$	0.89	1.08	37	$40\bar{4}7$	1.35	1.24
15	$20\bar{2}7$	2.30	2.86	38	$32\bar{5}0$	1.00	0.70
16	$21\bar{3}0$	1.76	1.55	39	$32\bar{5}7$	1.64	1.09
17	$21\bar{3}3$	1.66	1.45	40	$41\bar{5}0$	1.23	1.31
18	$21\bar{3}5$	0.51	0.78	41	$41\bar{5}4$	1.07	0.65
19	$21\bar{3}7$	1.51	2.14	42	$41\bar{5}.10$	0.85	0.65
20	$21\bar{3}.11$	0.57	0.76	43	$41\bar{5}.12$	1.13	1.96
21	$30\bar{3}0$	2.93	2.55	44	$41\bar{5}.14$	1.16	0.94
22	$30\bar{3}4$	2.36	1.23	45	$50\bar{5}0$	1.09	0.57
23	$30\bar{3}.10$	0.83	1.08	46	$33\bar{6}0$	1.14	1.07
				47	$42\bar{8}0$	1.23	0.52

From experimental values of Φ^2 we calculated the cross section of the Φ^2 series in the (00z) direction. The resultant interatomic vectors enabled us to site the atoms in the unit cell and make a preliminary estimate of the parameters. These were refined by calculating the series for the potential cross section in the x0z plane (Fig. 2). In order to determine the signs of the structure amplitudes we used parameter values $z_{Se} = 0.17$, $z_{Ga} = -0.10$. The parameters found from the synthesis were $z_{Se} = 0.177$ and $z_{Ga} = -0.10$. The R factor obtained from 47 reflections (without 000l) was 25.7%. We see from the table that the reflection $10\bar{1}0$ gives the greatest deviation from theory, which may be explained by the difficulty of estimating intensities so close to the central beam. If this reflection is excluded, we have R = 23.0%.

The structure of GaSe may be described in the following way. As indicated by Figs. 3a and 4, the alternation of the plane hexagonal lattices of Ga and Se atoms along the c axis justifies us in referring to a layer-type structure formed by "packets" with an interval of 3.18 Å between them (Fig. 3b). Inside each packet, pyramids with their bases at the boundaries of the packets are turned with their vertices inward (Fig. 4). Each Se atom has three Ga atoms at 2.48 Å and one Se at 2.325 Å as its nearest neighbors. The very similar scattering powers of the two kinds of atoms prevent us from choosing between the form shown in Fig. 4 and another in which Ga and Se are interchanged from experimental data only. The arrangement shown in Figs. 3a, b is preferable, since the distance between atoms a and a' is close to the minimum Se–Se distance in the Se lattice (2.32 Å) and differs from the corresponding Ga–Ga distance in the Ga lattice (2.45 Å). We consider that the difference between the chemical functions of Ga and Se excludes the possibility of these

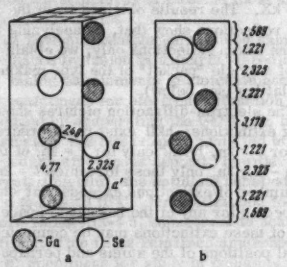

Fig. 3. Scheme of GaSe structure: (a) spatial arrangement of atoms; (b) section of the structure in a $(11\bar{2}0)$ plane.

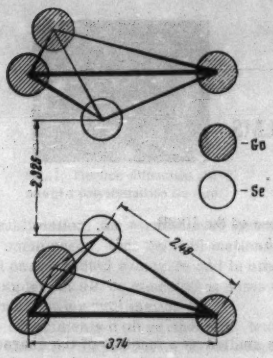

Fig. 4. Coordination of atoms in the GaSe structure.

atoms having a disordered arrangement in the lattice.

We failed to observe the rhombohedral structure found in the x-ray work, although all the hexagonal-phase reflections for which $h - k = 3n$ satisfied the rhombohedral condition $h - k + l = 3n$. Reflections with $h - k \neq 3n$, however, did not satisfy this condition.

The structure described may be regarded as ideal. The model was obtained without allowing for the absence of a large number of reflections for which the calculated intensity was nonzero, and also without allowing for the diffuse nature of a certain group of reflections.

As mentioned earlier, all reflections with $l = 2n$ are absent from ellipses with $h - k \neq 3n$, and all present are diffuse. A possible explanation for these peculiarities is based on a theory relating to disorder in the structure of hexagonal cobalt [4]. In hexagonal cobalt the structural distortion is connected with the displacement of some layers by a vector length $\frac{1}{3}x + \frac{2}{3}y$. As a result of this displacement, reflections with $h - k = 3n$ and $l \neq 2n$ drop out, while for $l = 2n$ they have normal intensity and sharpness. Reflections with $h - k \neq 3n$ become diffuse and elongated along the c^* direction; the diffuseness of reflections with $l = 2n$ is three times greater than that of reflections with $l \neq 2n$, which explains the absence of the former from the electron-diffraction patterns. All hki0 reflections remain sharp. These features of the electron-diffraction picture correctly reflect those found for the case of GaSe.

The shift of $\frac{1}{3}x + \frac{2}{3}y$ in the structure of GaSe is entirely possible in view of its layerlike arrangement. Thus, the structure of our GaSe specimens cannot be characterized by any particular space group in view of the absence of strict periodicity along the c axis, i.e., periodicity in the positioning of the layers. At the same time, the projection of the assembly of superposed layers may be characterized by a plane translational group $C_3 - p3$.

It is interesting to compare the disorder of the GaSe structure here described with that found in layered lattices of CdI_2, $CdBr_2$, etc. [5]. In contrast to the variable structure in CdI_2 and others, GaSe does not apparently contain inclusions with a definite spatial periodicity along the three directions. Packets of structure displaced from their "regular" position by $\frac{1}{3}x + \frac{2}{3}y$ are distributed at random over the thickness of the crystal (along the x axis).

LITERATURE CITED

1. K. Schubert, E. Dörre, and M. Kluge, "Zur Kristallchemie der B-Metalle. III. Kristallstruktur von GaSe und InTe," Z. Metall., 46, 216-224 (1955).
2. H. Hahn and G. Frank, "Über die Kristallstruktur des GaS," Z. Anorg. Allgem. Chem., 278, 5-6, 340-348 (1955).
3. B. T. Kolomiets and N. A. Goryunova, "Properties and structure of ternary semiconductor systems. 1. Electrical properties and structure of certain substances in the Tl–Sb–Se system," Zh. Tekhn. Fiz., 25, 984-994 (1955).
4. A. Wilson, X-Ray Optics [Russian translation] (IL, 1951).
5. Z. G. Pinsker, "Electron-diffraction study of BiI_2 and modern views on the structure of layered lattices," Tr. Inst. Kristallogr., 7, 35-48 (1952).

SOVIET PHYSICS – CRYSTALLOGRAPHY VOL. 1, NO. 5 SEPT.-OCT., 1956

ELECTRON-DIFFRACTION STUDY OF THE STRUCTURE OF GERMANIUM FILMS OBTAINED BY VACUUM DEPOSITION

S. A. Semiletov

Institute of Crystallography, Academy of Sciences of the USSR

Translated from Kristallografiya, Vol. 1, No. 5,
pp. 542-545, September-October, 1956
Original article submitted May 19, 1956

The structure of sublimed germanium films was studied as a function of the character of the substrates, their temperature, the rate of deposition, and the thickness of the films. Various types of crystallite orientation were found; these were associated both with the presence of the plane substrate and the rectilinear propagation of the atomic beams. Highly oriented films (single-crystal type) could be obtained by evaporating onto germanium single crystals.

It is well known [1] that when germanium is evaporated in vacuum onto a substrate held at a temperature below 370°C an amorphous film is formed; in order to obtain crystalline films, the substrate temperature must be raised above 370°C. Very different results were obtained by the author of a recently published paper [2], in which it was asserted that, on vacuum-depositing germanium onto cleavage faces of zinc blende, crystalline films were formed even at 250°C. The reduction of the critical temperature to 250°C was explained in [2] as being due to the similarity between the lattice spacings of Ge and ZnS (5.63 and 5.42 Å) and between their respective chemical bonds.

In the present investigation we studied the structure of thin germanium films as a function of the nature and temperature of the substrate, the rate of deposition, and the thickness of the films. The germanium was vacuum-evaporated from tungsten evaporators heated by electric currents. Graphite evaporators heated by electron bombardment were also used.

For the condensing substrates we used glass and quartz plates, corundum, carborundum, mica sheet, and cleavage faces of rocksalt, calcite, fluorite, and silicon. We also made a large number of experiments involving deposition on single-crystal germanium surfaces after grinding and etching.

The substrate temperature during condensation was measured by an iron–constantan thermocouple and in individual experiments varied from room temperature to 950°C. The film thickness was determined by weighing the substrates before and after deposition; it varied from 0.01 to 20 μ. The evaporation rate was determined from the film thickness and the time required to deposit the films. In individual experiments the evaporation rate varied from 10^{-7} to $2 \cdot 10^{-5}$ g/cm^2 · sec, i.e., by 150 to 200 times.

In accordance with published data [1], on evaporating the germanium onto cold (room temperature) substrates, we obtained amorphous films. Crystalline films were obtained on evaporating germanium onto substrates heated above 370°C.

Let us now consider the results obtained by studying the structure of the films.

For rapid sublimation of germanium onto glass, polished quartz, or corundum (heated to 400°C), polycrystalline films were formed (Fig. 1). Subsequent annealing of these samples at 400 to 900°C for 1 to 6 h had no effect on the structure of the films. In all the electron-diffraction photographs obtained with polycrystalline films, we observed the 222 ring, which is forbidden by the structure factor; the presence of this was noted earlier [3] and associated with dynamic effects.

It is well known [4] that thin films often develop texture, this being associated with the presence of the plane substrate and nonuniform development of the crystal faces. In the case of metal films ob-

Fig. 1. Electron-diffraction picture of a polycrystalline Ge film.

tained by sublimation, the formation of texture requires, in some cases, that the sublimation should be effected onto a heated substrate and in others that the samples should be annealed at some definite temperature after sublimation [5].

In our experiments with germanium, textures of various kinds developed during rapid evaporation onto substrates heated above 500°C. Thus, for example, when germanium was deposited on polished graphite plates, calcite crystals, and silicon carbide heated to 550 or 600°C, textures comprising germanium crystallites oriented with the (110) and (100) faces parallel to the substrate (the first of these predominating) were obtained; when the germanium was evaporated onto glass at 520°C, texture with orientations (111) and (100) developed, while for evaporation onto polished corundum at 700 to 800°C the (100) faces lay parallel to the substrate.

Later, on studying films 10 to 20 μ thick, we found that the germanium texture was connected not only with the presence of the plane substrate, but also with the fact that, in the course of vacuum evaporation, there was a unidirectional flow of the material supplying the crystallites, owing to the rectilinear propagation of the atomic beams (so-called feeding texture). In contrast to the types of orientation mentioned above, in this case the crystallites set with their (110) face parallel to the substrate, or perpendicular to the direction of the atomic beam.

The variety of textures formed on substrates by evaporated germanium is apparently connected with the isometric habit of the crystallites, by virtue of which the disposition of one or another of the faces parallel to the substrate may depend on an extremely small difference in the conditions of deposition.

In the case of feeding textures, only one unvarying type of orientation was observed; judging from the lengths of the arcs on the diffraction pictures (Fig. 2), the orientation here was more perfect than in the case of textures associated with the plane substrate.

Fig. 2. Electron-diffraction picture of Ge texture.

Fig. 3. Point electron-diffraction picture of a Ge film obtained by deposition on calcite.

Apart from photographs of polycrystalline samples and textures, we also obtained point electron-diffraction pictures indicating the presence and azimuthal orientation of germanium crystals relative to the substrates. The most perfect orientation occurred when depositing germanium on cleavage faces of calcite and mica (Fig. 3).

By solving the point electron-diffraction pictures we found that, in the case of calcite, the germanium crystallites were set with the (111) face parallel to the $(10\bar{1}1)$ face of the calcite, for a substrate temperature of about 520 to 600°C, and sometimes with the (100) face so oriented. In the case of mica, the germanium crystals were also set with the (111) face on the substrate, or more rarely the (110) face. Diffraction photographs of this type always showed weak Debye rings as well as point reflections, indicating that some of the crystallites were not oriented. Point diffraction pictures were obtained for films up to 10^{-5} cm thick. Thicker films only constituted textures and polycrystalline aggregates. We also evaporated germanium onto germanium single crystals, ground and subsequently etched. These experiments were aimed at elucidating the possibility of growing a germanium single crystal by crystallization from the vapor phase in vacuum. Apart from its theoretical interest, this question has considerable practical importance. It is well known that a layer of germanium produced by vacuum evaporation has hole-type conductivity [6]; hence, by evaporating onto an n-type single crystal we might well expect to produce crystals with p-n junctions. In this respect, it is particular-

Fig. 4. Electron-diffraction picture of an etched germanium single crystal.

Fig. 5. Electron-diffraction pictures of germanium films obtained by deposition on the etched surface of a single crystal.

Fig. 6. Electron-diffraction picture of an etched germanium single crystal.

Fig. 7. Electron-diffraction pictures of germanium films obtained by deposition on the etched surface of a single crystal.

ly interesting to study the structure of the layer growing on the single crystals and to determine the conditions under which it will acquire a single-crystal nature.

The crystals were etched in hydrogen peroxide. Figures 4 and 5 show electron-diffraction photographs obtained from one of the single crystals before and after depositing a 2-μ layer. The layer was deposited on the surface of a crystal heated to 520°C, the 2-μ layer being deposited in 30 min (slow evaporation). The fact that Fig. 5 contains reflections forming a regular lattice indicates that under these conditions a layer with the structure of a mosaic single crystal forms on the original single crystal. The cross shape of some reflections indicates that the growing layer includes crystallites with octahedral faces, possessing insufficient resolving power [5].

Figures 6 and 7 present electron-diffraction photographs obtained from another single crystal before and after depositing a 2-μ layer. The crystals were heated to 520°C and the deposition took 3 min (rapid evaporation). The presence of Kikuchi lines on the diffraction pattern of Fig. 7 indicates the formation of a single-crystal layer with a more perfect structure than that of the earlier case. Hence, increasing the evaporation rate improves the structure of the deposited layer. Increasing the substrate temperature leads to the same result.

As indicated earlier, the author of [2] observed crystalline germanium films on evaporating germanium onto crystal faces of zinc blende heated to 250 rather than 370°C, and explained this as being due to the similarity between the lattice spacings and chemical bonds in the two structures. This is rather unexpected. It is certainly well known that similarity between the spacings and bonds leads to the orientation of the evaporated crystallites on the crystalline substrate. As regards crystallization from the vapor phase during vacuum sublimation, so far as we know the formation of a crystalline or amorphous phase is determined by the substrate temperature and the time of holding the sample at some temperature rather than by the similarity of the lattice spacings or identity of chemical bonds. Elementary consideration of the crystallization process indicates that the formation of a crystalline or amorphous phase depends mainly on the mobility of the atoms; if the atoms on the substrate have low mobility and cannot assemble into aggregates (high viscosity), an amorphous phase is formed; if, however, the mobility of the atoms is sufficient for the formation of nuclei, then a crystalline phase is formed. From this point of view it is quite clear that raising the substrate temperature increases the kinetic energy and mobility of the atoms, and thus favors the formation of a crystalline phase. As regards the closeness of the lattice spacings and identity of the bonds, it is not really quite clear how these can facilitate the formation of a crystalline phase. If identity of bonds and similarity of lattice spacings facilitated the formation of a crystal-

line phase, then, clearly, by substituting germanium crystals for ZnS (depositing germanium on germanium) we could still further lower the temperature for the formation of the crystalline films.

In view of this, we made some special experiments and found that, on depositing germanium on germanium single crystals heated to 250 or even 370°C, only amorphous films were formed. Crystalline films formed above 370°C. Thus we must regard the results of [2] as erroneous.

LITERATURE CITED

1. G. Haas, "Studies on the structure and behavior of thin evaporated films of silver, aluminum, silicon, and germanium," Phys. Rev., 72, 174 (1947).
2. A. Segmüller, "Texturuntersuchungen an dünnen Zinn-und Germaniumschichten," Z. Krist., 107, 1/2, 18-35 (1956).
3. R. Heidenreich, "Theory of 'forbidden' (222) electron reflection in the diamond structure," Phys. Rev., 77, 2, 271-284 (1950).
4. B.K. Vainshtein, "Electron-diffraction texture photographs," Tr. Inst. Kristallogr., 6, 173-193 (1951).
5. Z.G. Pinsker, Electron Diffraction [in Russian] (1949).
6. J. Thornhill and K. Lark-Horovitz, "Films of germanium," Phys. Rev., 82, 762-763 (1952).

SOVIET PHYSICS - CRYSTALLOGRAPHY VOL. 1, NO. 5 SEPT.-OCT., 1956

MEASUREMENT AND RECALCULATION OF THE DYNAMIC ELASTIC CONSTANTS FOR QUARTZ

V. G. Zubov and M. M. Firsova

M. V. Lomonosov State University, Moscow

Translated from Kristallografiya, Vol. 1, No. 5,
pp. 546-554, September-October, 1956
Original article submitted July 13, 1956

The dynamic constants have been measured by Bergmann's method, with independent and direct determinations of c_{11}, c_{33}, c_{44}, and c_{66}. It is shown that Lawson's piezoelectric corrections are needed. Discrepancies are observed between the c_{44} and c_{14} determined in different ways, but the Laval-Raman theory eliminates the discrepancies and gives a fuller description of the dynamic behavior.

Introduction

Much attention has recently been given to the limitations of Vogt's theory of the dynamic elastic behavior of crystals and to the construction of a new atomistic theory. Laval and Raman have made major advances in this respect.

Laval [1], in 1951, and Raman [2], in 1955, employed very general concepts on particle interaction in rather different demonstrations that Vogt's theory is not applicable to the general case of dynamic processes in crystals, which for complete description require 45 independent constants instead of Vogt's 21. The Laval-Raman theory also predicted discrepancies between static and dynamic measurements of the adiabatic constants; it implied a markedly different relation between the elastic moduli s_{ik} and the elastic constant c_{ik}.

The new theory naturally demands a fresh examination of the existing experimental evidence and much more careful new direct measurements of elastic constants, especially for quartz, a material of great technical importance.

It has been shown [3] that there is no agreement on the numerical values for the elastic constants of quartz; direct measurements independent of results for other constants are available only for c_{11} and c_{66}, even now.

The most careful and precise dynamic determinations of the adiabatic constants are those of Atanasoff and Hart [4], Mason [5], and Nomoto [6]. Atanasoff and Hart found only c_{11} and c_{66} directly by measurement of vibrational frequencies for quartz plates; the other constants were found by calculation. In particular, their values for c_{33} and c_{13} are very unreliable, as very complicated equations are involved. Mason deduced c_{66}, c_{44}, and c_{14} from the thickness modes of AT-cut plates, the others being calculated from the s_{ik}. Vogt's theory gives equations different from those of the Laval-Raman theory, so these values cannot be used.

Nomoto used Bergmann's method to deduce all the constants from the diffraction figures given by ultrasound in a quartz cube. In this way he found c_{33} independently, as well as c_{11} and c_{66}.

The errors in the directly measured constants do not exceed 0.5%, whereas those in the calculated ones are 0.5-1%, except for Nomoto's c_{44} and Atanasoff and Hart's c_{33} and c_{13}, which give over 1%.

Table 1 lists the most reliable effective values for the c_{ik}.

The values of Table 1 take no account of the differences in the experimental conditions; no piezoelectric corrections have been applied. Atanasoff and Hart obtained two different values for c_{14} by measurement of natural frequencies with different circuits; Lawson's [7] corrections eliminated the discrepancy. These corrections are required not only for resonance in plates, but also in Bergmann's method. The most reliable values, as thus corrected, are then as given in Table 2.

Table 2 also lists adiabatic values deduced from Vogt's static measurements; these deviate widely from the dynamic results in nearly all cases, and the discrepancies are not explicable on Vogt's

TABLE 1

Source	$c_{ik} \cdot 10^{-10}$ dyne/cm²				
	c_{11}	c_{33}	c_{44}	c_{66}	c_{14}
Atanasoff and Hart	87.55	—	57.19	40.74	17.25/18.40
Mason	—	—	58.65	40.5	18.2
Nomoto*	87.31	105.7	57.55	—	17.51

*From the original paper [6]; other values are usually given in the literature, as a result of incorrect normalization of Nomoto's results. Bhagavantam's values could not be included, as we have been unable to obtain the original paper.

TABLE 2

Source	$c_{ik} \cdot 10^{-10}$ dyne/cm²				
	c_{11}	c_{33}	c_{44}	c_{66}	c_{14}
Atanasoff and Hart	86.75	—	58.0	39.9	17.97
Mason	—	—	58.6	40.3	18.2
Nomoto*	86.5	105.7	57.8	—	17.5
Vogt	85.4	105.4	57.1	39.1	16.9

*Nomoto's c_{44} has not been corrected, because the error of measurement exceeds the correction.

theory, whereas they agree with the Laval-Raman theory. There is also fairly poor agreement over the dynamic c_{44} and c_{14}, which cannot be explained in Vogt's theory.

Here we describe new independent measurements of some of the constants, which were made in order to clear up these discrepancies.

Methods

We used Bergmann's method [8], because it is far more flexible than the purely electronic methods. A particular advantage is that all the constants can be determined on the same specimen; further, it is possible to use in the calculations modes that do not allow of direct piezoelectric excitation, and that cannot be detected by electronic methods. This gives independent access to c_{33}, c_{44}, and c_{14}, as well as c_{11} and c_{66}; in addition, the equations are much simplified, and it is possible to check that the orientation is correct by reference to invariant relations.

Figure 1 shows the system used to observe the diffraction by the ultrasound, which produces very complex diffraction patterns in the focal plane of O_2, which reflect the symmetry of the crystal and the presence of three types of waves along each direction.

Figure 2 shows some of the patterns recorded. Each pair of spots here corresponds to a plane wave whose wavelength Λ may be calculated from

Fig. 1. The apparatus: L) light source; K) condenser lens; F) filter; D) pinhole; O_1) collimator lens; A) specimen; O_2) lens; B) screen or plate in focal plane of lens.

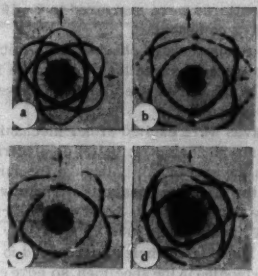

Fig. 2. Diffraction patterns for various directions of observation: a) along Z axis; b) along Y axis; c) along X axis; d) at 45° to the X and Z axes.

$$r_n = nF \cdot \frac{\lambda}{\Lambda},$$

in which r_n is the distance from the central maximum to that of order n, F is the focal length of the lens, and λ is the wavelength of the light.

The Λ are used with independent measurements of the frequency and density to find the effective elastic constants corresponding to these waves, and hence the principal constants.

Atanasoff and Hart derived [4] the following equations for the thickness modes from Vogt's theory:

a) waves along the X axis:

$$c_{11} - k = 0, \qquad (X_1)$$

$$(c_{66} - k)(c_{44} - k) - c_{14}^2 = 0 \qquad (X_2, X_3)$$

b) waves along the Y axis:

$$(c_{11} - k)(c_{44} - k) - c_{14}^2 = 0, \qquad (Y_1, Y_2)$$

$$c_{66} - k = 0, \qquad (Y_3)$$

c) waves along the Z axis:

$$c_{33} - k = 0, \qquad (Z_1)$$

$$c_{44} - k = 0, \qquad (Z_2)$$

(X_1), (Y_1), and (Z_1) give the effective coefficients for quasi-longitudinal waves; the others are for

quasi-transverse waves. We have used these equations with our data.

The light source was a mercury arc type PRK or SVDSh, which was filtered to isolate $\lambda = 5461$ Å; Lenzos interference filters were used, the band width and peak transmission being checked from spectrograms. O_2 had a focal length of 167.0 cm; O_1 had 50 cm. The pinhole was 0.01 mm in diameter. The patterns were measured to $2 \cdot 10^{-4}$ mm with an IZA-2 comparator.

These readings were checked from microphotometer traces; corrections were made in certain cases by measuring the distances between higher-order spots.

The waves were excited either mechanically (with a quartz piezoelectric plate) or electrically (directly in the specimen); both gave the same values for the effective constants. The power was provided by the usual three-point oscillator: output power 80 W, peak output 3000 V, frequency range 8-12 Mc.[1] These frequencies correspond to the 30-40th harmonics in the specimen, so edge effects are small. The frequencies were measured to 0.02% with a heterodyne wavemeter.

The specimens were made at the Institute of Crystallography from fine natural quartz as cubes $20 \times 20 \times 20$ mm oriented on the principal axes; they were carefully checked for orientation and absence of twins.[2]

The diffraction patterns also provided a test for twinning, while the invariants [3] provided a check on the orientation.

The constants should be obtained with errors not exceeding 0.2% under these conditions.

All results quoted for velocities and elastic constants at room temperature are derived from 400-600 independent measurements; these numerous data provided a good test of the performance, and the individual values seldom deviated by more than 0.5% from the mean, except when photographs of poor quality were used.

The final values are means from six cubes and nine plates; here again the deviations from the mean did not exceed 0.5% for properly oriented specimens.

Results and Discussion

The measurements were made at 20°C for waves propagating along all the principal directions. Table 3 gives the effective elastic constants k for the various modes.

Calculation from Vogt's theory gives c_{11}, c_{66}, c_{33}, and c_{44} directly from the k for (X_1), (Y_3), (Z_1), and (Z_2), respectively; the coefficients for (X_2) with (X_3) or (Y_1) with (Y_2) may be taken in pairs to give c_{14} and c_{44} by Atanasoff and Hart's method, and also to test the results for consistency. Table 4 presents this test.

Tables 1 and 4 show that our c_{11} and c_{66} agree satisfactorily with the direct and independent determinations by others.

Tables 1 and 4 also show that the c_{14} calculated in the various ways are in conflict, as in Atanasoff and Hart's work. This conflict, together with the agreement over c_{11} and c_{66} for identical electrical conditions, would indicate that results from Bergmann's method require piezoelectric corrections such as Lawson applied to Atanasoff and Hart's results. Table 5 gives our results for 20°C and fixed electric field as corrected in this way.

These corrections give good agreement between the c_{44} as found in the various ways, but left unaltered the spread in c_{14}.

Comparison of Tables 2 and 5 leads to the following conclusions.

1. Our results show that static measurements give a large and persistent deviation from dynamic ones for all the adiabatic constants except c_{33}. Our data on these disagree with Vogt's and with all others.

2. Our c_{33} agree closely with Nomoto's (also determined directly) and do not confirm the $c_{33} = 106.8$ suggested by Atanasoff and Hart, and also by Cady [9]. The complicated calculation evidently introduces some gross error; it is better to reject this value and to use $c_{33} = 105.5$ as the most probable. The static and dynamic values here are in agreement.

3. Our c_{44} (found directly and independently) agrees well with Mason's value, whereas calculation via Atanasoff and Hart's equations gives good agreement with their value, the difference between the calculated and directly measured c_{44} exceeding the errors of measurement. The difference be-

TABLE 3

	Mode							
	(X_1)	(X_2)	(X_3)	(Y_1)	(Y_2)	(Y_3)	(Z_1)	(Z_2)
Effective elastic constants $k \cdot 10^{-10}$ dyne/cm^2	87.38	68.0	28.92	94.96	49.47	40.37	105.4	58.9

[1] We are indebted to E. N. Volkova for assembling all the electronic equipment.

[2] We are indebted to A. B. Gil'varga for excellent work on the preparation and testing of the specimens.

TABLE 4

	c_{11}	c_{33}	c_{44}	c_{66}	c_{14}
Independent and direct determination	87.38	105.4	40.37	58.4	—
From (X_2) and (X_3)	—	—	—	56.55	17.8
From (Y_1) and (Y_2)	—	—	—	57.05	16.95

TABLE 5

	c_{11}	c_{33}	c_{44}	c_{66}	c_{14}
Independent and direct determination	86.6	105.4	39.6	58.4	—
From (X_2) and (X_3)	—	—	—	57.35	17.4
From (Y_1) and (Y_2)	—	—	—	57.85	17.6
Mean	—	—	—	57.6	17.5

TABLE 6

	n_{11}	n_{33}	n_{44}	n_{66}	n_{55}	n_{14}	n_{17}
Our data	86.6	105.4	58.4	57.6	39.6	—	17.5
Atanasoff and Hart	86.75	—	—	58.0	39.9	18.4	17.97
Mason	—	—	58.6	—	40.3	18.2	—
Nomoto	86.5	105.7	—	57.6	—	—	17.5
Mean	86.6	105.5	58.5	57.7	39.9	18.3	17.7

tween our c_{14} and Mason's also exceeds the error of measurement.

We thus have here a new conflict that cannot be explained on Vogt's theory, as for the conflict between the static and dynamic measurements.

The Laval-Raman theory explains the discrepancies for c_{44} and c_{14}; it replaces Vogt's matrix for the elastic constants by the form [10]:

$$\begin{array}{cccccccccc}
n_{11} & n_{12} & n_{13} & n_{14} & 0 & 0 & n_{17} & 0 & 0 \\
 & n_{11} & n_{13} & -n_{14} & 0 & 0 & -n_{17} & 0 & 0 \\
 & & n_{33} & 0 & 0 & 0 & 0 & 0 & 0 \\
 & & & n_{44} & 0 & 0 & n_{17} & 0 & 0 \\
 & & & & n_{55} & n_{17} & 0 & n_{17} & n_{17} \\
 & & & & & n_{66} & 0 & n_{14} & n_{14} \\
 & & & & & & n_{55} & 0 & 0 \\
 & & & & & & & n_{44} & n_{14} \\
 & & & & & & & & n_{66}
\end{array}$$

The effective constants for (X_2), (X_3), (Y_1), and (Y_2) are dependent on n_{55} and n_{17} [3], while those for (Z_2) and for shear waves in AT sections are dependent only on n_{44} and n_{14}. Then Atanasoff and Hart's method for c_{44} and c_{14} in fact gives n_{55} and n_{17}; direct measurement of c_{44} and c_{14}, or use of Mason's method, gives n_{44} and n_{14}. The conflict is thus to be expected on the Laval-Raman theory.

The various previous results can then be interpreted to give the constants at room temperature and constant electric field (Table 6).

This table shows that the Laval-Raman theory gives much better agreement between results than does Vogt's theory; the predicted difference between n_{44} and n_{55}, or between n_{14} and n_{17}, is actually observed. We have also shown that the differences persist at all temperatures up to the transition point. The better agreement and lack of conflict show that the Laval-Raman theory gives a fuller and more exact description of the dynamic elastic behavior.

Raman drew the same conclusion from the data on cubic crystals.

The table also shows that the Laval constants n_{44}, n_{55}, n_{14}, and n_{17} must replace c_{44} and c_{14} when the usual equations are used to find the natural frequencies of quartz plates in any section.

Conclusions

Bergmann's method provides direct and independent measurement of c_{33} and c_{44}, as well as c_{11} and c_{66}, the errors being less than 0.5%. The re-

sults need Lawson's piezoelectric corrections, on account of differences in the conditions for the various elastic constants, which is clear from a comparison of the results with those obtained in other ways.

Our results confirm that the static adiabatic constants of quartz inevitably deviate from the dynamic ones; they also reveal a conflict (not predicted by Vogt's theory) between the c_{44} and c_{14} derived from different natural vibrational modes of quartz.

The Laval-Raman theory is applied to remove these conflicts and to give good agreement between the various sets of results. It is concluded from these successes that the Laval-Raman theory gives a fuller and more correct description of the dynamic elastic behavior of crystals.

We are indebted to A.V. Shubnikov and I.S. Zheludev for direction and discussion, and to Professor Laval of the College de France for providing access to his and Le Corré's data.

LITERATURE CITED

1. J. Laval, "Sur l'élasticité du milieu cristallin. L'état solide," Rapports et Discussions, Congrès Solvay 1951 Bruxelles. Stoops 273.
2. C.V. Raman and K.S. Viswanathan, "The elastic behavior of isotropic solids," Proc. Ind. Acad. Sci., 42, 1,1-9 (1955); C.V. Raman and K.S. Viswanathan, "On the theory of the elasticity of crystals," Ibid., 42, 2, 51-70 (1955); C.V. Raman and D. Krishnamurti, "Evaluation of the four elastic constants of some cubic crystals," Ibid., 42, 3, 111-129 (1955).
3. V.G. Zubov, "A study of the dynamic elastic properties of quartz," Dissertation [in Russian] (Moscow University, 1956).
4. J. Atanasoff and P. Hart, "Dynamical determination of the elastic constants and their temperature coefficients for quartz," Phys. Rev., 59, 85 (1941).
5. W. Mason, "The application of quartz crystals," Bell System Tech. J., 22,2,178 (1943).
6. O. Nomoto, "Über die Eigenschwingungen und die Elastizität des Quarzes," Proc. Phys.-Math. Soc. Japan, 25, 4, 240 (1943).
7. A. Lawson, "Comment on the elastic constants of alpha-quartz," Phys. Rev., 59, 838 (1941).
8. L. Bergmann, Der Ultraschall (Zurich, 1954).
9. W. Cady, Piezoelectricity [Russian translation] (IL, 1949).
10. J. LeCorré, "Constants élastiques at piézoélectriques cristallines," Bull. Soc. Franc. Min. Crist., 76, 464-479 (1953).

SOVIET PHYSICS – CRYSTALLOGRAPHY VOL. 1, NO. 5 SEPT.-OCT., 1956

SOME ASPECTS OF THE DIFFRACTION OF LIGHT BY ULTRASONIC WAVES IN QUARTZ

V. G. Zubov and M. M. Firsova

M.V. Lomonosov State University, Moscow

Translated from Kristallografiya, Vol. 1, No. 5,
pp. 555-556, September-October, 1956
Original article submitted July 13, 1956

Tests do not confirm Bergmann's result for the ratio of peak intensities in diffraction of light by longitudinal and shear waves; a new effect is observed in the diffraction at fast shear waves propagating along the X axis of quartz.

A crystal can carry three waves along any direction: one quasi-longitudinal (compression wave) and two quasi-transverse (shear waves). The displacements occur in three mutually perpendicular directions, and the velocities are usually different.

An assertion often encountered in the literature is that the diffraction at shear waves is much weaker than that at longitudinal ones; Bergmann [1] has repeatedly asserted that the diffraction spots corresponding to shear waves must always be weaker than those corresponding to compression waves, and also that it is almost always impossible to detect higher-order diffraction peaks from shear waves.

But we observed (in a study of the elasticity of quartz via diffraction at ultrasonic waves [2,3]) that this is far from being the case; the intensity ratio in the peaks is very much dependent on the resonance and excitation conditions. Mechanical excitation (from another quartz crystal) usually produced weaker spots from the shear waves, but electrical excitation enables one to obtain any intensity ratio. Slow shear waves along the X and Y axes, and shear waves in 45° XZ sections, are most strongly excited and give the best patterns, resonance, and excitation conditions being the same. These waves produce higher-order diffraction peaks as easily as do compression waves; ones up to the order of 16 are readily observed even in fairly weak fields.

Figure 1 shows a pattern with high-order peaks produced by slow shear waves propagating along the X and Y axes. Figure 2 shows a similar pattern from compression waves propagating along the X axis, which required stronger fields than did the pattern of Fig. 1.[1]

This erroneous assertion may have arisen because coupling to shear waves is very difficult in mechanical excitation. This difficulty would lead to unequal amplitudes and hence to a systematic difference in the ratio of the intensities.

Slow shear waves along the X axis show an effect that does not fit the Raman-Nata treatment of diffraction intensities.

Figure 3 shows the pattern seen along the Z axis in quartz when that axis coincides exactly with the incident beam. Slow shear waves along the X axis then produce peaks of even order very much stronger than those of odd order; the even ones are so strong that secondary peaks resembling the basic pattern are formed around them. A deviation of only 1° from the correct setting of the Z axis causes a pronounced change in the intensity ratios; the first-order peak becomes strongest, the intensity falling monotonically toward the higher orders. This fall is the same on both sides of the zero order, so that there is no unilateral extinction of peaks.

It is difficult to explain the diffraction seen along the Z axis for fast shear waves propagating along the X axis.

Figure 3 shows that the peaks corresponding to these are scarcely visible in the main diffraction pattern seen along Z, although there are gaps at

[1]We are indebted to photographic technician V. A. Vinogradov for processing the color photographs.

the appropriate points in the second rings of the main and higher-order figures. Figure 3 also shows two diffraction points within the first ring of the main figure, and also the same within the first rings of the higher-order figures. The distance between points in adjacent figures show that they correspond to fast shear waves along X and arise from diffraction of the beams corresponding to the odd peaks produced by the slow shear waves along X, not from diffraction of the main beam.

Figure 3 thus shows that diffraction along Z arises from fast shear waves along the X axis in quartz only when the slow shear waves along the same axis are strongly excited; and even then it occurs in the beams corresponding to the odd peaks produced by the slow shear waves.

These effects are not explicable by existing approximate theories of diffraction at ultrasonic waves; they require a more rigorous and complete treatment of the orientation effects produced by excitation of shear waves.

LITERATURE CITED

1. L. Bergmann, Der Ultraschall (Zurich, 1954).
2. V.G. Zubov, "A study of the dynamic properties of quartz," Dissertation [in Russian] (Moscow State University, 1956).
3. V.G. Zubov and M.M. Firsova, "Measurement and recalculation of the dynamic elastic constants of quartz," Kristallografiya, 1, 5, 546-554 (1956).

Fig. 1

Fig. 2

Fig. 3

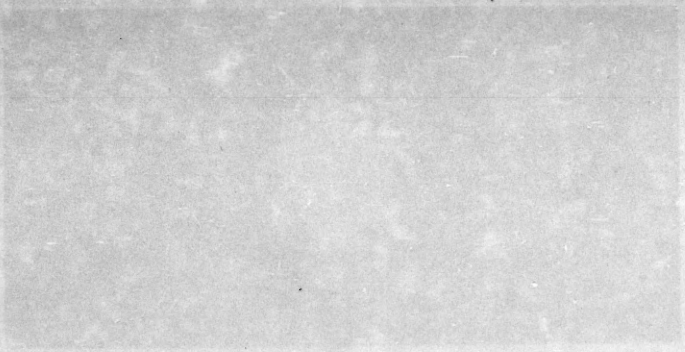

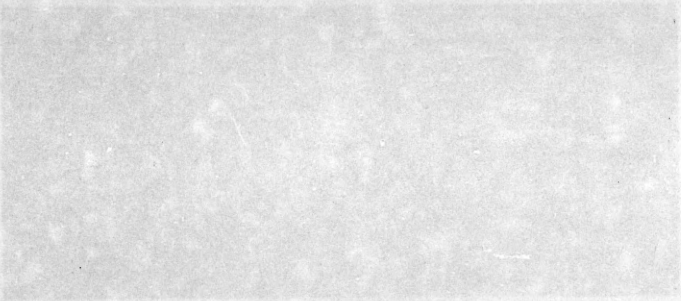

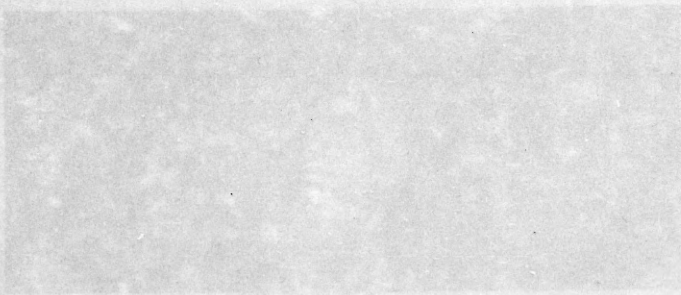

SOVIET PHYSICS - CRYSTALLOGRAPHY VOL. 1, NO. 5 SEPT.-OCT., 1956

SOME RESULTS ON THE PHOTOELECTRET STATE IN SULFUR SINGLE CRYSTALS

V. M. Fridkin

Institute of Crystallography, Academy of Sciences of the USSR

Translated from Kristallografiya, Vol. 1, No. 5,
pp. 557-563, September-October, 1956
Original article submitted August 11, 1956

The photoelectret charge has been measured as a function of intensity and time of illumination during polarization. The lifetime of the residual polarization is discussed.

Introduction

Polarization in photoconducting crystals was studied by Hilsch and Pohl [1], after it had been shown [2] that photopolarization in crystals is associated with the accumulation of a space charge due (at least in part) to electron trapping. Later [3,4] additively colored alkali halides were used in measurements of the spectral distribution of the depolarization current. These curves had two peaks, which correspond to transition into the conduction band from the F centers (the main short-wave peak) and from the F' centers, the latter associated with defects. The polarization during photoconduction was due to the transitions from the F centers into the conduction band, where the electrons are displaced by the external field and eventually become trapped at F' centers. Photodepolarization is due to transition into the conduction band from F and F' centers, the electrons then migrating in the field of the space charge. Similar deductions have been drawn [5] for single crystals of sulfur. The photopolarization of sulfur has also been examined by Kurrelmeyer [6] and Vorob'ev [7]; amorphous selenium shows a similar effect [8].

Nadzhakov, in 1937, discovered fixed internal photopolarization in polycrystalline sulfur [9] and examined the lifetime of the state in the dark. He found that a polycrystalline plate retained its polarization unchanged for at least 15 h, in which it resembled the electrets discovered by Eguchi in 1921. The heterocharge on an Eguchi electret is due to the temperature dependence of the ion mobility and dipole relaxation time.

Nadzhakov's electrets are evidently produced via photoconduction and trapping of displaced charges at localized levels. Nadzhakov proposed [9] the name photoelectrets, Eguchi electrets then being thermoelectrets. The methods devised for charge measurement on electrets could then be applied to photopolarization.

Nadzhakov has since made further measurements of the lifetime of the polarization in polycrystalline sulfur and of the effects of temperature on the polarization [10,11]. He showed [10] that the purity and thermal history of the material are important. The polarization persisted almost unaltered for 37 h in pure polycrystalline sulfur (maker Kahlbaum), whereas sulfur of commercial grade showed a considerable fall in this time. In addition, he found that single crystals showed a more rapid fall. Brief illumination during polarization revealed that the photopolarization proper is accompanied by dark polarization (which arises when a field is applied in the dark); the latter is dependent on the dark resistance and eventually decays to zero, whereas the photopolarization cannot be completely eliminated by internal dark conduction.

A recent paper [12] deals with the persistent internal polarization produced by visible light, ultraviolet, x rays, and fast electrons; it also reports the relation of charge to polarization conditions and seeks to relate the polarization to photoconduction and luminescence. However, no data are presented on the lifetime of the polarization (electret state proper). Another recent paper [13] merely presents essentially Nadzhakov's results of 1937.

Here we report preliminary results for the photoelectret state in single crystals, as the persistent (or slowly decaying) internal photopolarization in a single crystal appears to have a bearing on crystal physics generally. It is also of interest to compare the lifetime and production conditions for single crystals with those for polycrystalline aggregates.

The persistent internal polarization in a polycrystalline material is equivalent to a polar texture of symmetry $\infty \cdot m$ (Shubnikov); Nadzhakov showed that such a texture is stable in pure polycrystalline sulfur. Residual polarization in a single crystal is equivalent to a special polar direction, which in general is equivalent to alteration of the initial symmetry to the symmetry of one of the subgroups of $\infty \cdot m$. It is of interest to compare the magnitude and lifetime of the polarization for nonpolar, polar, and special polar directions, particularly as regards the anisotropy of these for a given crystal. It is to be expected that the production conditions and magnitude will vary with the direction. The lifetime of the internal polarization is the lifetime of the altered symmetry.

Here we give results only on the production conditions and lifetime for photopolarization in sulfur single crystals.

Methods

We used plates about 1 cm^2 in area and 1-1.5 mm thick, cut from natural crystals of orthorhombic sulfur perpendicular to the acute bisector of the optic axes; in a few cases we used cubes whose faces were perpendicular to the diad axes. The specimens were brought to a mirror finish by polishing on silk wetted with kerosene.

The measurements were made with the vacuum-tube electrometer described in [14]; the measuring cell is shown in Fig. 1. The body 1 has a hole to admit light, which is closed by the quartz plate 2 held by ring 3, which carries a brass grid, which acts as one electrode. The second electrode 4 is of aluminum and is held in the amber insulator 7 mounted in the top 6, which fits tightly in the body. The specimen 5 is gripped between the two electrodes by the spring 8; it has no guard-ring, because surface leakage in sulfur is very slight [7]. The polarizing voltage is applied to the body of the cell and hence to the grid electrode; the aluminum electrode is connected to the grid of the electrometer tube.

The cell was placed in a thermostat whose temperature was adjustable up to 100°C; this allowed

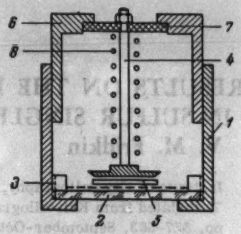

Fig. 1. The measuring cell.

entry of a beam of light parallel to the polarizing field. The intensity at the specimen was measured with an exposure meter of known spectral response, for which purpose the cell was moved to one side.

The thermostat and light source (PRK-4 mercury arc) were mounted on an optical bench. The high voltage was provided by an electronically stabilized supply. All measurements were made in terms of the steady-state reading.

The voltage was usually applied at the same time as the illumination, the latter being turned off after a set time; the voltage was then removed and the grid electrode was grounded. The plate was left in the dark for a set time with the electrodes joined together; the charge was measured by depolarization in response to fresh illumination (depolarization current as a function of time). The polarization (numerically equal to the surface charge density) was usually evaluated from the initial discharge current. The current could also be integrated to give the charge released; the polarizing current was also recorded as a function of time.

Results

Polycrystalline aggregates and single crystals were used, the latter 1 cm^2 by 1.5 mm thick (see above); polycrystalline specimens of about the same size were made by melting these plates, with subsequent recrystallization by Nadzhakov's method [15].

The specimen was polarized under white light for 10 min at 200 V; then the electrodes were grounded, the specimen being left for a set time in the dark. The charge was measured by depolarization.

Figure 2 shows the results as the ratio of the initial discharge current i_t at time t after the polarization to i_0, the same immediately after polarization. The single crystal retained hardly any polarization after 50 h in the dark, whereas the

polycrystalline specimen retained about 40% after 90 h.

The effect is to be ascribed to differences in the conditions for electron trapping at localized levels. The activation energy governs the trapping time, and this is clearly much greater for the polycrystalline specimen. The limiting (perhaps finite) value of the polarization for the polycrystalline material demands special consideration.

The charge (polarization) of a single crystal is also dependent on the intensity and illumination time (Figs. 3-5).

Figure 3 shows i_0 as a function of intensity during polarization for 10 min in white light at 200 V for a single crystal. The intensity could be varied by moving the source and by inserting metal grids (neutral filters). The discharge current was measured 5 min after the end of the illumination period, the depolarizing intensity being always $3 \cdot 10^{-4}$ W per cm^2. This figure also shows the initial current during polarization as a function of intensity; the two are linearly related, but the polarization shows saturation, which is apparent even at $E = 5 \cdot 10^{-5}$ W/cm^2.

Figure 4 shows the relation of initial discharge current to intensity at low intensities; the polarization produced at $2.4 \cdot 10^{-8}$ W/cm^2 was equivalent to $i_0 = 1.3 \cdot 10^{-11}$ A, while the dark polarization produced in the same time was equivalent to $i_0 = 0.5 \cdot 10^{-11}$ A. The photopolarization effect thus differs appreciably from dark polarization even at this relatively low intensity; but it is of little significance to attempt to divide the total polarization into light and dark parts as regards lifetime, because the over-all polarization of a single crystal eventually falls to zero. On the other hand, such a division is desirable for polycrystalline material, because the dark polarization decays to zero, but the photopolarization is not lost completely [10].

Figure 5 shows the photopolarization (in terms of i_0) as a function of illumination time. The single crystal was polarized with white light ($3 \cdot 10^{-4}$ W

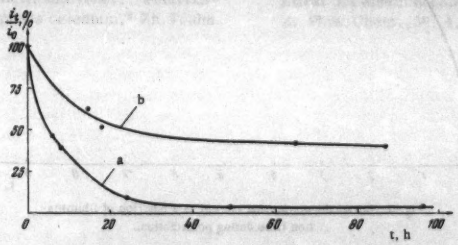

Fig. 2. Residual polarization in: (a) single crystal of sulfur; (b) polycrystalline aggregate.

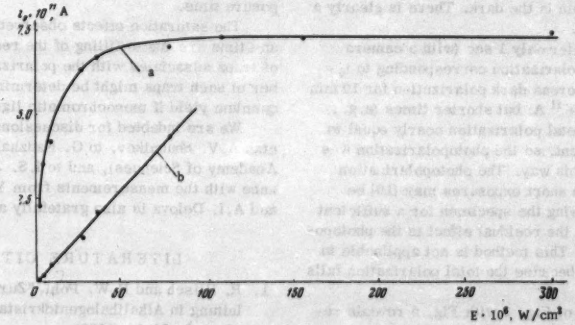

Fig. 3. Intensity dependence of: (a) initial depolarization current; (b) initial polarizing current.

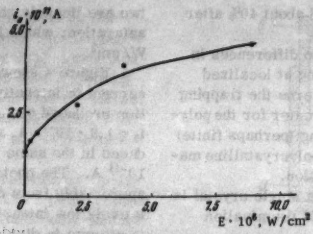

Fig. 4. Intensity dependence of initial depolarization current for low intensities during polarization.

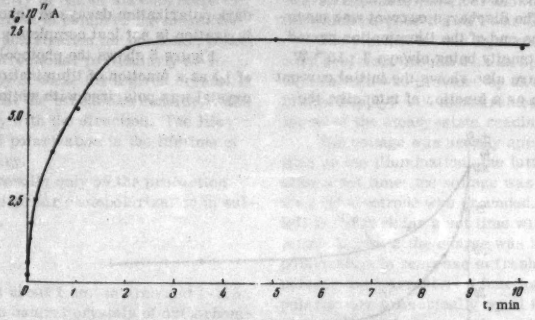

Fig. 5. Initial depolarization current as a function of illumination time during polarization.

per cm² at 200 V, the latter always applied for 10 min. Depolarization was by white light at $3 \cdot 10^{-4}$ W/cm² after 5 min in the dark. There is clearly a saturation effect.

Illumination for only 1 sec (with a camera shutter) gave a polarization corresponding to $i_0 = 0.8 \cdot 10^{-11}$ A, whereas dark polarization for 10 min gave only $0.5 \cdot 10^{-11}$ A; but shorter times (e.g., 0.2 sec) gave a total polarization nearly equal to the dark component, so the photopolarization was undetectable in this way. The photopolarization produced by such short exposures may [10] be measured by leaving the specimen for a sufficient time in the dark; the residual effect is the photopolarization alone. This method is not applicable to single crystals, because the total polarization falls rapidly to zero.

Comparison of Fig. 3 with Fig. 5 reveals reciprocity failure for the internal polarization; a given Et (in which E is intensity and t is time) produces a residual polarization dependent on the exposure time.

The saturation effects observed for intensity and time are due to filling of the restricted number of traps associated with the polarization. The number of such traps might be determined from the quantum yield if monochromatic light were used.

We are indebted for discussions to Academician A.V. Shubnikov, to G. Nadzhakov (Bulgarian Academy of Sciences), and to I.S. Zheludev. Assistance with the measurements from Yu.N. Martyshev and A.I. Delova is also gratefully acknowledged.

LITERATURE CITED

1. R. Hilsch and R.W. Pohl, "Zur Elektronenleitung in Alkalihalogenidkristallen," Z. Phys., 87, 1-2, 78-88 (1933).

2. P.S. Tartakovskii, "Über die Polarisation bei der lichtelektrischen Leitfähigkeit von röntgenisiertem Steinsalz," Z. Phys., 66, 11-12, 830-833 (1930).
3. P.S. Tartakovskii and D.M. Kaminker, "Space charges in photoconduction. Part I," Zh. Éksperim. i Teor. Fiz., 10, 2, 139-144 (1940).
4. D.M. Kaminker, "Space charges in photoconduction, Part II," Zh. Éksperim. i Teor. Fiz., 10, 2, 145-149 (1940).
5. P.S. Tartakovskii and G. Rekalova, "The internal photoelectric effect and a possible scheme for the electron energy levels in sulfur," Zh. Éksperim. i Teor. Fiz., 10, 1025-1029 (1940).
6. B. Kurrelmeyer, "The photoelectric conductivity of sulfur," Phys. Rev., 30, 6, 893-910 (1927).
7. A.A. Vorob'ev, "A photoelectric study of sulfur single crystals," Zh. Éksperim. i Teor. Fiz. 4, 368-383 (1934).
8. D.N. Nasledov and E.K. Malyshev, "Polarization effects in amorphous selenium," Zh. Tekhn. Fiz., 16, 10, 1135-1140 (1946).
9. G. Nadzhakov, "Über eine neue Art von Elektreten: Photoelektreten," Phys. Z., 39, 6, 226-227 (1938).
10. G. Nadzhakov and N.T. Kashukeev, "Studies on photoelectrets," Izv. Bulgar. Akad. Nauk., ser. fiz., 2, 321-337 (1951).
11. G. Nadzhakov and N.T. Kashukeev, "Polarization change in a photoelectret in response to temperature," Izv. Bulgar. Akad. Nauk., ser. fiz., 3, 103-115 (1952).
12. H. Kallman and B. Rosenberg, "Persistent internal polarization," Phys. Rev., 97, 6, 1596-1610 (1955).
13. E.D. Padgett, "Phototransistors and photoelectrets," Radio-Electronics, 2 (1955).
14. A.I. Froiman and V.M. Fridkin, "A study of the heterocharge on Carnauba wax electrets," Kristallografiya, 1, No. 3 (1956).
15. G. Nadzhakov, "Über einen photovoltaischen Effekt bei einem hochisolierenden Körper," Z. Phys. Chem., 36, 4, 314-321 (1937).

SOVIET PHYSICS - CRYSTALLOGRAPHY VOL. 1, NO. 5 SEPT.-OCT., 1956

STUDY OF THE STRUCTURE OF KINK BANDS IN THALLIUM HALIDE CRYSTALS

M. V. Klassen-Neklyudova and A. A. Urusovskaya

Institute of Crystallography, Academy of Sciences of the USSR

Translated from Kristallografiya, Vol. 1, No. 5,
pp. 564-571, September-October, 1956
Original article submitted May 19, 1956

An optical and x-ray study has been made of kink bands in TlBr–TlI specimens having different crystallographic orientations. Complete agreement has been found between the optical pattern and the results of the x-ray study. The gradual nature of kink-band formation has been investigated. Indications have been obtained to the effect that slip traces are not always present in a kink band.

We have found [1] that in the longitudinal bending of TlBr–TlI crystals, kink bands are sometimes formed in them. The term "kink" is used by us to denote a form of deformation resulting in the elbow-shaped bending of the specimens, when part of a specimen is displaced in relation to the other part, and a transition zone is formed between the displaced parts. We call this transition zone a kink band. In another of our investigations [2], a study was made of the conditions under which the deformation of crystals of thallium and cesium halides was accompanied by kink-band formation. It was found that kink bands were not formed when the crystals were subjected to uniform tension. They were formed only if tension was accompanied by macroscopic bending. In the case of deformation by compression, the kinks were formed at the ends or in the middle part of the specimen if compression was accompanied by longitudinal bending. Thus, kink formation is always due to the presence of nonuniformly distributed stresses.

Optical investigations showed that the crystal lattice gradually changes its orientation over the width of the band connecting the crystal parts which have been displaced in relation to each other. The gradual change in orientation results from the formation of two opposing fans of wedge-shaped portions [1].

The present article deals with a more detailed study of the structure of this transition region (kink band).

Specimens of TlBr–TlI crystals, in which a sharply pronounced kink band had been formed on compression accompanied by longitudinal bending, served as objects of the investigation. The bands in specimens of three crystallographic orientations were studied. The principal axis of one specimen formed an angle of 26° with the [100] direction (slip direction); the principal axis of the second specimen coincided exactly with the [100] slip direction; in the third specimen, the principal axis was parallel to the [111] direction.

Study of Specimen in which the Compression Axis Formed an Angle of 26° with the [100] Direction

Photographs in polarized and natural transmitted light of this specimen are reproduced in [1]. A thin section, 0.15-mm thick, parallel to the (110) plane, was prepared from this specimen. The thin section was made in the following way. A plate 3 mm thick was cut from the specimen by means of an automatic fret saw (TlBr–TlI crystals are difficult to dissolve and, therefore, it was not possible to cut them by means of a thread moistened with a solvent). For removing the surface layer, damaged in cutting, from one side, this plate was ground (with emery) on ground glass for about 1 mm. The surface of the plate was then polished, and the plate was stuck onto glass by the polished side to avoid bending when subjecting the other side to a similar treatment. A number of Laue diffraction patterns were

Fig. 1. Laue pattern from non-deformed part of specimen. The indices of the spots are shown (exposure, 4 h).

obtained from this thin section, using wide x-ray beams (diameter 1.5 mm). The x-ray irradiation used was from a tube with a molybdenum target, voltage 57 kV and current 10 mA. Exposure was 4 to 12 h.

First of all, the specimen was adjusted so that the x rays passed strictly along the [110] direction. Adjustment was made according to Laue patterns from an undeformed portion of the specimen (Fig. 1). Laue patterns from the kink band were then taken. Figure 2 is a diagram showing the structure of part of a kink band, drawn from a photomicrograph of the thin section. The circles in the diagram mark the places for which Laue patterns were photographed. The width of the band was such that the x-ray beam completely covered it. Laue patterns of the kink band showed splitting of the spots along the circumference into a number of reflections (Fig. 3). Radial broadening of the spots was not observed. This is evidence of the fact that the x-ray beam passed strictly along the axis of rotation of the lattice. Since the x-ray beam passed along the [110] direction, the axis of rotation of the lattice was the [110] direction.

In the microscopic study of this specimen, it was observed that all the wedge-shaped regions were made up of slip traces,[1] changing their direc-

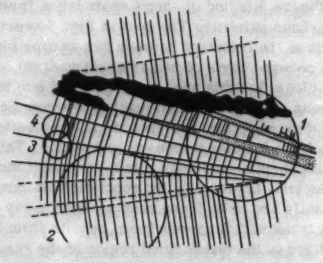

Fig. 2. Diagram of kink-band structure in a TlBr–TlI crystal, drawn from a photomicrograph. The circles 1 and 2 mark the places subjected to x-ray study with a wide x-ray beam (diameter 1.5 mm); the circles 3 and 4 denote places from which Laue patterns were obtained with an x-ray beam 0.1 mm in diameter.

Fig. 3. Laue pattern from kink band (exposure, 12 h).

Fig. 4. Photograph in natural transmitted light of part of kink band in a TlBr–TlI crystal with impact figures formed in it. Demonstrates lattice rotation in the kink band.

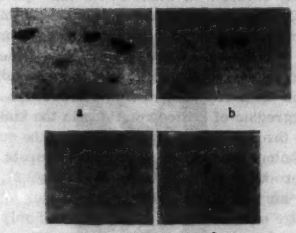

Fig. 5. Form of Laue pattern spots taken (a) from entire kink band (part 1, Fig. 2), set of 34° angles; (b) from edge of kink band (part 2, Fig. 2, exposure 10 h), set of 10° angles; (c) from boundary of two wedge-shaped regions (part 3, Fig. 2), and, (d) from an individual wedge-shaped region (part 4, Fig. 2).

[1]By the term "slip traces" we understand bands visible in thallium halide crystals in transmitted polarized light, owing to double refraction caused by local internal stresses, and in natural transmitted light, owing to local variation of the index of refraction.

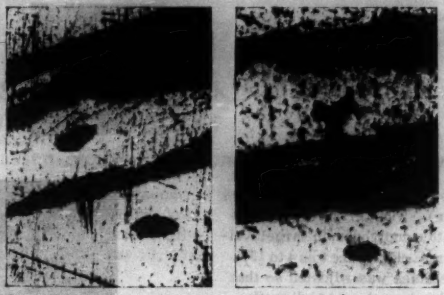

a b

Fig. 6. Photomicrographs of two cuts of TlBr–TlI crystal, compressed in the [100] direction. Impact figures produced inside and outside the kink band; (a) cut along the (110) plane; (b) cut along the $(1\bar{1}0)$ plane.

tion on passing from one edge to another (Fig. 4). The plane of the thin section was perpendicular to the slip planes, so that judging by the arrangement of the slip traces, the axis of rotation of the lattice was situated in a slip plane, and was perpendicular to the slip direction.

Figure 5 shows individual x-ray pattern spots taken from two portions of the specimen. The spot in Fig. 5a corresponds to the case where the beam entirely covered the whole of the band (part 1 in Fig. 2). The complete x-ray pattern for this case is shown in Fig. 3. According to measurements made on a gnomonic projection of this Laue pattern, the aggregate of the reflections corresponding to a spot on the x-ray pattern (Fig. 1) corresponded to the aggregate of lattice rotations in the kink as a whole through an angle of 34°. When the second x-ray photograph was taken, one of the spots of which is reproduced in Fig. 5b (part 2 in Fig. 2), the x-ray beam was displaced from the center to close to the edge of the specimen, and covered only a few wedge-shaped regions. In this case, the spot had a spread of 10° and consisted of five separate reflections. Each pair of adjacent reflections corresponded to two wedge-shaped regions rotated through approximately 2° in relation to each other.

According to optical measurements, the lattice in adjacent wedge-shaped regions of this crystal was also rotated through an angle of 2° [1]. From a comparison of the results of the optical and x-ray measurements, it may be said that in this case the x-ray beam covered approximately five wedge-shaped regions. This conclusion is in agreement with the number of wedges covered by the beam (part 2) in Fig. 2. The degree of broadening of these spots was ascertained by superimposing two x-ray patterns: one taken from an undeformed part of the specimen (Fig. 1), and the other from a kink band (Fig. 3).

Furthermore, to obtain information on the state of the lattice inside the wedges and on their boundary, x-ray patterns of these parts were obtained by means of a narrow x-ray beam 0.1 mm in diameter. The narrow beam was produced by placing a lead diaphragm 0.1 mm in diameter at the exit of the x rays from the collimator. In taking these x-ray patterns, a tube with a tungsten target was used (voltage 57 kV, current 13 mA, exposure 40 to 60 h).

Figure 5 (c and d) shows spots taken from two of the Laue patterns. The spot in Fig. 5c corresponds to the boundary between two wedges (the beam covered parts of two adjacent wedges). It is quite clear that this spot can be divided into two reflections, with an angular spacing between them of ~2°. Figure 5d shows a spot of an x-ray pattern taken from inside a wedge-shaped region. This spot is quite unsplit, and near it is a very faint radial diffuse tail, invisible in the reproduction. Similar faint tails are to be found near spots in x-ray patterns taken with a narrow beam, remote from the kink band in the undeformed region of the specimen.

On the basis of the x-ray patterns reproduced (in Figs. 5a-d), it may be concluded that the splitting of the spots is due to the presence of the aggregate of rotated regions, i.e., to macroscopic distortion of the crystal. The slip traces present in

the interior of the wedges do not cause asterism of Laue spots.

Lattice rotations in the kink band can be demonstrated very graphically by means of impact figures [3]. Figure 4 shows a photomicrograph of a portion of a kink band. The wedge-shaped parts and the displacements inside them are clearly to be seen (photography in nonpolarized light). In addition, two large impact figures, produced by means of a needle, are visible. One of these figures has been applied outside the kink, and the other inside it. The long axis of the figures coincides with the [110] direction. From the mutual arrangement of the impact figures, it may be seen that the lattice in the kink band has been rotated with reference to the lattice of the original crystal, and it is even possible to make an approximate estimate of the angle of rotation.

Study of a Specimen with the Axis Parallel to the [110] Direction

Figure 6 shows lattice rotations in a kink band by means of impact figures in another TlBr–TlI specimen, compressed along the principal axis, parallel to the direction of the cube edge. Both photographs were taken in nonpolarized light. The plane of cut of the plate shown in Fig. 6a was perpendicular to the axis of rotation of the crystal lattice, while the plane of cut of the plate shown in Fig. 6b was parallel to that axis and perpendicular to the first cut. Both plates were approximately parallel to planes of the rhombododecahedron. In the first figure, the impact figures both inside and outside the kink band (i.e., in the latter case, in the nondeformed region) have the same form but are rotated in relation to each other through an angle of 28°. The axis of rotation is normal to the polished surface of the cut, i.e., it is the [110] direction. In the second cut (Fig. 6b), the axis of rotation of the lattice lies in the plane of the cut, and impact figures corresponding to the kink band and to the nondeformed part of the crystal have different symmetries; whereas, outside the band, the impact figure has a two-fold axis of symmetry (corresponding to the crystal symmetry in the [110] direction), inside the band, the impact figure has approximately a three-fold axis of symmetry and corresponds to a plane close to [111]. Inside the kink band, the lattice has been rotated in such a manner that in place of the rhombododecahedron plane there has emerged a plane close to the octahedron plane.

The lattice in the kink band is not in the twinning position in relation to the original crystal, since the interface between them is not a plane of symmetry of the conjugate lattices. This conclusion is based on x-ray patterns taken perpendicular to the cut, shown in Fig. 6a, from a part containing a kink-band boundary. The contact boundary was found to have the indices (241) in relation to the initial lattice, and the indices (17.17.10) in relation to the rotated part of the crystal (kink band).

Unlike the specimen shown in Fig. 4, in the present case there were no slip traces in the kink band. Subsequent experiments with ten specimens with this orientation confirmed the absence of slip in the band.

Study of Specimen with Its Axis Parallel to the [111] Direction

A general view of this specimen, in which the principal axis coincided with the [111] direction, in polarized transmitted light is shown in Fig. 7. On compression, the specimen underwent a smooth longitudinal bend, and assumed a form reminiscent of a cosine curve with a 3/4 period. On compression, two kinds of bands were formed, one (1-1) of which passed through the entire cross section of the specimen, while the other (2-2) failed to reach the other side of the specimen. Inside both kink bands there were many cracks, but in the second band (incompleted kink) cracks were considerably fewer.

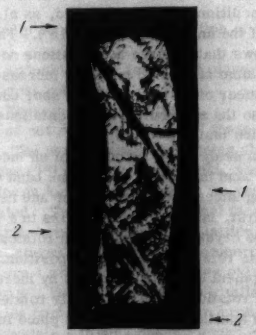

Fig. 7. Photograph in polarized light of TlBr–TlI specimen compressed along an axis parallel to [111]. As a result of the compression, two kink bands were formed, one (the bottom one) of which failed to pass through the entire specimen.

On examination of the structure of the incomplete kink, an impression was gained of the gradual nature of its development. Figure 8 shows Laue spots taken from three different parts of the incomplete kink. During exposure, the x-ray beam passed along the [110] direction, coinciding with the direction of the axis of rotation of the lattice in the band, which is shown by splitting of the spots only on the circumference. The x-ray pattern spot (Fig. 8a) taken from the end of the band, corresponds to the initial stage of kink formation. This Laue spot shows that in the initial stage of deformation there were no considerable lattice rotations, the lattice distortions were quite small and produced only slight broadening of the Laue spots in the radial direction. The middle part along the length of the band corresponds to more intense deformation when considerable lattice rotations were already taking place. In the Laue pattern (Fig. 8b), taken from this part of the kink band, circumferential splitting of the spots into three spots with a final angle of rotation of 9° can be observed. The intensity of the additional spots, however, is very small. This shows that an insignificant part of the crystal volume was in the rotated position. In the initial part of the band of the incomplete kink, situated close to a lateral surface of the specimen, the deformation of the crystal was greater. The considerable intensity of the additional spots in the x-ray photograph shown in Fig. 8c indicates that a larger volume of the crystal was in the rotated condition. In this case, the number of additional spots increased, as also did the range of the angles of rotation (18°). This latter fact shows that at large deformations not only does the volume of rotated material increase, but also the number of rotated regions, and, consequently, also the set of discrete orientations of the crystal lattice inside the kink band.

Thus, a study of the structure of an incomplete kink band has shown that a kink band develops by spreading successively into newer and newer regions. At first, lattice rotation occurs in a small region of the crystal, and the lattice rotates through a small angle relative to the initial position. Further development of the band occurs by increase of the angle of rotation in the previously rotated region and, in addition, rotation takes place in adjacent parts situated on either side of the originally formed band.

In both kink bands of this specimen, as in the specimen compressed along the [100] direction (Fig. 6), no slip traces were visible.

We shall examine the arrangement of the kink bands in relation to the crystallographic axes in the three specimens studied. In the first of them (the principal axis of the specimen made an angle of 26° with the [100] direction), the kink band was situated at an angle of 48° to the principal axis, or at an angle of 106° to the [100] direction. In the second specimen (the principal axis was parallel to the [100] direction), the kink band was formed at an angle of 74° to the principal axis, coinciding with the slip direction. In the third specimen, the kink band made an angle of 31° with the [111] axis, or 85° with the [100] slip direction. On a basis of the comparison of these data, it may be concluded that a kink band is always formed approximately perpendicularly to the planes and direction of slip, but not in the direction of action of the maximum cleavage stresses, as might be expected.

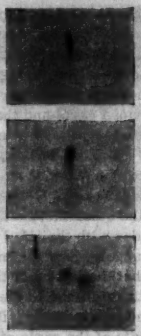

Fig. 8. Laue spots corresponding to three places in an incomplete kink; (a) end; (b) middle; (c) beginning.

Discussion of the Results

An x-ray study of kink bands in TlBr–TlI crystals has shown that a kink band consists of an aggregate of wedge-shaped regions rotated in relation to each other.

The rotation of the lattice in individual (adjacent) wedge-shaped regions does not occur gradually but abruptly, with a jump. The results of the x-ray study are in agreement with an optical study and with a study of the rotation by means of impact figures. Such abrupt lattice rotations in the case of kinking have not been observed in other crystals, for example in zinc [4], cadmium [5], CsI [6]. The authors of articles on the investigation of these crystals consider that there is smooth bending of slip planes in kink bands. This view, however, is not shared by other investigators. Gilman [7] affirms that in kink bands of zinc crystals, fracture of slip

planes occurs, not their bending. Moore has confirmed this experimentally [8]. He measured the slope of the basal planes in relation to the original crystal in a twin and in the accommodation bands adjacent to the twin. He found that the accommodation bands, representing transition zone, like kink bands, consisted of one or more undistorted regions, rotated through angles of 10'-30' in relation to each other and to the original crystal.

We consider that on deformation, kink formation does not occur by bending of the lattice but by discrete rotations. The magnitude of an elementary rotation depends on the plastic properties of the investigated crystal, and also on the experimental conditions (crystallographic orientation of the specimen, rate of deformation).

It should be noted, however, that in investigating the structure of kinks, it is necessary to take into account the time elapsing between the moment of producing the kink and its examination. Grounds for such a conclusion may be provided by Honeycombe's experiments [9] in explanation of the influence of recovery on kink-band structure in cadmium and aluminum. From Laue patterns of kink bands in cadmium at different stages of recovery, Honeycombe discovered that closely situated faint spots in the course of time merged into a number of strong spots situated fairly remote from each other. In aluminum single crystals, this phenomenon was not observed at room temperature, but heating to 600°C was necessary for merging of the spots. After high-temperature annealing of deformed specimens of cadmium, intensive recrystallization occurred and the entire kink band was transformed into two grains.

The specimens we studied had been kept for a long time (several months) before x-ray examination. It is possible that during this period their recovery occurred, and small slightly rotated wedge-shaped regions united to form larger portions, more considerably rotated in relation to each other, thereby increasing somewhat the abruptness of the rotations.

Furthermore, in all the foreign articles on the study of kink bands in metals, it is pointed out that the kink boundary bisects the angle between the slip traces situated on either side of this boundary. Orowan [5], in outlining kink formation, states that the lattices in such regions are not in a mutually twinning position, although the plane of contact is common to both of them. In contradistinction to this, however, Kolontsova et al. found that in CsI crystals, in one part of a kink band, the lattice of one of the wedge-shaped regions was rotated in relation to the original crystal in accordance with the twinning law. In the twinned components, the (113) plane was common to both.

Stepanov [10] points out that in the flaking of rocksalt crystals, the boundaries of the flakes are not crystallographically equivalent in adjacent rotated regions (flakes). Our investigations of a kink band in TlBr – TlI [1] gave a similar result. Repeated measurement of the angle between the boundaries of the wedge-shaped regions and the slip traces inside them in one of the specimens showed that one of the boundaries of these regions was perpendicular to the displacements, while the other made with the first boundary an angle of 2°, being perpendicular to the displacements present in the adjacent wedge-shaped region.

It may be concluded from this that the rotation of the lattice may not only be symmetrical, as occurs in a CsI crystal, but also nonsymmetrical, when the adjacent rotated regions do not represent a twin.

The presence of slip traces in the wedge-shaped parts of a kink band may lead one to conjecture that nonsymmetrical rotation is performed by reason of slip accompanied by rotation of slip planes around a direction perpendicular to the direction of slip and situated in the slip plane.

Currently, therefore, the following proposals exist concerning the mechanism of kink-band formation:

1. Slip accompanied by bending of the slip planes;
2. Slip accompanied by rotation of the slip planes;
3. Twinning on an irrational plane [11], i.e., symmetrical rotation;
4. Nonsymmetrical rotation.

We do not support the first of these four proposals. The participation of twinning along irrational faces [6] and nonsymmetrical reorientation of the lattice in kink-band formation we regard as demonstrated. Twinning on irrational faces and nonsymmetrical reorientation of the lattice represent different stages of the same phenomenon.

Figure 4 shows that slip traces exist inside each wedge. We have observed a similar phenomenon in the compression of cesium bromide and iodide crystals. In kink bands formed in these crystals, in all the orientations we have investigated, slip traces (the same slip elements as in the case of TlBr – TlI) were always present.

It should be noted, however, that we have observed slip traces in specimens examined either after completion of the deformation process (Fig. 4),

during the deformation process by filming at a rate of 24 frames per second, or when kink bands were fully formed in the time between two frames (in a time < 0.04 sec) [2]. On the basis of these data, we were unable to affirm that lattice reorientation in the wedge-shaped regions and slip necessarily occur simultaneously. Slip could develop even after reorientation of the lattice. The photograph in Fig. 6 and the additional investigations of nine specimens (the axis of compression of six specimens was parallel to [100], the axis of compression of three specimens was at a small angle to the [100] direction), in which we also failed to observe slip traces on examination in polarized light, support the possibility of lattice rotation occurring without the participation of slip.

Summary

1. Kink bands in three specimens of TlBr–TlI having different crystallographic orientations have been studied.
2. Complete correspondence between the optical pattern of the kink-band structure and the form of the Laue spots has been shown; kink bands are an aggregate of regions rotated in relation to each other.
3. The axis of rotation is the [110] direction.
4. Kink bands are developed approximately perpendicularly to the slip planes.
5. The gradual nature of kink-band formation has been studied in the case of an incompleted kink.
6. It is shown that kink formation is not always accompanied by slip. Kinks may be formed by means of nonsymmetrical lattice rotations.

The radiography was carried out in the X-Ray Laboratory of the Institute of Crystallography. We are extremely grateful to Academician N.V. Belov for the facility to work in the laboratory supervised by him.

LITERATURE CITED

1. A.B. Zemtsov, M.V. Klassen-Neklyudova, and A.A. Urusovskaya, "Complicated manifestation of plastic deformation in single crystals," Dokl. Akad. Nauk SSSR, 91, 4, 813-816 (1953).
2. M.V. Klassen-Neklyudova and A.A. Urusovskaya, "Influence of nonuniform stressed state on the mechanism of the plastic deformation of thallium and cesium halides," Kristallografiya, 1, 1, 410-418 (1956).
3. A.A. Urusovskaya, "Plastic deformation figures observed in crystals of TlBr–TlI, CsI, CsBr," Tr. Inst. Kristallogr., 12, 172-179 (1956).
4. J.B. Hess and C.S. Barrett, "Structure and nature of kink bands in zinc," Trans. AIMME, 185, 599 (1949).
5. E. Orowan, "A type of plastic deformation new in metals," Nature, 149, 3768, 643-644 (1942).
6. E.V. Kolontsova, I.V. Telegina, and G.M. Plavnik, "The structure of kink bands in some ionic crystals," Kristallografiya, 1, 4, 419-424 (1956).
7. J.J. Gilman, "Mechanism of ortho kink-band formation in compressed zinc monocrystals," J. Metals, 6, Sec. 2, 5, 621-629 (1954).
8. A. Moore, "Accommodation kinking associated with the twinning of zinc," Proc. Phys. Soc., 12, 956-958 (1952).
9. R. Honeycombe, "Inhomogeneities in the plastic deformation of metal crystals," J. Inst. Metals, 80, 45-56 (1951-1952).
10. A.V. Stepanov and A.V. Donskoi, "New mechanism of plastic deformation of crystals," Zh. Tekhn. Fiz., 24, 2, 161-183 (1954).
11. N.A. Brilliantov and I.V. Obreimov, "Plastic deformation in rocksalt. III," Zh. Éksperim. i Teor. Fiz., 5, 330-339 (1935); "Plastic deformation. IV," Zh. Éksperim. i Teor. Fiz., 7, 978-986 (1937).

SOVIET PHYSICS – CRYSTALLOGRAPHY VOL. 1, NO. 5 SEPT.-OCT., 1956

THE POLYMORPHIC TRANSITIONS OF BISMUTH AT HIGH PRESSURES

V. P. Butuzov and E. G. Ponyatovskii

Institute of Crystallography, Academy of Sciences of the USSR
Translated from Kristallografiya, Vol. 1, No. 5,
pp. 572-576, September-October, 1956
Original article submitted June 9, 1956

The phase diagram of 99.995% Bi has been examined at pressures up to 30,000 kg/cm^2 and at temperatures from normal up to the melting points of the phases. The β phase melts at 184°C between 17,300 and 22,400 kg/cm^2, so β-Bi melts without change of volume, whereas the melting point of γ-Bi increases with pressure, with a mean coefficient of 0.0072 deg-cm^2/kg. The $\alpha \rightleftharpoons \beta$ and $\beta \rightleftharpoons \gamma$ transitions are very fast but show substantial hysteresis at all the temperatures used. The ratio of the heats of transition and the volume changes in these transitions have been determined by a thermometric method.

Bridgman [1] first detected the polymorphic transitions in bismuth under hydrostatic pressure; he used the displacement of the plunger. The first (monoclinic) modification is stable up to 25,900 kg per cm^2 at 20°C; the second is stable over the range 25,900 to 27,760 kg/cm^2; and the third is stable at and above 27,760 kg/cm^2. The lattice structures of the latter two modifications are unknown. These three modifications may be denoted in the standard way as the α, β, and γ modifications. Bridgman recorded the melting point of α-Bi as a function of pressure, the α-β and β-γ equilibrium curves over the range −50 to +170°C, the changes in specific volume in the $\alpha \rightleftharpoons \beta$ and $\beta \rightleftharpoons \gamma$ transitions, the heats of transition, and the coordinates of the triple points $\alpha-\beta-$liq, $\beta-\gamma-$liq, $\alpha-\beta-\gamma$.

The transition pressures of bismuth at room temperature are presently the principal reference points in the calibration of manganin resistance gauges. Bridgman determined the transition parameters of bismuth several times [2-5], but only at room temperature. The transition points were detected from the displacement of the plunger and from the resistance, but the latter does not yield important parameters such as the heat of transition or the volume change, while the piston displacement does not yield the volume change for each transition separately, because the two transition points are close together. In his later papers [2,3] he gives the sums of the volume changes for the two. Other disadvantages of his methods are that they do not give access to temperatures above 200-250°C, nor can the transition rates be deduced.

The liquidus line for bismuth was followed up to 22,200 kg/cm^2 in 1953 at this institute by differential thermal methods [6].

We have now made a detailed study of the phase diagram at pressures up to 30,000 kg/cm^2 on bismuth of 99.995% purity[1]; the heats and volume changes in the $\alpha \rightleftharpoons \beta$ and $\beta \rightleftharpoons \gamma$ transitions have also been determined. The hydrostatic pressure was provided by a mixture of isopentane with n-pentane in a pressure amplifier [7]; a manganin device reading to ±100 kg/cm^2 being used in conjunction with an iron–nichrome thermocouple reading to ±1.5°. Full details of the methods have been given elsewhere [8].

The heating and cooling rates were about 1 deg per sec. The transition points were readily detected with the differential and single thermocouples, on account of the fairly high rates of transition and latent heats. Both transitions show appreciable thermal hysteresis; Table 1 gives data

[1] The main impurities in the Bi were: 0.003% Pb, 0.001% Fe, and 0.0003% Hg.

TABLE 1

P °C kg·cm^{-2}	T α→β °C	T β→α °C	T_{av} °C	ΔT
19 300	165	162	163.5	3
21 500	128	122	125.0	6
23 800	73	58	655.5	15

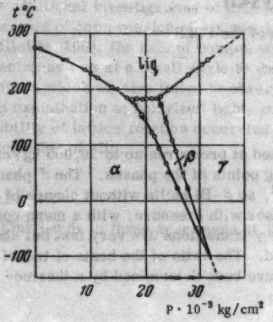

Fig. 1. Phase diagram for bismuth. ○ – Our results; × – Bridgman's results.

on the $\alpha \rightarrow \beta$ and $\beta \rightarrow \alpha$ transitions at various pressures.

The hysteresis in the $\alpha \rightleftharpoons \beta$ transition increases from 3° for T_{av} = 163.5° to 15° at T_{av} = 65.5°, in which T_{av} is the average of the temperatures for the $\alpha \rightarrow \beta$ and $\beta \rightarrow \alpha$ transitions at that pressure.

Figure 1 shows the P–T phase diagram derived from the data results, the points being T_{av}, and each being the mean of at least six measurements. The new melting curve of α-Bi agrees closely with the older one, as do the α-β and β-γ transition curves. The melting point of β-Bi is independent of pressure within the errors of experiment, so β-Bi melts without change of volume. The melting point of γ-Bi rises from 184°C at 22,400 kg/cm^2 to 239° at 30,000 kg/cm^2, the mean slope being 0.0072 deg-cm^2/kg.

The latent heats of the transitions were determined as follows. The bismuth specimen 1 (weight about 6 g) was placed in the glass tube 2 (Fig. 2) inside the container 3, which was closed by the plug 6. The specimen and container had recesses to take the junctions 4 and 5 of the differential thermocouple. The container was placed in the pressure amplifier 7, and the pressure was raised to 25,000 kg/cm^2 (below the first transition point). It was

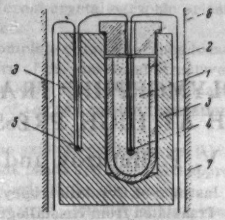

Fig. 2. Method of determining heats of transition in the pressure vessel.

then raised from 25,000 to 28,000 kg/cm^2 over of the apparatus being kept constant at 20°C. The temperature of the specimen was recorded with a Kurnakov system. The ratios of the latent heats of the $\alpha \rightleftharpoons \beta$ and $\beta \rightleftharpoons \gamma$ transitions were deduced from the ratio of the areas on the dta diagram. The heats and volume changes were deduced from four equations in four unknowns:

$$\frac{1}{T}\left(\frac{dT}{dp}\right)_1 = -\frac{\Delta V_1}{Q_1},$$

$$\frac{1}{T}\left(\frac{dT}{dp}\right)_2 = -\frac{\Delta V_2}{Q_2},$$

$$\Delta V_1 + \Delta V_2 = -0.0085 \text{ cm}^3/\text{g} \quad [2,3]$$

$$Q_1 : Q_2 = n.$$

Here, ΔV_1 is the change in specific volume in the $\alpha \rightleftharpoons \beta$ transition, ΔV_2 is the same for the $\beta \rightleftharpoons \gamma$ transition, $(dT/dp)_1$ and $(dT/dp)_2$ are the slopes of the α-β and β-γ transition curves at 20°C, and Q_1:Q_2 = n is the ratio of the heats of transition.

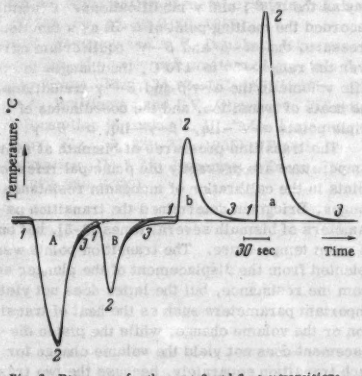

Fig. 3. Dta curves for the $\alpha \rightleftharpoons \beta$ and $\beta \rightleftharpoons \gamma$ transitions.

TABLE 2

	Q_1, cal/g	Q_2, cal/g	ΔV_1, cm^3/g	ΔV_2, cm^3/g	$\alpha \rightleftharpoons \beta - liq$		$\beta - \gamma - liq$		$\alpha - \beta - \gamma$	
					P, kg/cm²	T, °C	P, kg/cm²	T, °C	P, kg/cm²	T, °C
Our data	−1.78	−0.71	−0.0055	−0.0030	17300	184	22400	184	32200	−108
Bridgman [1]	−1.62	−0.68	−0.0047	−0.0035	17300	183	22400	185	32300	−110

In all, we measured the heats six times: in four cases the specimen was held in a lucite cylinder, and in two in a copper cylinder. Figure 3 shows a typical recording made in one run, in which A and B denote, respectively, the $\alpha \rightarrow \beta$ and $\beta \rightarrow \gamma$ transitions (pressure increasing), while a and b denote the reverse transitions (pressure decreasing). Parts 1-2 correspond to absorption (release) of heat, while parts 2-3 correspond to equilibration after the transition. The shape of part 1-2 is governed by the rate of change of pressure. The density of β-Bi is higher than that of α-Bi, so the volume is lower. An applied pressure, only slightly in excess of the equilibrium value, causes the volume to decrease until the equilibrium pressure is reached, at which point the transition stops. The α and β forms then coexist. Complete transition from α-Bi to the β form requires continuing increase in pressure. Part 1-2 (α-β transition) is of low slope when the rate of change of pressure is small; the transition occurs at a fixed pressure. High rates cause part 1-2 to be nearly vertical; the transition occurs in less than 1 sec. The exact time can be evaluated from the recording speeds and the known lag in the system. The slope of part 2-3 is largely independent of the rate of change. These remarks apply also to the $\beta \rightarrow \gamma$, $\gamma \rightarrow \beta$, and $\beta \rightarrow \alpha$ transitions.

The average $Q_1 : Q_2$ is 2.51, with a maximum range of ±2%, in spite of the marked variation in conditions (container materials and rate of pressure variation). Table 2 gives our results, and also Bridgman's.

Both transitions at 20°C involve considerable pressure hysteresis: some 1000 kg/cm² for $\alpha \rightleftharpoons \beta$ and some 900 kg/cm² for $\beta \rightleftharpoons \gamma$. This hysteresis is not dependent on the rate of change. The transition point has been taken as the mean of the pressures for the forward and reverse transitions. This hysteresis has not been reported before; it remains an open question whether the effect is inherent in pure bismuth or is due to impurities.

The heats of the $\alpha \rightleftharpoons \beta$ and $\beta \rightleftharpoons \gamma$ transitions may be used to deduce similar heats for other substances at high pressures.

Conclusions

1. Dta has been applied over the range 1 to 30,000 kg/cm² and temperatures from normal up to the melting points of the phases.

2. The melting point as a function of pressure has been determined for γ-bismuth; the mean coefficient is 0.0072 deg-cm²/kg.

3. The ratio of the latent heats of the $\alpha \rightleftharpoons \beta$ and $\beta \rightleftharpoons \gamma$ transitions at 20°C has been deduced, together with the changes in specific volume.

4. There is appreciable hysteresis in the $\alpha \rightleftharpoons \beta$ and $\beta \rightleftharpoons \gamma$ transitions at heating and cooling rates around 1 deg/sec; the rates of both transitions are high at the temperatures used.

LITERATURE CITED

1. P.W. Bridgman, "Polymorphism principally of the elements, up to 50,000 kg/cm²," Phys. Rev., 48, 11, 893-906 (1935).
2. P.W. Bridgman, "Compressions to 50,000 kg per cm²," Phys. Rev., 57, 3, 235 (1940).
3. P.W. Bridgman, "Compressions and polymorphic transitions," Phys. Rev., 60, 4, 351 (1941).
4. P.W. Bridgman, "The effect of pressure on several properties of the alloys of Bi-Sn and Bi-Cd," Proc. Am. Acad. Arts Sci., 82, 2, 101-156 (1953).
5. P.W. Bridgman, "The use of electrical resistance in high-pressure calibration," Rev. Sci. Instr., 24, 5, 400-401 (1953).
6. V.P. Butuzov, M.G. Gonikberg, and S.P. Smirnov, "Measurement of the melting points of metals at very high pressures," Dokl. Akad. Nauk SSSR, 89, 4, 651-653 (1953).
7. V.P. Butuzov, G.P. Shakhovskii, and M.G. Gonikberg, "Pressure amplifiers for use at high temperatures and very high pressures," Tr. Inst. Kristallogr., 11, 233-238 (1955).
8. V.P. Butuzov, S.S. Boksha, and M.G. Gonikberg, "Polymorphic transitions in phosphorus at very high pressures," Dokl. Akad. Nauk SSSR, 108, 3 (1956).

THE TRANSFORMATION MECHANISM FOR DENDRITIC CRYSTALS

M. O. Kliya

Institute of Crystallography, Academy of Sciences of the USSR

Translated from Kristallografiya, Vol. 1, No. 5,
pp. 577-582, September-October, 1956
Original article submitted June 16, 1956

Cinemicrography has been applied to unstable dendritic crystals; an explanation is offered for the observed decomposition and conversion to a granular structure. The time for detachment of a branch has been measured (to about 20%) as a function of the initial thickness at the point of detachment.

Dendritic crystals are unstable and eventually produce a system of isometric grains, but the process can be very slow. The details are also not visible to the unaided eye.

Time-delay photomicrography has been applied to the stages from dendrites to rounded grains in ammonium chloride at constant temperature; the process is driven by the tendency of the surface free energy to become minimal. The experiments were essentially a repetition of those of Saratovkin [1] with NH_4Cl between glass slides. Aqueous NH_4Cl was chosen because it readily provides the high supersaturations needed for the growth of dendritic crystals.

A drop of the saturated solution was placed between two glass slides in an air thermostat at 70°C. The excess of solution was squeezed out, and the specimen was transferred to the microscope stage, where it cooled to room temperature. Water loss was suppressed with a layer of grease. The cooling was accelerated (to produce high supersaturation) by directing a jet of air onto the specimen. Dendritic crystals usually grew inwards from the edges; the camera was started at this point, the initial stage being recorded at 24 frames per second. At the end of this stage the rate was reduced to 1 or 2 frames per second (early period of conversion of the dendrites), with the intervals increasing gradually toward the end of the experiment (to intervals of 1.5-2 min at 5-7 h). The temperature was kept constant.

The conversion of the dendrites began very soon after they had grown, at which point the solution was no longer supersaturated, so the solid was in equilibrium with the solution, speaking generally; but material is taken up from one part of a dendrite and is deposited on other parts, on account of the differences in equilibrium concentration as between concave, flat, and convex areas (Ostwald-Freundlich formula, assuming the surface tension to be constant).

The surface tension is a function of direction for a crystal, as is clear from the frames shown in Fig. 1 for a closed drop of solution (see [2, 3] for description of the method of making these closed drops). The migration of material continues until $2\sigma_i/l_i$ becomes the same for all faces present in the equilibrium form of the crystal [4] (σ_i is surface tension, l is central distance). Here the variation of σ_i between faces is important, as well as the shape and size of the interfaces. The final frame shows the crystal as a body of nearly constant curvature, the deviations being due to the anisotropy in the surface tension. The solubility of this crystal is the same at all points.

The transformation of dendrites can be explained on this basis. It is clear from the film that material is transported from convex parts to concave ones; but these parts are often widely separated, so there is an additional tendency for material to migrate from adjacent plane areas to concave ones.

Figure 2 illustrates the transformation of flat dendrites of thickness only a few times the wavelength of light. The minor branches appear as though withdrawn into the trunk. Rather thicker

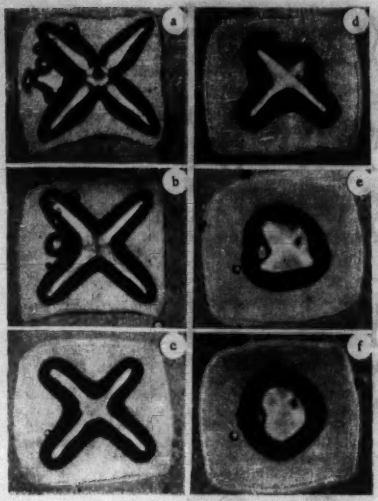

Fig. 1. Transformation of dendritic ammonium chloride crystals in a closed drop of solution, × 525. Time intervals: a-b, 10 min; a-c, 1 h; a-d, 2 h 20 min; a-e, 4 h 30 min; a-f, 36 h.

Fig. 2. Conversion of thin ammonium chloride dendrites, × 675. Time intervals: a-b, 4 h; a-c, 30 h.

dendrites in addition tend to break up, a process that would, at first sight, seem to contradict the Gibbs-Curie-Wulff law. However, the migration from plane and convex faces to concave ones explains the effect, although one might initially suppose that material from the base of a branch would be deposited elsewhere, because the largest negative curvature occurs at the base of a branch (Fig. 3), so this ought to be the site of deposition. The negative curvature seen in the photographs is accompanied by a large positive curvature in a section parallel to the base of the dendrite, and the latter causes the base to dissolve. A closely spaced array of secondary branches causes the process to accelerate, on account of transfer of material from adjacent parts to the concave area at the base. This transport continues until the curvature at that site is largely eliminated. Even before this has been completed, the base has sometimes been so extensively attacked from both sides that the secondary branch is detached from the main one. This detachment occurs the sooner the thinner the secondary branch, as Chernov has shown [5] in terms of a relation of detachment time to thickness.

This time can be measured quite closely (to about 20%) with the microscope (error of measurement 2 sec). For this purpose we used 30 secondaries on a single dendrite, which gave the relation of time to thickness. This agreed reasonably well with Chernov's theoretical curve.

This detachment leaves a sharp spike at the base (Fig. 3f), which has a large positive curvature, so it is rapidly lost. The detached branch also becomes more nearly isometric; material is deposited on it, although it everywhere has positive curvature, especially at the ends, where it dissolves. Some of the dissolved material is deposited on the sides. A detached branch separated from the base by only a few diameters gives rise to appreciable deposition even on the flat parts of the base, even though the detached part has not yet become isometric. This transfer is clear from the reduction in area, although the part may increase somewhat in width. However, even an isometric dendrite is unstable in the presence of a nearby base; its material is gradually transferred to the latter.

These transfer processes continue until all the crystals have the same effective curvature. The rate of conversion to equilibrium (isometric) form is dependent on the separation and disposition of the surfaces that differ in curvature. Convection currents here play no part, and the processes are

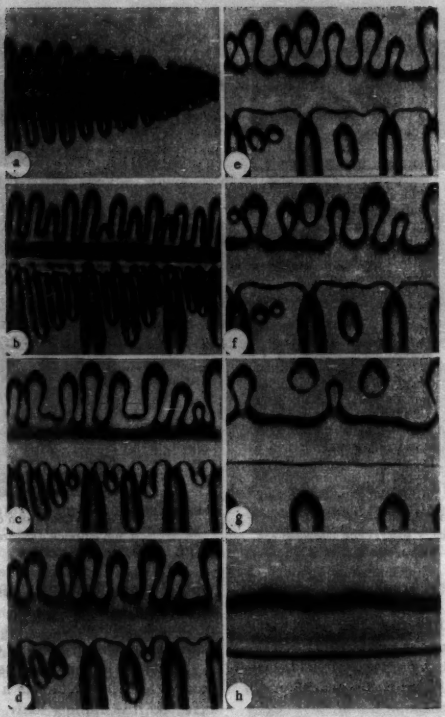

Fig. 3. Transformation and decomposition of dendritic NH_4Cl crystals, × 975. Time intervals: a–b, 6 sec; a–c, 15 sec; a–d, 40 sec; a–e, 50 sec; a–f, 1 min 25 sec; a–g, 4 min; a–h, 5 h.

mainly ones of diffusion; surface diffusion may play some part with isolated crystals.

The conversion rate is also dependent on the temperature; a stage can be frozen by appropriate cooling, as in many metallurgical techniques. Diffusion still occurs in these frozen structures, but only at extremely low rates.

All the secondary branches (whether detached or not) are lost by the time the conversion is fairly well advanced; the specimen consists of interwoven main trunks from different dendrites. The process does not stop at this stage, for the trunks eventually develop necks and break up, the fragments becoming rounded grains. The larger grains then grow at the expense of the small ones. The specimen is then a set of randomly oriented grains in no way resembling the original dendritic structure.

Metal castings cannot be observed in this way. Very often the processes do not go to completion, a frozen structure remaining. Extremely varied polygranular structures may be produced, on account of the anisotropy in crystal structure, surface tension, impurity distribution, etc.

We are indebted to Professor G. G. Lemmlein for direction in this work.

LITERATURE CITED

1. D. D. Saratovkin, Dendritic Crystallization [in Russian] (1953).

2. G.G. Lemmlein, "The conditions for production of crystals of equilibrium shape," Dokl. Akad. Nauk SSSR, 98, 6, 973 (1954).
3. M.O. Kliya, "Production of an equilibrium drop-crystal system," Dokl. Akad. Nauk SSSR 100, 2, 259-262 (1955).
4. V.K. Semenchenko, "Thermodynamics of small objects," Zh. Fiz. Khim., 12, 6, 298 (1945).
5. A.A. Chernov, "Evaluation of the conversion times for inclusions and dendritic crystals," Kristallografiya, 1, 5, 582-587 (1956).

EVALUATION OF TRANSFORMATION TIMES FOR INCLUSIONS AND DENDRITIC CRYSTALS

A. A. Chernov

Institute of Crystallography, Academy of Sciences of the USSR
Translated from Kristallografiya, Vol. 1, No. 5,
pp. 583-588, September-October, 1956
Original article submitted June 16, 1956

Surface-tension effects are considered in relation to the breakup of elongated crystals and inclusions; the conversion time is evaluated as a function of several factors and is compared with the experimental evidence.

Introduction

In 1951-1956, Lemmlein and Kliya reported [1-3] experiments on the effects of surface tension on interfaces between saturated aqueous solutions and crystals of sodium nitrate, ammonium chloride, and silver nitrate. An effect dependent on minimum surface energy was observed: liquid inclusions and branches of dendrites (both effectively long cylinders) spontaneously broke up to products that then took up equilibrium (nearly spherical) shapes. Figure 1 of [3] gives time-lapse photomicrographs that illustrate this.

Here we discuss these effects in the isotropic approximation, which gives an estimate of the decomposition time as a function of surface tension, temperature, concentration, etc.

A dendrite is essentially equivalent to an inclusion, so we consider the latter first.

An elongated cylinder is not the equilibrium shape, so a system containing such an inclusion will tend to alter the shape of the inclusion at constant volume. A sphere has the least surface energy in the isotropic approximation, but the formation of two or more spherical inclusions will also reduce the surface energy (the number actually formed is dependent on the ratio of length to diameter). This in no way implies that all of these cases, or even the most favorable, will actually occur; the detailed mechanism of the transformation is also decisive. The only mechanism available here is diffusion transport within the inclusion (the crystal has infinite viscosity and does not allow of hydrodynamic transformation); this arises from differences in the concentrations of saturated solutions above surfaces differing in curvature.

Consider the inclusion of Fig. 1 (ratio of length l to diameter $2a$ small). The concentration at A is less than that at B, and the diffusing particles travel as shown by the arrows. The process tends to shorten the inclusion while widening it at the center, so the shape tends to come to equilibrium. Now let $l \gg 2a$. It can be shown that the concentration gradients are appreciable only over distances of about $2a$ near the ends, so that the latter

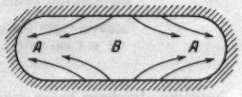

Fig. 1

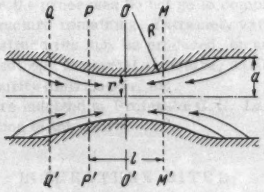

Fig. 2

have no effect on the center for $l \gg 2a$. This is why a long inclusion splits up into several spherical inclusions.

This may be considered more closely. Let us suppose that section OO' (Fig. 2) is slightly narrower than adjacent parts (e.g., because it was formed that way initially), the radius at that point being r. If this change of shape tends to reduce the surface area, then it will give rise to a flux of material that tends to reduce r further. This will continue until the inclusion breaks into two, or, alternatively, further reduction in r does not reduce the energy, e.g., because the ends are approached, with a resulting increase to radius a. This rather complex problem will not be discussed in detail; a simpler approximation will be used.

The mean curvature near OO' is

$$2\left(\frac{1}{r}-\frac{1}{R}\right).$$

If

$$\frac{1}{r}-\frac{1}{R}>\frac{1}{a}, \tag{1}$$

Thomson's formula gives us that the concentration of the saturated solution near OO' will be less than that in adjacent areas; diffusion then continues until the inclusion splits into two, provided that (1) always applies. But the narrowing may be such that $R \gg r$ while the ends are far away, in which case (1) will apply not only for all r less than a certain critical value r^* (governed by a and by the position) but will actually become stronger as r decreases.

Precisely the same may occur for a dendrite (rod) surrounded by saturated solution; the only difference is that the signs of the curvatures are reversed, and hence also are the directions of the diffusion fluxes. This causes the dendrite to break up.

The breakup time can now be evaluated.

Conversion of an Inclusion

Figure 2 indicates the scale of the region within which diffusion is effective; l is several times a. The part between QQ' and PP' is of length about $2a$, and here the concentration changes from

$$\sim c_\infty\left(1-\frac{\sigma m}{\rho kTa}\right)$$

to

$$\sim c_\infty\left(1-\frac{\sigma m}{\rho kTr}\right),$$

where c_∞ is the concentration above a flat surface, σ is the surface tension, m is the mass of a molecule of the substance, ρ is the density of the solid, k is Boltzmann's constant, and T is absolute temperature. The density j of the diffusion flux is

$$j \sim \frac{Dc_\infty \sigma m}{2\rho kT}\left(\frac{1}{r}-\frac{1}{a}\right),$$

where D is the diffusion coefficient.

We assume that all the material entering through PP' and MM' is deposited between these points; then r as a function of time t is given by

$$\frac{dr}{dt} = \frac{Dc_\infty \sigma m}{\rho^2 kTal}\left(\frac{1}{a}-\frac{1}{r}\right).$$

The limits of integration for r are r_0 (radius of initial section) and zero; neglecting the change in a, the time τ needed is found as

$$\tau \sim \frac{\rho^2 kTa^2 l}{Dc_\infty \sigma m}\ln\frac{a}{a-r_0}. \tag{2}$$

This result is discussed below.

Conversion of a Dendrite

Breakage of a Large Dendrite. Figure 3 shows the shape of the weak point and the diffusion flows near it; here the diffusion occurs on the outside and so is governed mainly by the concentration at infinity, which we assume to be determined by remote dendrites of radius about a, which is

$$\sim c_\infty\left(1+\frac{\sigma m}{\rho kTa}\right).$$

The attack is most rapid where r is small (Fig. 3), so we consider only a spherically symmetrical solution to the steady-state diffusion equation. Then

$$j \sim \frac{Dc_\infty \sigma m}{\rho kTr}\left(\frac{1}{a}-\frac{1}{r}\right).$$

The material balance gives us, as before, that

$$\frac{dr}{dt} = \frac{j}{\rho} = \frac{Dc_\infty \sigma m}{\rho kTr}\left(\frac{1}{a}-\frac{1}{r}\right),$$

so

$$\tau \sim \frac{\rho^2 kTa^3}{Dc_\infty \sigma m}\left[-\ln\left(1-\frac{r_0}{a}\right)-\frac{r_0}{a}-\frac{1}{2}\left(\frac{r_0}{a}\right)^2\right]. \tag{3}$$

Detachment of a Branch. This is of especial interest as being the most common; it may be discussed, as above, by reference to Fig. 4, but here $r_0 \ll a$, so (3) simplifies to

$$\tau \sim \frac{\rho^2 kTr_0^3}{3Dc_\infty \sigma m}. \tag{4}$$

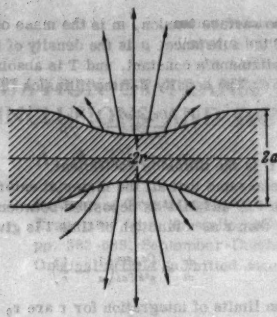

Fig. 3

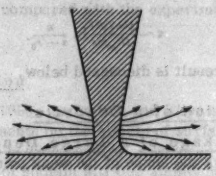

Fig. 4

Flat Dendrites. This case has no direct practical significance, but it reproduces the main features of the effects seen in Kliya's experimentally simpler system [3], in which ammonium chloride dendrites grew in the space between two glass slides. The detachment of branches was recorded by cinemicrography; $\tau = \tau(r_0)$ was measured. This case is discussed as above.

The concentration over the dissolving area is

$$c_\infty\left(1+\frac{\sigma m}{\rho kTr}\right).$$

The material is deposited on surfaces whose mean radius is about d, because radii larger than this are impossible for plates a distance 2d apart. These surfaces may lie at a distance $R \gg d$; diffusion is confined essentially to two dimensions, so

$$j \sim \frac{Dc_\infty \sigma m}{\rho kTr \ln\frac{r}{R}\left(\frac{1}{r}-\frac{1}{d}\right)},$$

$$\tau \sim \frac{\rho^2 kT}{Dc_\infty \sigma m}\int_0^{r_0} \frac{r^2 \ln\frac{R}{r}}{1-\frac{r}{d}}\,dr.$$

But $R \gg d$, $r_0 \leqslant d$, and the logarithm is a slowly varying function, so we have roughly

$$\tau \sim \frac{\rho^2 kT d^2}{Dc_\infty \sigma m}\left[-\ln\left(1-\frac{r_0}{d}\right)-\frac{r_0}{d}-\frac{1}{2}\left(\frac{r_0}{d}\right)^2\right]\ln\frac{R}{r_0}. \quad (5)$$

Discussion

Equations (2)-(5) all contain[1]

$$\frac{\rho^2 kT}{Dc_\infty \sigma m} \quad (6)$$

This shows that the conversion is accelerated at high concentrations and by large diffusion coefficients.

The quantities in (6) are functions of temperature, so τ may be found as a function of temperature. For example, c_∞ may increase rapidly, so the process accelerates toward high temperatures, especially if ρ decreases, as is usually the case.

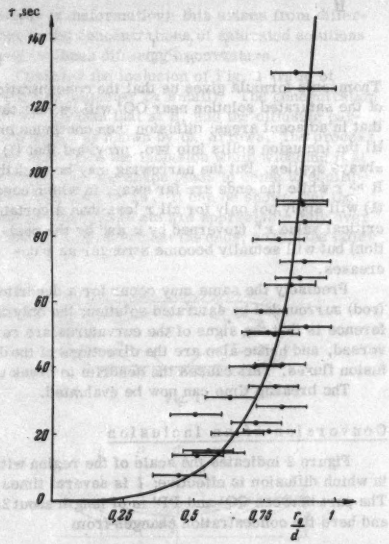

Fig. 5

[1] These expressions cannot be deduced by the method of dimensions, because the above result for τ is not the only combination of the quantities that has the dimensions of a time; but only D contains time, so we may put $\tau \sim 1/D$ directly.

Comparison of (2), (3), and (5) shows that the conversion time has a logarithmic singularity as r_0 tends to a or d, so the conversion is initially very slow if the initial deviation is small or if r_0 is comparable with the distance between the slides. Any narrow spot arising by accident will be leveled off if $r_0 \gg d$; it will not become narrower, and no breakage will occur.

Small r_0 (pronounced initial distortion) cause τ to vary in different ways with the initial radius: slightly for inclusions, in proportion to r_0^3 for bulky dendrites, and in proportion to $r_0^3 \ln r_0$ for flat dendrites.

Typical numerical values are $D \sim 10^{-5}$ cm^2 per sec; $\rho \sim 3$ g/cm^3; $\sigma \sim 3 \cdot 10^2$ dyn/cm^2; $m \sim 10^{-22}$ g; $c_\infty \sim 0.1$ g/cm^3; $T \sim 300°K$; $r_0 \sim 5 \cdot 10^{-4}$ cm; they give $\tau \approx 4$ min.

Figure 5 compares (5) (full line) with Kliya's [3] results (points), the coefficient of proportionality being chosen to given $R = 10d$.[2]

There are many instances where small crystals or cavities are altered in shape by surface tension in a calculable way; experiment here can provide reliable values for the surface tension as a function of crystallographic direction for such contacts.

We are indebted to G.G. Lemmlein for advice and assistance in this work.

LITERATURE CITED

1. G.G. Lemmlein, "Crack healing in crystals and shape change in secondary liquid inclusions," Dokl. Akad. Nauk SSSR, 78, 4, 685-688 (1951).
2. M.O. Kliya, "Some aspects of the formation of liquid inclusions in crystals," Dissertation [in Russian] (Institute of Crystallography, 1952).
3. M.O. Kliya, "The transformation mechanism of dendritic crystals," Kristallografiya, 1, 5, 576-581 (1956).

[2] The lines shown on the experimental points indicate the range of experimental error.

PREPARATION OF POTASSIUM TARTRATE CRYSTALS*

P. G. Pozdnyakov

Division 10, Ministry of the Radio and Electronics Industry

Translated from Kristallografiya, Vol. 1, No. 5,
pp. 589-593, September-October, 1956
Original article submitted April 4, 1956

A technique devised in 1947-1950 is described, which now forms the basis for the commercial production of these crystals.

These crystals (denoted in the industry by KT and those of ethylene-diamine tartrate (EDT) are used as piezoelectric plates of low temperature coefficient of frequency. KT is better than EDT in that its elastic constants vary less with temperature, and also because its electromechanical coupling coefficient is higher. This means that crystals of larger resonance range may be made. KT and EDT sometimes form good substitutes for quartz, e.g., in the filters of our 12-channel high-frequency telephones.

Mason [2] has described the properties of KT crystals in detail.

These crystals have not found commercial use in other countries, because of insuperable difficulties in routine production; EDT is used, in spite of the advantages of KT, because the crystals are much more readily grown [3].

There appears to be no published literature on the growth of KT crystals.

This salt ($K_2C_4H_4O_6{\cdot}\frac{1}{2}H_2O$) is made by neutralizing the acid or potassium hydrogen tartrate with caustic potash or potassium carbonate. The crystals are colorless and readily soluble in water, density 1.98 g/cm^3. The water of crystallization is very firmly bound; no effluorescence occurs even on prolonged exposure to temperatures up to 100°C, but the water is lost completely around 165 °C. The water is not lost under vacuum, so the material may be used in evacuated devices. The crystals have little tendency to take up water; they are unaffected by air of normal humidity, but deliquesce at or above 80% relative humidity.

The crystals are monoclinic (dihedral axial class); Fig. 1 illustrates one, the principal forms being the {100} and {001} pinakoids and the {11$\bar{1}$} and {1$\bar{1}$1} dihedra, with the {0$\bar{1}$0} monohedron also commonly present. The {020} monohedron is very rare; weak faces of the {101} and {10$\bar{1}$} pinakoids are also seen, with occasionally a few dihedral faces with high indices, such as {1$\bar{1}$3}.

The polarity along the diad axis (the b axis) is seen as a difference in growth rates along that axis. The angle of the monoclinic cell is 89°10'. There is prominent cleavage on {100} and {001} faces. Figure 2 shows a KT crystal of the usual habit grown from a point seed.

*Read at the First All-Union Conference on Piezoelectricity, November 24, 1952 [1].

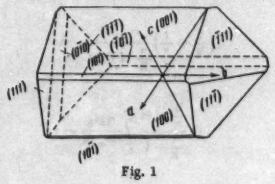

Fig. 1

Fig. 2

Aqueous KT is neutral; KT does not dissolve in alcohol or other organic solvents. The solubility in water is very nearly a linear function of temperature: 100 g of water at 25°C contains about 92 g, as against 108 g at 50°C. This high solubility means that a slight change in water content (e.g., by evaporation) can give rise to appreciable supersaturation. The solution is of low viscosity. High supersaturations do not occur, because the compound crystallizes spontaneously at supersaturations substantially lower than those found for EDT. This adds to the difficulty of growing KT crystals.

Slightly supersaturated solutions give crystals elongated along the b axis, the growth in the positive direction being the more rapid. The (020) face grows the most rapidly and is usually lost, followed by the $\{11\bar{1}\}$ dihedron. The $\{1\bar{1}1\}$ faces on the negative direction of the b axis grow at only half the rate of the $\{11\bar{1}\}$ faces, while the rates for the $\{100\}$ and $\{001\}$ faces are lower by factors of about three. These values are average ones, because temperature, supersaturation, etc., have some slight effect. Crystals grown from neutral solutions have very nearly the same habit as those grown from alkaline ones.

The temperature affects the habit by accelerating the growth of the $\{100\}$ and $\{001\}$ faces, so the crystals produced by hot solutions are more nearly isometric, while those from cold solutions are highly elongated along the b axis.

We began tests on the growth of KT crystals in 1947, but for a long time obtained unsatisfactory results with pure solutions; the pinakoids became coated with a cloudy layer when the crystals were 20–30 mm in size (sometimes earlier), and this retarded the growth. This was followed by a network of small cracks, which then extended. It seemed that traces of impurities were damaging the crystals, since good results were obtained only with certain batches of salt, and then only during the first and second cycles (on account of impurity buildup). Some tests were done on constant-temperature growth, but no consistent results were obtained.

It was clear that the crystals were very sensitive to traces of impurities, so various materials were added to the solution; alkali had been found to be of value with Rochelle salt and ammonium phosphate, as it appears to suppress the effects of some impurities. A solution that had failed to produce any satisfactory crystals was treated with 50 g of KOH per liter; the very first run gave perfect crystals, and further tests with these solutions containing much KOH showed that the cloudiness and cracking in the pinakoids were completely suppressed.

Ammonia had the same effect as KOH, but KOH was preferred, because this had less tendency to alter in concentration with lapse of time. Poor results were obtained with solutions containing NaOH, which reduced the growth rates of many faces, especially $\{11\bar{1}\}$, and gave rise to cloudy films.

The alkaline solutions were more stable than the neutral ones, and they allowed higher supersaturations, and hence higher growth rates; the maximum supercooling without spontaneous crystallization or production of defective crystals was about two degrees. Growth rates of 5 mm/day on the b axis are possible with these KOH solutions.

Long-term production of these crystals has shown that the best KOH is 15–25 g per liter of solution, because the KOH tends to reduce the solubility of the tartrate: 100 g of water at 25°C dissolves about 85 g when the KOH content is 15 g per liter, and about 100 g at 60°C.

Our first tests were done with point seeds of various orientations, but the best results were obtained with seeds elongated along the b axis with the fast-growing end facing outward; as would be expected. Unfortunately, the shape of the resulting crystals was unsatisfactory for cutting, on account of the excessive elongation and small area of the $\{100\}$ faces. Filter crystals should either be of large cross section or have broad $\{100\}$ faces. The first type may be produced satisfactorily from broad seed plates cut parallel to $(11\bar{1})$ or (020) faces, but the method has the disadvantage that the large area hinders regeneration. It is better to use rod seeds of much smaller area, and these allow one to produce crystals of large cross section in the two most useful styles. The first style has the length of the rod parallel to the edge between the $(11\bar{1})$ and $(\bar{1}11)$ faces, which is analogous to the use of rods with ammonium phosphate, which are cut parallel to the intersection of adjacent faces of the dipyramid [4]. Square KT crystals of large cross section are produced. The second style is a rod parallel to the intersection of the $(11\bar{1})$ and (100) faces, which is held with the face of the $(11\bar{1})$ dihedron upwards. This gives large broad crystals whose cross section is a parallelogram elongated along the c axis. These crystals are the best, because their $\{100\}$ faces are very prominent [5]. Figure 3 shows the best orientation of the rod seed and a crystal grown from such a seed. Figure 4 shows a homogeneous crystal of weight about 900 g, which was grown from a seed 3–4 mm high, 2 mm wide, and 50–60 mm long. Stepped intergrowths are usually produced if the length of the seed deviates by more than 2° from the intersection between (100) and $(11\bar{1})$ faces. This tendency increases with

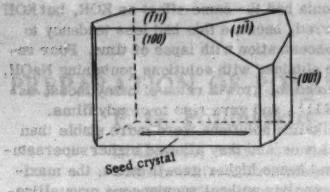

Fig. 3

the length of the seed, so long seeds must be carefully checked for orientation. The upper and lower faces must also be very smooth; grooves or recesses can give rise to intergrowths. The seeds must also be free from internal defects, because these may give rise to cracks.

Vigorous stirring or movement of the crystal is essential to the production of homogeneous crystals; continuous circular motion of the crystal gives satisfactory results, but the growth rate should then be kept low, because the solution tends to stagnate on some faces. Reciprocating motion is better, e.g., rotation through 60-90° at 20-30 cycles per minute.

Routine production is based on cooling solutions saturated at 45-50°. The temperature coefficient of the solubility is not large, so the method requires a large ratio of solution volume to weight of finished crystal; a liter of solution saturated at 50°C yields only 100-125 g of crystal on cooling to room temperature. Crystals grown by cooling from higher temperatures have considerable internal stress, so they often crack.

The initial supercooling should not exceed 1°C; 0.6-0.8°C is most usual. The crystals are sensitive to the supersaturation, so particular attention must be given to the sealing of the apparatus, otherwise loss of evaporation may produce excessive supersaturation and hence damage to the crystals.

A supersaturation sufficient to produce a growth rate of 5 mm/day has a marked tendency to cause spontaneous crystallization; the most economic rate for routine production is 3-4 mm/day.

The crystallizers we have developed have been described [6, 7]. A single crystallizer will produce 9-10 crystals each of weight about 500 g in a 20-day cycle. Crystals of weight over 1 kg are readily grown merely by using less seeds in the crystallizer.

Fig. 4

LITERATURE CITED

1. Élektrichestvo, No. 6 (1953).
2. W. Mason, The Properties of Monoclinic Crystals [Russian translation] (IL, 1946), p. 705.
3. W. Mason, Piezoelectric Crystals and Their Application in Ultrasonics [Russian translation] (IL, 1952), p. 168.
4. P. G. Pozdnyakov and A. S. Shternberg, Author's Certificate No. 100,988, dated January 7, 1952 [see Byull. Izobretenii No. 6, 7 (1955)].
5. P. G. Pozdnyakov and A. S. Shternberg, Author's Certificate No. 101,189, dated July 3, 1952 [see Byull. Izobretenii, No. 8, 7 (1955)].
6. P. G. Pozdnyakov, Author's Certificate No. 100,842, dated November 20, 1951 [see Byull. Izobretenii, No. 6, 7 (1955)].
7. P. G. Pozdnyakov, "Apparatus for growing crystals. Exchange of experience," Collection No. 5, Izd. NII MRTP, 1955, p. 43.

BRIEF COMMUNICATIONS

SYMMETRY OF PATTERSON SYNTHESES (FUNCTIONS)

N. I. Shulepova and N. V. Belov

Lobachevskii University, Gor'kii

Translated from Kristallografiya, Vol. 1, No. 5,
pp. 594-595, September-October, 1956
Original article submitted July 13, 1956

The 24 groups of three-dimensional Patterson syntheses were first derived in graduate work by N.I. Shulepova at Gor'kii University in 1949, but the work was not published. Buerger [1] published a derivation in 1950, but with the omission of one group, which he corrected in the same year [2]. In 1950 also, Kitaigorodskii [3] repeated Buerger's error and listed only 23 groups.

In 1953, Lipson and Cochran [4] published the astonishing statement that the two-dimensional Patterson groups are derived from the 17 ordinary ones by the addition of a center of symmetry.

All possible misunderstandings are removed if we define the Patterson groups as the product of the 11 Laue classes by the 14 Bravais lattices subject to the condition (and this is where Buerger and Kitaigorodskii erred) that Laue class 3m may be oriented in two ways with respect to the hexagonal (primitive) lattice: the mirror planes may be perpendicular to the shortest edges of the cell or parallel to them. The complete list of the Patterson groups is then as follows:

Laue classes	Patterson groups
I. 1	1. $P\bar{1}$
II. 2/*m*	2. *P*2/*m* 3. *C*2/*m*
III. *mmm*	4. *Pmmm* 5. *Cmmm* 6. *Fmmm* 7. *Immm*
IV. 4/*m*	8. *P*4/*m* 9. *I*4/*m*
V. 4/*mmm*	10. *P*4/*mmm* 11. *I*4/*mmm*
VI. $\bar{3}$	12. *P*$\bar{3}$ 13. *R*$\bar{3}$
VII. $\bar{3}m$	14. *P*$\bar{3}$*m*1 15. *P*$\bar{3}$1*m* 16. *R*$\bar{3}$*m*
VIII. 6/*m*	17. *P*6/*m*
IX. 6/*mmm*	18. *P*6/*mmm*
X. *m*3	19. *Pm*3 20. *Fm*3 21. *Im*3
XI. *m*3*m*	22. *Pm*3*m* 23. *Fm*3*m* 24. *Im*3*m*

The same result is obtained if we say that the Patterson groups are the symmorphic space groups corresponding to the 11 Laue classes.

The 7 two-dimensional Patterson groups are found in the same way:

I. 2	1. *p*2
II. *mm*2	2. *pmm*2 3. *cmm*2
III. 4	4. *p*4
IV. 4*mm*	5. *p*4*mm*
V. 6	6. *p*6
VI. 6*mm*	7. *p*6*mm*

LITERATURE CITED

1. M. J. Buerger, "Vector sets," Acta Cryst., 3, 87-97 (1950).
2. M. J. Buerger, "Vector sets. A correction," Acta Cryst., 3, 243 (1950).
3. A.I. Kitaigorodskii, X-Ray Structure Analysis [in Russian] (Moscow, 1951).
4. H. Lipson and W. Cochran, The Determination of Crystal Structures (London, 1953).

IONIC RADII AND REFRACTIONS FOR GROUP VIII METALS

S. S. Batsanov and E. D. Ruchkin

M. V. Lomonosov State University, Moscow

Translated from Kristallografiya, Vol. 1, No. 5, pp. 595-596, September-October, 1956
Original article submitted April 20, 1956

The ionic refractions are given here for group VIIIa elements in their various states of ionization.

The refractions have been calculated by Kordes' method from the ionic radii.

It has been shown [2] that the ionic radius may be calculated from the electronegativity E of the atom, which Sanderson [3] gives as $E = Z/(\frac{4}{3}\pi E_i \cdot r^3)$, where Z is the number of electrons, E_i is the electron density of an inert-gas atom with the same number of electrons, and r is the covalent radius.

The covalent radius is dependent on the valency for group VIII metals, so the atomic E of group VIII metals cannot be based on the usual covalent radii. This difficulty can be avoided if we calculate the covalent radii from the atomic radii [4], because the metallic and covalent bonds are essentially similar in nature, the differences being due to change in the coordination number (12 for metallic bonds, 6 for covalent bonds in these elements).

Table 1 gives the covalent radii (from the atomic ones, with correction for the coordination number), the electron densities for isoelectronic inert-gas atoms, and the atomic and ionic E. The last are given by Sanderson's formula $\Delta E = 2.08n \cdot (E_{at})^{1/2}$, where ΔE is the change in E when the atom loses n electrons.

TABLE 1

Element	r	E_i	E_{at}	E for ion		
				+2	+3	+4
Fe	1.21	1.02	3.43	11.13	14.98	—
Co	1.20	1.04	3.59	11.47	15.41	—
Ni	1.19	1.06	3.74	11.79	15.80	19.87
Ru	1.28	1.33	3.77	11.84	15.87	19.91
Rh	1.28	1.34	3.82	11.95	16.01	20.08
Pd	1.31	1.35	3.61	11.51	—	19.41
Os	1.29	1.63	5.18	14.64	19.37	24.10
Ir	1.29	1.64	5.22	14.72	19.47	24.22
Pt	1.32	1.65	4.90	14.11	—	23.32

TABLE 2

Element	Degree of ionization					
	+2		+3		+4	
	E_i	r	E_i	r	E_i	r
Fe	0.97	0.81	0.94	0.73	—	—
Co	0.99	0.80_5	0.97	0.72_5	—	—
Ni	1.02	0.80	0.99	0.72_5	0.97	0.66_5
Ru	1.32	0.86	1.31	0.78	1.30	0.71_5
Rh	1.32	0.86_5	1.32	0.78	1.31	0.72
Pd	1.33	0.88	—	—	1.32	0.73
Os	1.61	0.91	1.60	0.82_5	1.59	0.76_5
Ir	1.62	0.91	1.61	0.82_5	1.60	0.76_5
Pt	1.63	0.92_5	—	—	1.61	0.78

TABLE 3

Element	Degree of ionization		
	+2	+3	+4
Fe	1.14	1.13	—
Co	1.11	1.09	—
Ni	1.08	1.06	1.03
Ru	1.37	1.33	1.20
Rh	1.41	1.33	1.23
Pd	1.52	—	1.31
Os	1.57	1.41	1.28
Ir	1.57	1.41	1.28
Pt	1.69	—	1.39

The ionic E then give the ionic radii in group VIIIa as

$$r = \sqrt{\frac{|Z|}{\frac{4}{3}\pi \cdot E_i \cdot E_{ion}}}$$

Table 2 gives E_i for Me^{2+}, Me^{3+}, and Me^{4+}, together with the radii.

These ionic radii have been compared with those given by Bokii [4], Ahrens [5], and Stockar [9].

The calculated radii lie within the limits of variation of the radii given by these various sources.

Table 3 gives the ionic refractions calculated from Kordes' formula $R = 1.354(r \cdot Z^2/(n-1))^{4.5}$, where r is ionic radius, Z is valency, and n is the Born repulsion factor.

These results agree closely with the empirical values $R_{Fe^{2+}} = 1.15$ cm^3, $R_{Co^{2+}} = 0.7$ cm^3, and $R_{Ni^{2+}} = 0.6$ cm^3, the mean deviation not exceeding 0.3 cm^3, which does not exceed the spread of the experimental results for the ionic refractions of the first triad of metals in group VIII.

LITERATURE CITED

1. E. Kordes, "Ermittlung von Atomabständen aus der Lichtbrechung," Z. Phys. Chem., 44, 249-261 (1939).
2. S.S. Batsanov, "Calculation of the electronic polarizability for atoms," Zh. Fiz. Khim., 30, No. 12 (1956).
3. R. Sanderson, "Electronegativities in inorganic chemistry," J. Chem. Educat., 32, 140-143 (1955).
4. G.B. Bokii, Introduction to Chemical Crystallography [in Russian] (1953).
5. L. Ahrens, "The use of ionization potentials," Geochim. Cosmochim. Acta, 2, 155-169 (1952).
6. K. Stockar, "Radii of positive monoatomic ions," Helv. Chim. Acta, 33, 1409-1420 (1950).

THERMAL STRESSES IN CUBIC CRYSTALS

B. N. Grechushnikov and D. Brodovskii

Institute of Crystallography, Academy of Sciences of the USSR
Translated from Kristallografiya, Vol. 1, No. 5,
pp. 597-599, September-October, 1956
Original article submitted September 15, 1955

1. It has been shown [1] that the thermoelastic stresses in anisotropic bodies are very important to the theory of annealing.

Here we consider this for a very simple particular case in two dimensions, with allowance for temperature terms. Here, the components u, v, w of the displacement vector are dependent only on the variables x and y, with $u = u(x, y)$, $v = v(x, y)$, $w = 0$, which gives us the components of the deformation tensor as

$$\varepsilon_x = \frac{\partial u}{\partial x},\quad \varepsilon_y = \frac{\partial v}{\partial y},\quad \gamma_{xy} = \frac{\partial u}{\partial x} + \frac{\partial v}{\partial y},\quad \varepsilon_z = \gamma_{yz} = \gamma_{xz} = 0. \tag{1}$$

Hooke's law, as extended via the thermal-expansion tensor α_{ik}, is put as

$$\begin{aligned}
\varepsilon_x &= a_{11}\sigma_x + a_{12}\sigma_y + a_{13}\sigma_z + a_{16}\tau_{xy} + \alpha_{11}T,\\
\varepsilon_y &= a_{12}\sigma_x + a_{22}\sigma_y + a_{23}\sigma_z + a_{26}\tau_{xy} + \alpha_{22}T,\\
\varepsilon_z &= a_{13}\sigma_x + a_{23}\sigma_y + a_{33}\sigma_z + a_{36}\tau_{xy} + \alpha_{33}T,\\
\gamma_{xy} &= a_{16}\sigma_x + a_{26}\sigma_y + a_{36}\sigma_z + a_{66}\tau_{xy} + \alpha_{12}T.
\end{aligned}$$

Then (see [2]):

$$\begin{aligned}
\varepsilon_x &= \beta_{11}\sigma_x + \beta_{12}\sigma_y + \beta_{16}\tau_{xy} + \gamma_{11}T,\\
\varepsilon_y &= \beta_{12}\sigma_x + \beta_{22}\sigma_y + \beta_{26}\tau_{xy} + \gamma_{22}T,\\
\gamma_{xy} &= \beta_{16}\sigma_x + \beta_{26}\sigma_y + \beta_{66}\tau_{xy} + \gamma_{12}T,
\end{aligned} \tag{2}$$

$$\sigma_z = -\frac{1}{a_{33}}(a_{13}\sigma_x + a_{23}\sigma_y + a_{36}\tau_{xy} + \alpha_{33}T). \tag{3}$$

Here, $\beta_{ij} = a_{ij} - a_{i3}\alpha_{33}/a_{33}$ (i, j = 1, 2, 6)

$$\gamma_{11} = \alpha_{11} - \frac{a_{13}\alpha_{33}}{a_{33}},\quad \gamma_{22} = \alpha_{22} - \frac{a_{23}\alpha_{33}}{a_{33}},\quad \gamma_{12} = \alpha_{12} - \frac{a_{36}\alpha_{33}}{a_{33}}. \tag{4}$$

The equations of equilibrium and for the boundary conditions are as in the theory of elasticity without the temperature-dependent terms (we assume that external forces are absent):

$$\begin{aligned}
&\frac{\partial \sigma_x}{\partial x} + \frac{\partial \tau_{xy}}{\partial y} = 0,\\
&\frac{\partial \sigma_y}{\partial y} + \frac{\partial \tau_{xy}}{\partial x} = 0,
\end{aligned} \tag{5}$$

$$\begin{aligned}
&\sigma_x \cos(nx) + \tau_{xy}\cos(ny) = 0,\\
&\tau_{xy}\cos(nx) + \sigma_y \cos(ny) = 0.
\end{aligned} \tag{6}$$

Compatibility of the deformations requires that

$$\frac{\partial^2 \varepsilon_x}{\partial y^2} + \frac{\partial^2 \varepsilon_y}{\partial x^2} = \frac{\partial \gamma_{xy}}{\partial x\,\partial y},$$

and this, with (2), becomes

$$\begin{aligned}
&\beta_{11}\frac{\partial^2 \sigma_x}{\partial y^2} + \beta_{12}\frac{\partial^2 \sigma_y}{\partial y^2} + \beta_{16}\frac{\partial^2 \tau_{xy}}{\partial y^2} + \gamma_{11}\frac{\partial^2 T}{\partial y^2} + \beta_{12}\frac{\partial^2 \sigma_x}{\partial x^2} + \beta_{26}\frac{\partial^2 \tau_{xy}}{\partial x^2}\\
&+ \gamma_{22}\frac{\partial^2 T}{\partial x^2} - \beta_{16}\frac{\partial^2 \sigma_x}{\partial x\,\partial y} - \beta_{26}\frac{\partial^2 \sigma_y}{\partial x\,\partial y} - \beta_{66}\frac{\partial^2 \tau_{xy}}{\partial x\,\partial y} - \gamma_{12}\frac{\partial^2 T}{\partial x\,\partial y} = 0.
\end{aligned} \tag{7}$$

The substitutions $\overset{*}{\sigma}_x = \sigma_x - c_{11}T$, $\overset{*}{\sigma}_y = \sigma_y - c_{22}T$, $\overset{*}{\tau}_{xy} = \tau_{xy} - c_{12}T$, in which c_{11}, c_{22}, and c_{12} satisfy

$$\begin{aligned}
\gamma_{11} &= \beta_{11}c_{11} + \beta_{12}c_{22} + \beta_{16}c_{12},\\
\gamma_{12} &= \beta_{16}c_{11} + \beta_{26}c_{22} + \beta_{66}c_{12},\\
\gamma_{22} &= \beta_{12}c_{11} + \beta_{22}c_{22} + \beta_{26}c_{12},
\end{aligned}$$

enable us to reduce the problem to the ordinary one of the stress distribution in a body subject to bulk and surface forces whose components are

$$\begin{aligned}
X &= -c_{11}\frac{\partial T}{\partial x} - c_{12}\frac{\partial T}{\partial y},\\
Y &= c_{12}\frac{\partial T}{\partial x} - c_{22}\frac{\partial T}{\partial y},\\
X_n &= c_{11}T\cos(nx) + c_{12}T\cos(ny),\\
Y_n &= c_{12}T\cos(nx) + c_{22}T\cos(ny).
\end{aligned}$$

2. Consider the stress in a long cylinder of radius R cut from a cubic crystal along a cube edge. The result is to be applied in annealing theory, so we assume that the sides of the cylinder are heated or cooled at a constant rate ±h. The temperature T within the cylinder is given by [3]

$$T = ht - \frac{h}{4\chi}(R^2 - x^2 - y^2) \tag{8}$$

in which t is time and $\varkappa$ is thermal conductivity.

The coordinate system has its Z axis along the axis of the cylinder, the X and Y axes being in the plane of the cross section; then the tensor for the elastic constants simplifies to give [4]

$$a_1 = a_{11} = a_{22} = a_{33},\ a_2 = a_{12} = a_{13} = a_{23},$$
$$a_{14} = a_{24} = a_{34} = 0,\ a_{44} = a_3.$$

We seek a solution to (5) subject to (6) and (7) in the form

$$\begin{aligned} \sigma_x &= A(x^2 + 3y^2 - R^2), \\ \sigma_y &= A(3x^2 + y^2 - R^2), \\ \tau_{xy} &= -2Axy. \end{aligned} \tag{9}$$

It can be shown that this choice is such as to satisfy the equation of equilibrium and the boundary conditions, A being given by (7) as

$$A = \frac{\alpha h}{2\varkappa} \frac{a_1 - a_2}{6(a_1^2 - a_2^2) + 2(a_1 a_2 - a_2^2) + a_3}.$$

The solution implies stresses σ_z given by (3) as

$$\sigma_z = -\frac{2Aa_2}{a_1}(2r^2 - R^2) + \frac{\alpha h}{2\varkappa a_1}(R^2 - r^2),$$
$$r^2 = x^2 + y^2.$$

In addition, we must have $\sigma_z = 0$ at $z = \pm H/2$, in which H is the length of the cylinder, if the result is to be applicable to a finite cylinder with free ends; but σ_z is not dependent on z, so this condition cannot be satisfied. The principle [5] allows us to proceed as follows, however. We replace the stresses by the equivalent force and apply to the base of the cylinder a force equal in magnitude but opposite in direction to the above force. The state of stress in simple tension or compression is not dependent on the elastic properties [6], so σ_x, σ_y, and τ_{xy} are unaltered, while for $\bar{\sigma}_z$ we have

$$\bar{\sigma}_z = (2r^2 - R^2)\left[\frac{2Aa_2}{a_1} - \frac{\alpha h}{2\varkappa a_1}\right].$$

The radial and transverse components of the stress are

$$\begin{aligned} \sigma_r &= A(r^2 - R^2), \\ \sigma_\theta &= A(3r^2 - R^2), \\ \tau_{r\theta} &= 0. \end{aligned}$$

The standard result is obtained automatically for an isotropic cylinder.

We are indebted to V.R. Regel' for proposing the topic and for direction of the work.

LITERATURE CITED

1. G.E. Tomilovskii, "An experimental study of the effects of structural inhomogeneity, surface state, and heat treatment on the strength of synthetic corundum crystals," Dissertation [in Russian] (Institute of Crystallography, 1953).
2. S.G. Lekhnitskii, Anisotropic Plates [in Russian] (1947).
3. H. Adams and E.D. Williamson, "Temperature distribution in solids during heating or cooling," Phys. Rev., 14, 99-114 (1919).
4. A.V. Shubnikov, E.E. Flint, and G.B. Bokii, The Principles of Crystallography [in Russian] (1940).
5. N.I. Muskhelishvilli, Some Major Problems in the Mathematical Theory of Elasticity [in Russian] (1954).
6. S.G. Lekhnitskii, Theory of Elasticity for Anisotropic Bodies [in Russian] (1950).
7. S.P. Timoshenko, The Theory of Elasticity [in Russian] (1937).

THERMOELASTIC STRESSES IN ANISOTROPIC PLATES

V. L. Indenbom, I. M. Sil'vestrova, and Yu. I. Sirotin

Institute of Crystallography, Academy of Sciences of the USSR; and M. V. Lomonosov State University, Moscow

Translated from Kristallografiya, Vol. 1, No. 5, pp. 599-603, September-October, 1956
Original article submitted April 23, 1956

These stresses often arise in technical applications of crystals, and they have a major influence on the choice of growth and annealing conditions, as well as on the thermal stability in pyroelectric and piezoelectric devices. This makes it of interest to deduce the stresses produced in such plates by nonuniform temperature distributions.[1]

The plate is taken to be cut in any way from the crystal; with it we associate a Cartesian coordinate system whose origin lies in the central plane and whose Z axis is normal to the surface. The temperature distribution is $\theta = \theta(z)$, but otherwise it is entirely arbitrary.

In terms of the components of the stress tensor, the equation for equilibrium is

$$\frac{\partial \sigma_{kz}}{\partial z} = 0 \quad (k = 1, 2, 3) \tag{1}$$

with $\sigma_{kz} = 0$ at the surface (no external forces); this gives

$$\sigma_{kz} = 0 \quad (k = 1, 2, 3) \tag{2}$$

for all points.

The stresses and bending moments averaged over the thickness are zero at the edges:

$$\bar{\sigma}_{ij} = 0, \ \overline{z\sigma}_{ij} = 0, \ (i, j = 1, 2). \tag{3}$$

The bar in (3) denotes averaging over the thickness in the usual way:

$$\bar{\sigma}_{ij} = \frac{1}{2a}\int_{-a}^{+a} \sigma_{ij}(z)\, dz, \text{ etc.},$$

in which a is half the thickness.

The solution is a function of z alone, so (3) is satisfied throughout the plate.

Hooke's law in generalized form[2] gives

$$\varepsilon_{ij} = s_{ijkl}\,\sigma_{kl} + \alpha_{ij}\theta. \tag{4}$$

and with (3) we have

$$\bar{\varepsilon}_{ij} = \alpha_{ij}\bar{\theta}, \ \overline{z\varepsilon}_{ij} = \alpha_{ij}\overline{z\theta} \quad (i, j = 1, 2). \tag{5}$$

Only three of the compatibility equations are not satisfied identically:

$$\frac{\partial^2 \varepsilon_{ij}}{\partial z^2} = 0 \quad (i, j = 1, 2). \tag{6}$$

From (5), we have the solution to (6) as

$$\varepsilon_{ij} = \alpha_{ij}\left(\frac{3}{a^3}\overline{z\theta}\cdot z + \bar{\theta}\right) \quad (i, j = 1, 2), \tag{7}$$

which gives us a system of linear equations for the stresses:

$$s_{ijkl}\,\sigma_{kl} = \alpha_{ij}\left(\frac{3}{a^3}\overline{z\theta}\cdot z + \bar{\theta} - \theta\right) \quad (i, j = 1, 2). \tag{8}$$

The solution to (8) may be put as

$$\sigma_{ik} = \beta_{ik}\left(\frac{3}{a^3}\overline{z\theta}\cdot z + \bar{\theta} - \theta\right) \quad (i, j = 1, 2), \tag{9}$$

in which the thermoelastic coefficients β_{ik} are as follows, if we use the ordinary rules [2] for converting the subscripts:

$$\beta_{mn} = \frac{A_{mn}}{\Delta}\alpha_n \quad (m, n = 1, 2, 6). \tag{10}$$

[1] No thermoelastic stresses are produced by uniform distributions, or ones linearly dependent on the rectilinear coordinates, as for an isotropic body [1].

[2] Here and henceforth we assume summation with respect to the subscripts as appropriate.

TABLE 1. Thermoelastic Coefficients for Crystal Plates

System	Axis X	Axis Y	Axis Z
Monoclinic	$\beta_{yy} = A_1(s_{22}\alpha_2 - s_{23}\alpha_3)$ $\beta_{zz} = A_1(-s_{23}\alpha_2 + s_{33}\alpha_3)$ $\beta_{yz} = 0$ $A_1^{-1} = s_{22}s_{33} - s_{23}^2$	$\beta_{xx} = A_2[(s_{23}s_{45} - s_{36}^2)\alpha_1 + (s_{11}s_{35} - s_{13}s_{45})\alpha_3 + (s_{13}s_{36} - s_{11}s_{23})\alpha_2]$ $\beta_{zz} = A_2[(s_{13}s_{36} - s_{12}s_{33})\alpha_1 + (s_{11}s_{36} - s_{13}^2)\alpha_3 + (-s_{11}s_{23} + s_{13}s_{12})\alpha_2]$ $\beta_{xz} = A_2[(s_{12}s_{36} - s_{13}s_{23})\alpha_1 + (s_{13}s_{13} - s_{11}s_{33})\alpha_3 + (s_{11}s_{23} - s_{12}^2)\alpha_2]$ $A_2^{-1} = s_{11}s_{23}s_{45} + 2s_{13}s_{12}s_{36} - s_{23}s_{36}^2 - s_{11}s_{36}^2 - s_{45}s_{12}^2$	$\beta_{xx} = A_3(s_{22}\alpha_1 - s_{12}\alpha_2)$ $\beta_{yy} = A_3(-s_{12}\alpha_1 + s_{11}\alpha_2)$ $\beta_{xy} = 0$; $A_3^{-1} = s_{11}s_{22} - s_{12}^2$
Orthorhombic		$\beta_{xx} = A_4(s_{23}\alpha_1 - s_{13}\alpha_2)$ $\quad \beta_{xz} = 0$ $\beta_{zz} = A_4(-s_{13}\alpha_1 + s_{11}\alpha_2)$ $\quad A_4^{-1} = s_{11}s_{33} - s_{13}^2$	
Trigonal	$\beta_{yy} = A_5(s_{23}s_{44}\alpha_1 - s_{13}s_{44}\alpha_2)$ $\beta_{zz} = A_5[-s_{13}s_{44}\alpha_1 + (s_{33}s_{44} - s_{14}^2)\alpha_2]$ $\beta_{yz} = A_5(-s_{14}s_{23}\alpha_1 + s_{14}s_{13}\alpha_2)$ $A_5^{-1} = -s_{14}^2 s_{33} + s_{44}(s_{11}s_{33} - s_{13}^2)$	$\beta_{xx} = A_6(s_{23}s_{55}\alpha_1 - s_{13}s_{55}\alpha_3)$ $\beta_{zz} = A_6[-s_{13}s_{55}\alpha_1 + (s_{11}s_{55} + s_{13}^2)\alpha_3]$ for classes 3, $\bar{6}$ $\beta_{xz} = A_6(-s_{13}s_{23}\alpha_1 + s_{13}s_{13}\alpha_3)$ $A_6^{-1} = s_{55}(s_{11}s_{33} - s_{13}^2) - s_{13}^2 s_{23}$ $\beta_{xx} = A_7(s_{23}\alpha_1 - s_{13}\alpha_2)$ $\beta_{zz} = A_7(-s_{13}\alpha_1 + s_{11}\alpha_2)$ for classes 3:2; 3·m, 3:m $\beta_{xz} = 0$; $A_7^{-1} = s_{11}s_{33} - s_{13}^2$	$\beta_{xx} = \beta_{yy} = \alpha_3(s_{11} + s_{12})^{-1}$ $\beta_{xy} = 0$
Tetragonal and hexagonal	As for a monoclinic plate normal to the X axis Here, $s_{11} = s_{22}$; $s_{13} = s_{23}$; $\alpha_1 = \alpha_2$	As for an orthorhombic plate normal to the Y axis	As for a trigonal plate normal to the Z axis
Cubic	As for a trigonal plate normal to the Z axis		

Here,

$$\Delta = \begin{vmatrix} s_{11} & s_{12} & s_{16} \\ s_{12} & s_{22} & s_{26} \\ s_{16} & s_{26} & s_{66} \end{vmatrix}$$

and A_{mn} is the algebraic complement of element s_{mn} in Δ. We have $\overline{z\theta} = 0$ for the special case of a distribution symmetrical about the mean plane, and

$$\sigma_{ik} = \beta_{ik}(\bar{\theta} - \theta). \tag{11}$$

Table 1 gives formulas for the β_{ik} for plates cut normal to the physics axes in terms of the usual settings[3] of the crystals.

For instance, for ethylenediamine tartrate,[4] a monoclinic crystal widely used in piezoelectric devices, we have for plates cut perpendicular to the X, Y, and Z axes (in dynes/cm^2 · deg),[5]

$\beta_{yy} = 1.05 \cdot 10^7$. $\beta_{xx} = 0.63 \cdot 10^7$. $\beta_{xz} = 0.05 \cdot 10^7$.
$\beta_{zz} = 0.99 \cdot 10^7$. $\beta_{zz} = 0.7 \cdot 10^7$. $\beta_{yy} = 0.56 \cdot 10^7$.
$\beta_{yz} = 0$. $\beta_{zx} = 0.16 \cdot 10^7$. $\beta_{xy} = 0$.

The stress ellipse degenerates to a circle for a plate cut normal to an axis of order three or higher, as would be expected.

This case is closely similar to that for an isotropic plate having forces parallel to the surface and equal [5] to

$$\sigma = \beta\left(\frac{3}{a^2}\overline{z\theta} \cdot z + \bar{\theta} - \theta\right), \tag{12}$$

where

$$\beta = \frac{\alpha E}{1 - \mu}.$$

E being Young's modulus and μ Poisson's ratio.

Formula (12) is the common basis of calculations on heating and cooling [6], annealing [5], quenching [7], and thermal stability [8] for isotropic plates, so (9)-(11) enable us to calculate these effects for any crystalline plate. Of course, allowance must be made for the anisotropy in the thermal conductivity [9]; the heat transfer will be governed by the conductivity normal to the surface.

All the above formulas are applicable to any plate with rectilinear [10] anisotropy, not merely to crystal plates.

LITERATURE CITED

1. V.M. Maizel', Temperature in the Theory of Elasticity [in Russian] (1951).
2. W. Mason, Piezoelectric Crystals and Their Application in Ultrasonics [Russian translation] (1952).
3. A.V. Shubnikov, E.E. Flint, and G.B. Bokii, The Principles of Crystallography [in Russian] (1940).
4. R. Bechmann, "Determination of elastic and piezoelectric coefficients of monoclinic crystals with particular reference to ethylene diamine tartrate," Proc. Phys. Soc., 63, 577 (1950).
5. L.H. Adams and E.D. Williamson, "Annealing of glass," J. Frankl. Inst., 190, 597, 835 (1920).
6. N. Yu. Taits, Techniques in Heating Steel [in Russian] (1950).
7. V.L. Indenbom, "Theory of the tempering of glass," Zh. Tekhn. Fiz., 24, 925 (1954).
8. Glass Technology (collection edited by A. I. Kitaigorodskii) [in Russian] (1951).
9. I.V. Mitskevich, "Some aspects of thermal conduction in anisotropic solids," Zh. Éksperim. i Teor. Fiz., 26, 557 (1954).
10. S.G. Lekhnitskii, Theory of Elasticity for Anisotropic Bodies [in Russian] (1950).

[3] See [3], p. 93, or [2], p. 50.

[4] The elastic coefficients of [4] have been used together with the expansion coefficients given on p. 16 of [2].

[5] The thermoelastic stress may vary by a factor of 10-20 with the orientation of the plate, other conditions being unchanged.

RESONANT PLATES CUT FROM BRAZILIAN-LAW QUARTZ TWINS

M. I. Yaroslavskii and I. G. Vasin

Institute of Crystallography, Academy of Sciences of the USSR
Translated from Kristallografiya, Vol. 1, No. 5,
pp. 603-606, September-October, 1956
Original article submitted July 11, 1956

Natural quartz crystals are usually twinned, the dauphiné and Brazilian laws being the most common, one or another of which accounts for a large part of almost any natural crystal.

A Brazilian (optical) twin consists of right- and left-handed parts in antiparallel positions, the positive rhombohedron of the right-handed part being intergrown with the same of the left; the same applies to the negative rhombohedra.

The symmetry of such a twin, if ideal, is $6 \cdot m$, which is higher than that of quartz itself. An ideal Brazilian twin shows no piezoelectric response, because all the piezoelectric moduli for this class are zero [1]; plates cut from such crystals thus find no piezoelectric applications.

A feature commonly overlooked is that the elastic-constants tensor for such a twin, $\{s_{iklm}\}$, is exactly analogous with the tensor for a single crystal of quartz, which has 3:2 symmetry. Thus, the mechanical modes of a plate cut from a twin will be as for such a crystal; in particular, the resonant frequencies and temperature coefficients of these will be the same [2].

Brazilian twins commonly occur as polysynthetic intergrowths (alternating thin layers of the two forms); the two components frequently differ very much in size, so such an intergrowth contains areas in which the twinned parts are small, although the size of such areas may be inadequate to allow the cutting of truly single-crystal plates of the required size.

It will be clear from the above that such a twinned crystal may be cut into resonant plates whose properties are precisely as for single-crystal ones; this is possible if the twins lie in a part of the plate not covered by the metal electrodes. This is often so, because most quartz plates are nowadays only partly metallized; in particular, the electrodes of high-frequency plates of AT and BT cuts are usually placed as shown in Fig. 1.

To test these ideas, we prepared a set of 38 plates containing varying proportions of Brazilian twins, and also a set of 25 plates cut from single crystals, all cuts being AT (35°30' to the Z axis) and nominally of frequency about 5 Mc. These plates could also be excited at their third harmonic (size 20 × 15 × 0.3 mm). The electrodes were as shown in Fig. 1b (spot electrodes 8 mm in diameter).

The twins usually lay toward the edges of the plate and were not covered by the metal, but in some cases the thin twinned parts passed under the electrodes. These plates were mounted in K-19 holders, which were evacuated to 10^{-1} to 10^{-2} mm Hg.

The plates were tested as follows:

1. The activity was measured at the fundamental and at the third harmonic with a Shembel oscillator.

2. The temperature coefficient of the frequency was measured between +20 and +70°C with the plate excited at its third harmonic.

3. Parameters $\varkappa$ (circuit magnification) and c_0 (static capacitance of crystal and holder) were measured [3].

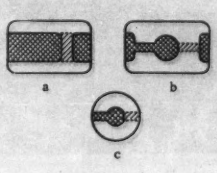

Fig. 1

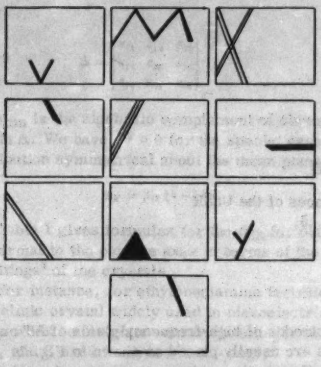

Fig. 2. Examples of disposition of twins on resonant plates whose response does not differ from that of a single crystal.

4. The spectrum was recorded.

R_q (equivalent loss resistance) was also measured.

The twins produced no change in the frequency coefficients. These plates had been ground in the same mount with the single-crystal ones to the same size and had the same frequency. Also, all twinned plates (except one) had temperature coefficients equal to or less than those of the single-crystal plates. The one poor plate was checked with an x-ray goniometer and was found to have been wrongly cut, so we may say that Brazilian twins produce no appreciable distortion in the mode of oscillation. Moreover, the twinned plates included none vibrating at several frequencies.

The activity (as expected) was found to be directly related to the amount of twinned material under the electrode; it was as for single-crystal plates when there was no twinned material under the metal, or even when the twinned part under the metal was only a thin band (Fig. 2). The same applies to $\varkappa$ and R_q, which were also dependent on the particular part of the twin found under the metal (Fig. 3).

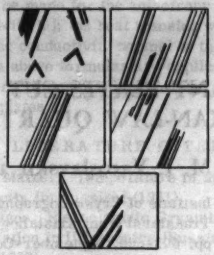

Fig. 3. Examples of twins in plates whose response was well below normal.

Quartz crystals containing Brazilian twins, which are usually rejected for piezoelectric use, may thus often be employed to make filter plates without showing performance inferior to that of single-crystal ones.

We are indebted to I.S. Zheludev for valuable advice and for criticisms of the manuscript.

LITERATURE CITED

1. A.V. Shubnikov, "The piezoelectric effect in quartz twins," Tr. Inst. Kristallogr., 5, 117-122 (1949).
2. I.G. Basin, Author's Certificate No. 68,098, dated May 15, 1948.
3. E.I. Kamenskii, "New parameters of quartz plates and an engineering calculation method for self-excited quartz oscillators," Izv. Akad. Nauk SSSR, ser. fiz., 20, 2, 237-250 (1956).

SOVIET PHYSICS – CRYSTALLOGRAPHY VOL. 1, NO. 5 SEPT.-OCT., 1956

LECTURE EXPERIMENT FOR DEMONSTRATING RHYTHMIC GROWTH IN SALOL CRYSTALS

A. V. Shubnikov

Institute of Crystallography, Academy of Sciences of the USSR
Translated from Kristallografiya, Vol. 1, No. 5,
pp. 606-607, September-October, 1956
Original article submitted June 15, 1956

This demonstration is prepared as follows. A finely ground and slightly warmed glass slide is touched with a small brush previously dipped in molten salol (melting point 42.5°C) to produce two fairly thin lines meeting at a small angle. The specimen is then heated again and is allowed to cool to room temperature. Salol readily becomes supercooled, so it does not usually crystallize spontaneously.

The demonstration is started by initiating crystallization at one of the four ends with a needle bearing solid salol; the preparation is at once transferred to the microscope (used with ordinary light at a magnification of about twenty). The crystals grow rhythmically and (an interesting point), the growth front bends at the junction of the streaks to end up perpendicular to all four branches (Fig. 1). This can be demonstrated to a large audience by using a projection microscope, but this requires care to insure that the preparation does not become heated by the illumination system, because this can halt the rhythmic growth.

We have previously given a qualitative explanation for the rhythmic growth of salol crystals [1,2] which has not previously been described in this form.

LITERATURE CITED

1. A.V. Shubnikov, How Crystals Grow [in Russian] (1935), p. 79.
2. A.V. Shubnikov, The Formation of Crystals [in Russian] (1947), p. 47.

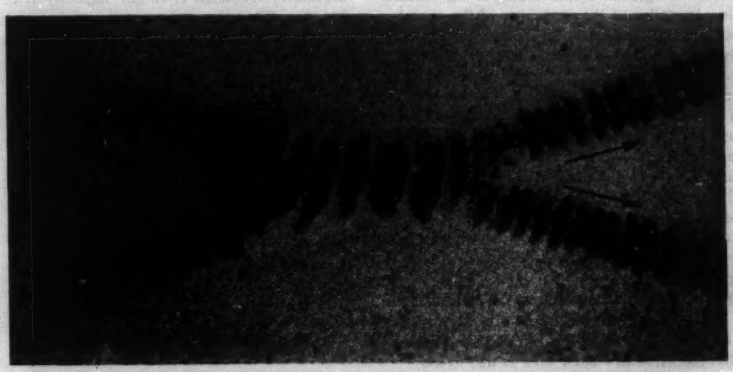

Fig. 1. The crystallization was started in the top left branch and propagated in the directions shown by the arrows.

SPIRAL GROWTH LAYERS ON BARIUM TITANATE CRYSTALS

N. V. Gliki, I. A. Pleteneva, and V. A. Timofeeva

Institute of Crystallography, Academy of Sciences of the USSR

Translated from Kristallografiya, Vol. 1, No. 5, pp. 607-608, September-October, 1956
Original article submitted July 13, 1956

Spiral growth layers have recently been reported for many organic and inorganic substances, but none of these is a ferroelectric. Recently, we observed spirals on barium titanate, which were produced during thermal analyses concerned with the crystallization of $BaTiO_3$.

The layers occur on the most abundant faces of the {100} form (Fig. 1); they have straight edges. Figure 1 is a crystal seen in slightly oblique reflection, which reveals simultaneously the spirals and the domain pattern. The parts of the spiral are not parallel to the edges of the crystal or to the domain boundaries, which run parallel to those edges; the deviations are 5-6°. The reason for this may be as for the spirals on salol crystals [1]. The angular deviation θ is governed by the ratio of the velocity v of the tangential displacement to the velocity V of the elongation of the periphery of the spiral.

Oblique illumination (Fig. 2) was used to reveal the domains directly under the center of the spiral. The crystal evidently contains several regions differing in orientation of the domain boundaries directed along face diagonals. Directly under the center of the spiral lies an opaque region resembling a spherical inclusion; near the spot and along the diagonals lie regions in which the domains with mutually perpendicular directions overlap. The four sectors around the center have the directions of the domain boundaries changing in a way such as to make the boundaries in adjacent sectors mutually perpendicular.

The final domain structure is dependent on the initial stresses and on any change in these produced by the domain structure [2], so we may suppose that the structure seen here is due to the stresses arising near the screw defect, which acts as a growth center.

Chernysheva [3] has described related effects in the twinning of Rochelle salt; the distribution of the twins (domains) is governed by the structural imperfections, and this becomes more complex in parts rich in inclusions (microscopic foreign particles, inclusions of solution). Polarized light reveals a regular array of light and dark regions around the inclusions, but the photographs show that the boundaries near the twins (light or dark) all have the same direction. This domain structure in Rochelle salt differs from that in our barium titanate crystal.

The $BaTiO_3$ crystals were platelets with faces of the {100} form, which were produced from a melt of barium chloride, barium carbonate, and titanium dioxide (2:1, 4:1), which was used in corundum crucibles of 20 cm^3 capacity at 1400-1480°C. The temperature was measured with a differential platinum–platinum–rhodium thermocouple.

Fig. 1. Face of a barium titanate crystal carrying a spiral growth layer. × 150.

Fig. 2. Internal structure of the same crystal, × 150.

The temperature and time spent in the molten state were tested for their effects on the heat of crystallization and on the morphology of the crystals. The differential cooling curve was smooth and without halts if the melt was heated to temperatures up to 1450°C, but not maintained at the maximum temperature, because only a small quantity of material was crystallizing, so the temperature difference from the Al_2O_3 standard was inappreciable. An effect became apparent only when the melt was kept at 1450°C for 3 h, presumably because sufficient titanate is formed in solution to give a fair crop of crystals on cooling, these releasing heat and so delaying the fall in temperature, which is seen on the differential curve as an exothermic peak. These were the conditions that gave crystals with spirals on their faces. An effect is detectable for shorter times (about 1 h) but only if the temperature is raised to 1480°C.

LITERATURE CITED

1. S. Amelinehx, "Théorie et observations concernant la croissance des cristaux de salol," J. Chim. Phys. et Phys.-Chim. Biol., 50, 4, 218-225 (1953).
2. A. Hippel, "Ferroelectricity, domain structure, and phase transitions of barium titanate," Rev. Mod. Phys., 22, 221-237 (1950).
3. M. A. Chernysheva, "Effects of zone and sector structure on the distribution of twins (domains) in Rochelle salt crystals," Dokl. Akad. Nauk SSSR, 91, 1, 87-88 (1953).

SPIRAL STRUCTURE OF ACCESSORY GROWTH ON (0001) SURFACES OF ARTIFICIAL QUARTZ CRYSTALS

L. I. Tsinober

All-Union Piezooptic Mineral Raw Materials Research Institute

Translated from Kristallografiya, Vol. 1, No. 5, pp. 609-610, September-October, 1956
Original article submitted July 3, 1956

These structures on quartz crystals have been reported several times, but without detailed illustration or description.

Willis, in 1952 [1], merely stated that he had observed these spirals on the R faces of natural quartz, while Weill [2] gave a photomicrograph of a spiral on a (0001) surface of a quartz inclusion in a molybdenite block from Queensland (Australia). This spiral is very difficult to distinguish in the journal, partly because the state of the surface generally was poor. More recently, it has been reported [3] that the accessory growth on the R faces of artificial quartz consisted of concentric layers and also spiral structures; but the plates show only concentric layers and include no spiral structure.

Here we give several photomicrographs of accessory growth spiral structures on the (0001) surfaces of an artificial quartz crystal.

This crystal was grown in this institute from a seed plate in the form of a disk 2.5 mm thick and 35 mm in diameter cut perpendicular to the L_3 axis of a single crystal. The initial process was one of regeneration; the circular seed plate rapidly became hexagonal, and the area of the slow-growing R faces gradually increased, whereas that of the fast-growing basal surface rapidly diminished. The growth rates of the faces of the small r rhombohedron were substantially higher than those of the R faces under these conditions (they were roughly the same as for the basal surface), so the r faces did not arise during growth. At the end of regeneration the crystal had faces corresponding to three simple forms: $\{10\bar{1}0\}$ hexagonal prism, $\{10\bar{1}1\}$ major rhombohedron, and $\{8\bar{1}91\}$ trapezohedron.

The basal surface grew by nucleation and extension of numerous conical accessories, which often became trigonal pyramids with rounded faces and edges, the orientation being such as to set the rounded edges toward the emergence of the negative ends of the L_2 axes (Fig. 1).

It appears that amorphous silica may be precipitated from the soda solution while the autoclave is cooling during the final stage of growth; this forms a thin film over the surfaces that tends to mask details. Figure 2c shows parts of such a film. This may be adequately removed from the prism and positive rhombohedron faces by boiling in concentrated NaOH, but this treatment was ineffective for the basal surface, except in the case of crystals at the very top of the autoclave, which remain above the solution during the cooling. Very occasionally such crystals have basal surfaces free

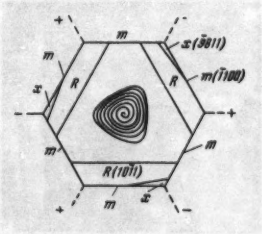

Fig. 1

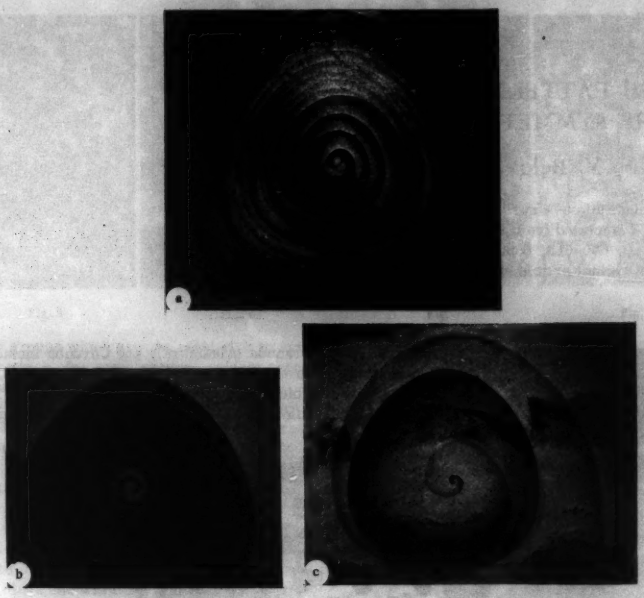

Fig. 2. Accessory pyramids with obvious spiral structure on a (0001) surface of artificial quartz, x 100.

from this film, and one such crystal showed spiral growth on the basal surface; three spirals are shown in Fig. 2, magnification 100.

The positive print reveals the trigonal structure of the spirals and shows that the (0001) layers are anisotropic in growth rate. The spirals of Figs. 2a and 2b are adjacent on a single crystal (right-handed); their senses are opposite, which is evidence that the sense of the spiral is unrelated to the optical sign of the crystal.

We are indebted to N.V. Gliki for advice and assistance in photographing these spirals.

LITERATURE CITED

1. B.T.M. Willis, "Screw dislocation in quartz," Nature, 170, 4316, 115-116 (1952).
2. A.R. Weill, "Observation des figures de croissance en spirale sur des cristaux de quartz naturel et d'alumine fondu," Compt. Rend., 235, 3, 256-257 (1952).
3. N.Yu. Ikornikova and V.P. Butuzov, "Relief of faces on artificial quartz crystals during the initial period of growth," Tr. Inst. Kristallogr., 11 (1956).

MOORISH PATTERNS OF THE MIDDLE AGES AND THE SYMMETRY GROUPS

N. V. Belov

Institute of Crystallography, Academy of Sciences of the USSR

Translated from Kristallografiya, Vol. 1, No. 5,
pp. 610-613, September-October, 1956
Original article submitted July 29, 1956

The Crystallography Symposium in Madrid (April 2-6, 1956) ended with excursions to Southern Spain, including centers of the former Moorish culture. Some of the relics of Seville (Alcazar), Granada (Alhambra), and Cordoba include walls covered with simple geometric patterns, many of which form striking illustrations of the 17 (single-color) and 46 (two-color) infinite two-dimensional

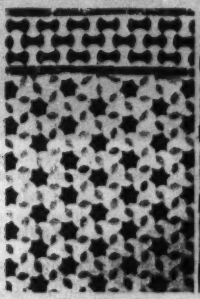

Fig. 1

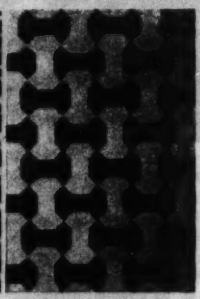

Fig. 2

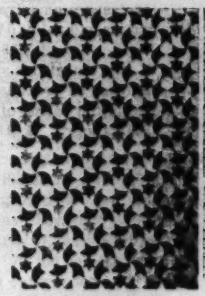

Fig. 3

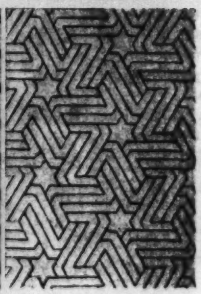

Fig. 4

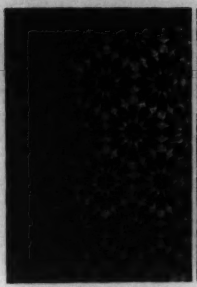

Fig. 5

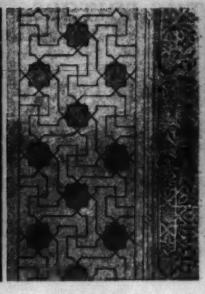

Fig. 6

Fig. 7

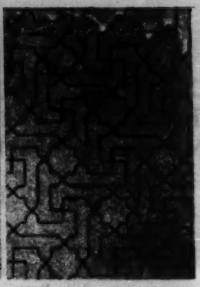

Fig. 8

symmetry groups which are the most rich in symmetry but which, for some reason, seldom appear in tapestries and other patterns.

The striking hexagonal pattern at Alhambra (12th to 13th century) consists entirely of current international symbols for hexad, triad, and diad axes (Fig. 1); it illustrates group p6.

Figure 2 shows a tetragonal pattern corresponding to the p4'g'm two-color group and consisting of a single, very simple figure repeated. The same pattern is seen in the border of Fig. 1.

Figure 3 would illustrate group p6' if the alternately black and white symbols for the triad axes were identical, i.e., if there were only stars of two colors or only ditrigons. The difference between the figures reduces the symmetry to p3.

Figure 4 represents interwoven bands of symmetry P622, i.e., one of the 230 (80) groups.

Figure 5 has the p6mm symmetry reduced to orthorhombic by the use of two halftones. The border at the top is common in tapestries and has symmetry pa'.

The tetragonal patterns of Figs. 6-8 are quite common in parquet flooring and elsewhere.

The stone floors of the Moorish buildings most frequently have the herringbone pattern characteristic of our wood-block floors; they have the barely perceptible orthorhombic symmetry pgg (Fig. 9).

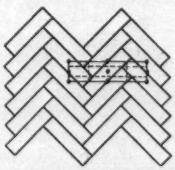

Fig. 9

All the older buildings have decorative works often in the form of regular reentrant polyhedra such as those illustrated in volume 27 of the Great Soviet Encyclopedia. However, these are more commonly based not on the regular dodecahedron but on combination of the cube with the octahedron (the coordination polyhedron giving closest packing) to give alternating square and triangular faces, these bearing the corresponding pyramids.

Finally, Fig. 10 illustrates the "Symmetry" sculpture in the Prado Museum, Madrid.

Fig. 10

LETTER TO THE EDITORS

ANSHELES'S COMMENTS* ON "A TRADITIONAL ERROR AND THE MANY WAYS IN WHICH IT APPEARS"†

A. V. Shubnikov

Institute of Crystallography, Academy of Sciences of the USSR

Translated from Kristallografiya, Vol. 1, No. 5,
p. 614, September-October, 1956
Original article submitted August 10, 1956

In my paper of the above title I stated that this error occurs in a variety of forms in textbooks on crystallography; it is essentially the impermissible replacement of an asymmetric figure or point by the most symmetrical figure, i.e., a sphere or a point by implication assigned the symmetry of a sphere.

Ansheles criticizes not my entirely clear formulation, but some idea entirely of his own, which is concerned not with the replacement of an asymmetric figure by a symmetrical point, but with the replacement of a symmetrical figure by some unspecified point. The same applies to the comments by the editor, in which he speaks of some crystals as though shown in my illustrations, whereas the latter do not show any crystals. Ansheles's comments, and those by the editors of the Zapiski, are irrelevant to my paper, so they require no additional reply from me. It remains only to note that such comments could appear in a journal published by the Academy, whereas the objections to them were not published.

*Zap. Vsesoyuzn. Min. Obshch., 84, 239 (1955).
†Zap. Vsesoyuzn. Min. Obshch., 83, 408 (1954).